

Directed functionalization of oxide and carbon nanomaterials for the development of efficient catalysts for carbon dioxide conversion into value-added products

Project Completion Report

DST No: INT/RUS/RFBR/P-322



Submitted by

Dr. Pankaj Bharali

Principal Investigator, Indian Counterpart

Assistant Professor
Department of Chemical Sciences
Tezpur University, India
Assam- 784 028

Jointly with

Dr. Mikhail A. Kerzhentsev

Principal Investigator, Russian Counterpart
Senior Researcher
Boreskov Institute of Catalysis, Novosibirsk
5, Pr. Akad. Lavrentieva, Novosibirsk, 630090, Russia

PROJECT COMPLETION REPORT

1. Title of the project: Directed functionalization of oxide and carbon nanomaterials for the development of efficient catalysts for carbon dioxide conversion into value-added products

2. Principal Investigator(s) and Co-Investigator(s): Dr. Pankaj Bharali

3. Implementing Institution(s) and other collaborating Institution(s): Tezpur University and Boreskov Institute Catalysis

4. Date of commencement: 19/02/2019

5. Planned date of completion: 19/02/2021

6. Actual date of completion: 01/07/2021 (with no-cost extension)

7. Objectives as stated in the project proposal: The main objective of this project is to develop novel X/MO_y ($M = Ce, La, Mg, Ce-La, Ce-Mg$; $X = Pd, Ni, NiPd$) and X/C and $X/CeO_2/C$ ($X = Pd, Cu, Ni, PdCu, PdNi$) nanocatalysts for steam/ CO_2 reforming of methane and electrocatalytic CO_2 reduction. To achieve this goal the following tasks will be undertaken:

(i) Synthesis of X/MO_y ($M = Ce, La, Mg, Ce-La, Ce-Mg$; $X = Pd, Ni, NiPd$) possessing the desired properties by varying X and M by Pechini method, sol gel or evaporation induced self-assembly (EISA) towards steam/ CO_2 reforming of methane.

(ii) Synthesis of X/C and $X/CeO_2/C$ ($X = Pd, Cu, Ni, PdCu, PdNi$) hydrothermal/solvothermal method with desired properties towards electrocatalytic CO_2 reduction.

(iii) Characterization of synthesized catalysts by a wide range of spectroscopic (FTIR, EPR, XPS/AES, ISS, Raman, EIS, and NMR), structural (XRD, SEM-EDX, TEM, TPR/TPO/TPD), electrochemical (CV, LSV, stripping voltammetry) and analytical (Gas and liquid chromatography) methods.

(iv) Determination of the optimal characteristics of catalyst for steam/CO₂ reforming of methane and electrocatalytic CO₂ reduction by varying the catalyst composition and preparation method.

8. Deviation made from original objectives if any, while implementing the project and reasons thereof:

The project objectives were slightly deviated due to the outbreak of Covid-19 pandemic. The electrocatalytic CO₂ reduction could not be performed due to unavailability of proper electrochemical set up. However, similar materials were synthesized and have been employed for related electrochemical applications. The actual works which were proposed have been communicated to journals and published.

9. Experimental work giving full details of experimental set up, methods adopted, data collected supported by necessary table, charts, diagrams & photographs:

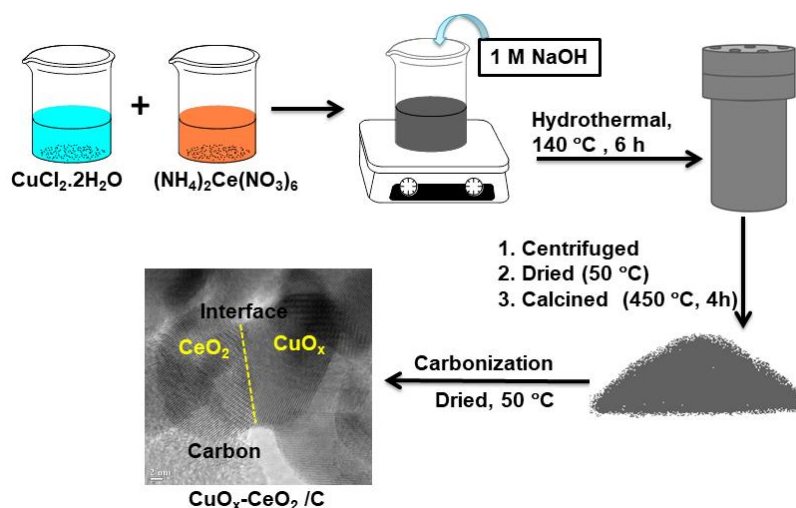
Methodology

Synthesis of materials.

Solvothermal and hydrothermal methods were mainly used to synthesize the materials. Addition of carbon to the oxide materials were done via physical grinding using a mortar, after calcination of the oxide precursor.

Hydrothermal synthesis of CuO_x-CeO₂/C.

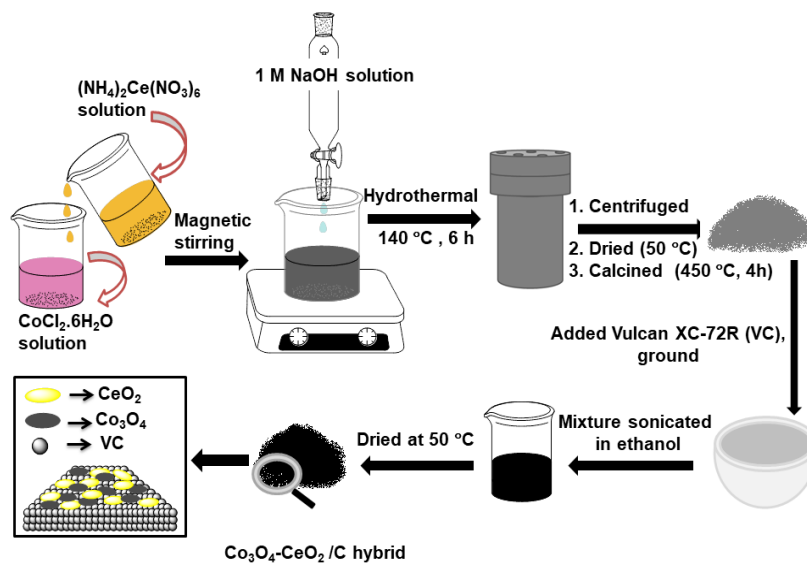
CuO_x-CeO₂ was synthesized via a simplified hydrothermal method. 0.05 M aqueous solution of (NH₄)₂Ce(NO₃)₆ (1.09646 g) and 0.05 M aqueous solution of CuCl₂·2H₂O (0.34096 g) were mixed together to form a homogenous solution such that the total concentration becomes 0.1 M. Next, 40 mL of 1 M NaOH solution was added drop wise to the freshly prepared salt solution using a burette and stirred for 30 min. The resulting solution was transferred to a 150 mL teflon-lined stainless steel autoclave and kept at 140 °C for 6 h. It was then allowed to cool for 15 h at room temperature. Finally the precursor was washed with Millipore water and absolute alcohol by centrifugation and dried at 50 °C. The precursor was calcined in a muffle furnace in air atmosphere at 450 °C for 4 h to get the CuO_x/CeO₂ composite oxide. In order to introduce the carbon support, the resultant oxide precursor was mixed with Vulcan XC-72R carbon (VC) powder in 30 % weight ratio. The resultant mixture was ground for 30 min using an agate mortar, ultrasonicated with ethanol (as a solvent) for 1 h and dried at 50 °C. The powdered mixture obtained was the carbon supported CuO_x-CeO₂, denoted as CuO_x-CeO₂/C. Scheme 1 pictorially represents the synthesis of the CuO_x-CeO₂/C EC.



Scheme 1. Schematic illustration of the synthesis of $\text{CuO}_x\text{-CeO}_2/\text{C}$.

Hydrothermal synthesis of the $\text{Co}_3\text{O}_4\text{-CeO}_2/\text{C}$ hybrid.

$\text{Co}_3\text{O}_4\text{-CeO}_2/\text{C}$ hybrid EC was obtained by following a similar reported procedure with slight modification. Firstly, the $\text{Co}_3\text{O}_4\text{-CeO}_2$ nanostructured materials were synthesized via a facile hydrothermal method. 0.4758 g of $\text{CoCl}_2\cdot 6\text{H}_2\text{O}$ (Merck) and 1.0964 g of $(\text{NH}_4)_2\text{Ce}(\text{NO}_3)_6$ (Merck) were dissolved separately in 20 mL of Millipore water each at room temperature. The two solutions which are of equal molar concentrations (0.05 M) were mixed together under constant magnetic stirring until a clear solution was obtained. To it, 40 mL of 1 M NaOH solution was slowly added drop wise using a burette with vigorous stirring for 30 min. The resulting solution was kept in an oven at 140 °C for 6 h using a Teflon-lined stainless-steel autoclave followed by cooling for 15 h. After washing with Millipore water and ethanol several times, the product collected via centrifugation was dried at 50 °C for 24 h. The obtained powder was then calcined at 450 °C for 4 h in air atmosphere to obtain the oxide, denoted as $\text{Co}_3\text{O}_4\text{-CeO}_2$. Afterwards, VC (obtained from Cabot Corporation, Navi Mumbai as gift) was mixed with $\text{Co}_3\text{O}_4\text{-CeO}_2$ oxide by physical grinding method for half an hour. The ground mixture was ultrasonically dispersed in ethanol (Merck) for 1 h and dried at 50 °C to obtained the final product *i.e.*, $\text{Co}_3\text{O}_4\text{-CeO}_2/\text{C}$ hybrid. A total loading of 30 % (by weight) of the oxide hybrid was maintained to obtain $\text{Co}_3\text{O}_4\text{-CeO}_2/\text{C}$. The synthesis of $\text{Co}_3\text{O}_4\text{-CeO}_2/\text{C}$ hybrid is diagrammatically represented in Scheme 2.



Scheme 2. Schematic representation of the synthesis of $\text{Co}_3\text{O}_4\text{-CeO}_2/\text{C}$ hybrid.

Hydrothermal synthesis of CuO_x/C and CeO_2/C .

CuO_x/C was synthesized following the same synthetic method as above. About, 0.68192 g of $\text{CuCl}_2 \cdot 2\text{H}_2\text{O}$ was dispersed in 40 mL of Millipore water such that the total concentration becomes 0.1 M. Next, 40 mL of 1 M NaOH solution was added drop wise to the freshly prepared salt solution using a burette and stirred for 30 min. The resulting solution was transferred to a 150 mL teflon-lined stainless steel autoclave and kept at 140 °C for 6 h. It was then allowed to cool for 15 h. Finally the precursor was washed with millipore water and absolute alcohol by centrifugation and dried at 50 °C. The precursor was calcined in air at 450 °C for 4 h to get CuO_x . The VC was added to the CuO_x in 30 % weight ratio and ground for 30 min using the agate mortar, ultrasonicated with ethanol (as a solvent) for 1 h and dried at 50 °C to get CuO_x/C as the final product. CeO_2/C was also synthesized in a similar manner using $(\text{NH}_4)_2\text{Ce}(\text{NO}_3)_6$ as the Ce precursor.

Hydrothermal synthesis of $\text{Co}_3\text{O}_4/\text{C}$

Typically, to make a 0.1 M salt solution, 0.09517 g of $\text{CoCl}_2 \cdot 6\text{H}_2\text{O}$ was dispersed in 40 mL of Millipore water. Then, 40 mL of 1 M NaOH solution was added drop wise to the freshly prepared salt solution using a burette with constant stirring for 30 min. The resulting solution was kept at 140 °C in a Teflon-lined stainless-steel autoclave for 6 h, followed by cooling for 15 h. The precursor was washed several times with Millipore water and absolute alcohol by

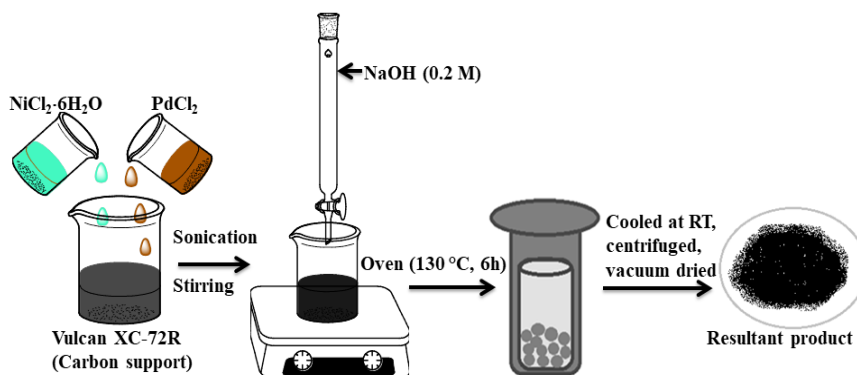
centrifugation and dried at 50 °C. The dried precursor was calcined in air at 450 °C for 4 h to get resultant oxide, *i.e.*, Co_3O_4 . Maintaining 30% weight ratio of the Co_3O_4 , VC was added to and ground for 30 min using the agate mortar, followed by ultrasonication in ethanol as the solvent for 1 h. and dried at 50 °C to get $\text{Co}_3\text{O}_4/\text{C}$ as the final product.

Synthesis of $(\text{Co}_3\text{O}_4+\text{CeO}_2) + \text{C}$ catalyst

$(\text{Co}_3\text{O}_4+\text{CeO}_2) + \text{C}$ was synthesized via physically mixing desired amount of the mono metallic oxides obtained after hydrothermal treatment *i.e.*, Co_3O_4 and CeO_2 , along with the carbon support. Like $\text{Co}_3\text{O}_4\text{-CeO}_2/\text{C}$ hybrid, the total MO loading over the carbon support is kept to be 30%.

Solvothermal synthesis of $\text{Pd}_3\text{Ni}/\text{C}$ alloy NPs

In a typical procedure to synthesize $\text{Pd}_3\text{Ni}/\text{C}$ alloy nanoparticles (NPs), 0.0157 g of $\text{NiCl}_2\cdot 6\text{H}_2\text{O}$ (0.066 mmol), 0.0351 g PdCl_2 (0.198 mmol) and 0.1 g of VC were dispersed in 50 mL of 1:1 solution of absolute EtOH and Millipore water. The solution was stirred for 15 min followed by 5 min of sonication. The total metal loading over the carbon support was maintained to be 20 wt%. 30 mL of NaOH solution (0.2 M) was then added drop wise to the mixture with continuous stirring for another 30 min. Then, 2 mL $\text{NH}_2\text{NH}_2\cdot\text{H}_2\text{O}$ was added drop wise to the mixture and stirred vigorously for 25 min. For solvothermal treatment, the solution was transferred into a teflon-lined stainless steel autoclave of 250 mL capacity and kept in an oven for 6 h at a temperature of 130 °C. After cooling it to room temperature, the final product obtained was washed several times with Millipore water and then with 50% v/v aqueous EtOH solution to remove the unreacted NaOH and Cl^- , centrifuged and dried in a vacuum oven at 55 °C. Scheme 3 represents the illustration of the synthesis of Pd–Ni/C alloy NPs.



Scheme 3. Schematic illustration of the synthesis of Pd–Ni/C alloy NPs.

Synthesis of PdNi/C and PdNi₃/C alloy NPs

PdNi/C and PdNi₃/C alloy NPs were synthesized via identical method like that of Pd₃Ni/C. All the experimental conditions were kept same, except the molar ratio of Pd and Ni salt precursors. Calculated amounts of PdCl₂ and NiCl₂·6H₂O were taken to maintain 1:1 and 1:3 atomic ratios of Pd and Ni in PdNi/C and PdNi₃/C alloy NPs, respectively.

Synthesis of Pd₃Cu/C, PdCu/C and PdCu₃/C alloy NPs

Pd₃Cu/C, PdCu/C and PdCu₃/C alloy NPs were synthesized by identical procedure like that of Pd₃Ni/C by using the appropriate metal precursor and maintaining the desired atomic ratios of Pd and Cu in the resultant NPs. In this case, CuCl₂·2H₂O was used as the Cu precursor.

Synthesis of Pd/C NPs

The Pd/C NPs were also synthesized using solvothermal method. In this case, only PdCl₂ of appropriated amount was employed as the metal precursor keeping all the experimental conditions unaltered.

Synthesis of Pd₃Cu/C–CeO₂ NPs

CuCl₂·2H₂O (0.0111g, 0.065 mmol), PdCl₂ (0.0347 g, 0.196 mmol), 0.05 g of VC and 0.05 g of CeO₂ were dispersed in 50 mL of 1:1 solution of absolute EtOH and Millipore water. The solution was stirred for 15 min followed by 5 min of sonication. The total metal loading over the support was maintained to be 20 wt%. 30 mL of NaOH solution (0.2 M) was then added drop wise to the mixture with continuous stirring for another 30 min. Then, 2 mL of NH₂NH₂·H₂O was added drop wise to the mixture and stirred vigorously for 25 min. The solution was then transferred into a teflon-lined stainless steel autoclave of 250 mL capacity and kept in an oven for 6 h at a temperature of 130 °C. After cooling it to room temperature, the final product obtained was washed several times with Millipore water and then with 50% v/v aqueous EtOH solution to remove the unreacted NaOH and Cl⁻, centrifuged and dried in a vacuum oven at 55 °C to obtain the resultant Pd₃Cu/C–CeO₂ NPs.

Synthesis of PdCu/C–CeO₂ and PdCu₃/C–CeO₂ NPs

PdCu/C–CeO₂ and PdCu₃/C–CeO₂ alloy NPs were synthesized via the same method like that of Pd₃Cu/C–CeO₂. All the experimental conditions were kept same, except the atomic ratio of Pd and Cu. Calculated amounts of PdCl₂ and CuCl₂·2H₂O were taken to maintain 1:1 and 1:3 atomic ratios of Pd and Cu in PdCu/C–CeO₂ and PdCu₃/C–CeO₂ NPs, respectively.

Synthesis of Pd₃Ni/C–CeO₂, PdNi/C–CeO₂ and PdNi₃/C–CeO₂ NPs

Here, NiCl₂·6H₂O was used as the Ni precursor following the same synthetic procedure similar to Pd₃Cu/C–CeO₂, maintaining the desired atomic ratios of Pd and Ni in the resultant NPs.

Physicochemical Characterization

The synthesized materials were characterized by a wide range of spectroscopic and structural methods such as powder X-ray diffraction (p-XRD), Fourier-transform infrared spectroscopy (FTIR), Brunauer-Emmett-Teller (BET) specific surface area analyses, Raman spectroscopy, thermogravimetric analysis (TGA), scanning electron microscopy (SEM), energy dispersive X-ray (EDX) spectroscopy, transmission electron microscopy (TEM) and high-resolution TEM (HRTEM), X-ray photoelectron (XP) spectroscopy (XPS). p-XRD patterns of the ECs were recorded on a Bruker AXS Model D8 focus instrument with Cu K α ($\lambda = 0.15418$ nm) radiation source in a 2θ range of $10^\circ - 80^\circ$ and the corresponding step size of $0.05^\circ \text{ s}^{-1}$. Infra-red spectra of the ECs were carried out in a FTIR spectrophotometer, Model Nicolet Impact I-410 by making pellets of the samples with KBr. For elemental analysis, EDS mapping and the EDX spectra were obtained on an Oxford instrument equipped with a scanning electron microscope (SEM) instrument “JEOL, KSM Model 6390 LV” to obtain the corresponding SEM image. Raman analysis was carried out in a RENISHAW, UK Raman spectrometer using 514 nm laser as the excitation source with a laser power of 5 mW. TGA profiles were obtained up to 700 °C using Model TGA-50, Shimadzu where the ramp rate of air was maintained at 30 mL min^{-1} and heating rate was $10 \text{ }^\circ\text{C min}^{-1}$. TEM and HR-TEM images were obtained on a JEM-2100 instrument operating at 200 kV. XPS was conducted using a Shimadzu ESCA-3400 system with an Mg-anode X-ray gun (10 kV, 20 mA). Before measurements, all the samples were Ar-etched for 60 s. During data processing, the binding energies (BEs) of all the samples were calibrated pertaining to the adventitious carbon 1s peak at 284.6 eV as a reference. All of the XPS spectra were smoothed via Savitzky-Golay method using a window of 10 points. The relative percentage determination of Ce³⁺ species was done after baseline correction followed by peak fitting of the high resolution Ce 3d core-level XP spectra using Gaussian function. A Shirley-type background was subtracted from the signals during baseline correction. N₂ adsorption/desorption isotherms were collected on a Quantachrome Instrument (Model: Nova 1000e) at 77 K (liquid nitrogen temperature). The specific surface areas of the ECs were determined by the BET method using the adsorption data at a relative pressure (P/P_0) region of 0.02–0.29.

Fabrication of working electrode

Prior to fabrication of working electrode, the surface of the glassy carbon electrode (GCE) was polished to mirror finish to get a smooth and clean surface using 0.005- μm Al_2O_3 powder. Typically, 5 mg of the sample was dispersed in 0.2 mL of millipore water and 0.3 mL of 2-propanol followed by addition of 0.5 mL of 0.5 wt % Nafion solution (purchased from Alfa Aesar) as binder. The mixture was sonicated for at least 40 min until a homogeneous suspension is obtained. A known volume of the suspension was loaded onto a GCE (0.0705 cm^2 in area) to form a monolayer by drop casting method and dried at 35 $^\circ\text{C}$ for 4 h.

Electrochemical Measurements for oxygen reduction reaction (ORR) and oxygen evolution reaction (OER).

Electrochemical tests were conducted in a standard three-electrode electrochemical cell on a PGSTAT204 workstation (Metrohm Autolab, The Netherlands). The cell consists of an Ag/AgCl electrode in saturated KCl solution as the reference electrode, a Pt wire as the counter electrode and a catalyst-modified glassy carbon electrode as the working electrode. All the electrochemical measurements were carried out at room temperature.

Cyclic Voltammetry (CV): For ORR, CV experiments were performed in N_2 - and O_2 -saturated 0.1 M aqueous solution of KOH (working electrolyte) in a potential window of 0.2 to -0.8 V (vs. Ag/AgCl). Prior to N_2 - and O_2 -saturated scans, ultra-high pure N_2 and O_2 were purged for 30 min for making a saturated environment and the flow was also continued during the tests. The working electrode was subjected to a continuous CV cycles between 0.2 to -0.8 V (vs. Ag/AgCl) at a scan rate of 100 mV s^{-1} till a reproducible CV curve was obtained. After surface cleaning, the final curve plot was obtained in O_2 -saturated electrolyte at a scan rate of 50 mV s^{-1} .

Linear Sweep Voltammetry (LSV): The same WEs fabricated for CV experiments and an rotating disk electrode (RDE) attached to the same electrochemical analyzer were used. LSV curves were obtained in the potential range of 0.2 to -0.8 V and 0.2 to 1.5 V (vs. Ag/AgCl) for ORR and OER, respectively at a scan rate of 10 mV s^{-1} . Overpotential at 10 mA cm^{-2} (η_{10}) for OER is calculated using the following equations: $E_{\text{experimental}} - E_{\text{theoretical}}$, where $E_{\text{theoretical}} = 1.23$ V vs. RHE. For determination of number of electrons transferred (n) during ORR, RDE experiments were carried out at different rotations (400, 900, 1600, 2500 and 3600 rpm) to obtain the Koutecky–Levich (K–L) plots. RDE experiments for both the reactions were

conducted in O₂-saturated 0.1 M aqueous solution of KOH. The currents obtained are normalized to the geometric surface area of the GCE for all the samples.

K–L equation: The number of electrons transferred (n) during the reaction was calculated using K–L equation on the basis of the LSV curves obtained from the RDE results [S1]:

$$\frac{1}{j} = \frac{1}{j_k} + \frac{1}{j_d} = \frac{1}{j_k} + \frac{1}{B\omega^{1/2}}$$

Slope of K–L plot, $B = 0.62nFC_0(D_0)^{2/3}\nu^{-1/6}$ and $j_k = nFkC_0$

where, j is the measured current density, j_k is the kinetic current density, j_d is the diffusion current density, ω is the rotation speed, n is the number of electrons transferred during ORR, F is the Faraday constant (96485 C mol⁻¹), C_0 is the concentration of dissolved O₂ (1.2 × 10⁻⁶ mol cm⁻³), D_0 is the diffusion coefficient of O₂ (1.9 × 10⁻⁵ cm² s⁻¹), ν is the kinetic viscosity of the electrolyte (0.01 cm² s⁻¹).

Chronoamperometry (CA) test: CA responses were obtained at a constant potential of –0.3 V (vs. Ag/AgCl) for 6 h to check the long-term stability. The test was performed in O₂-saturated 0.1 M KOH aqueous solution at 1600 rpm.

Electrochemically active surface area (ECSA): The double-layer capacitance (C_{DL}) was determined for the ECs to determine ECSA for metal-oxides (MOs). In order to get C_{DL}, a non-Faradaic potential region where there is no redox process taking place must be identified from the CV curve obtained in N₂-saturated 0.1 M aqueous solution of KOH. Afterwards, scan rate dependent CVs were obtained basically in a 0.1 V window around the open circuit voltage. The various scan rates are: 0.005, 0.01, 0.025, 0.05, 0.075, 0.1, 0.2 and 0.3 V s⁻¹. The measured current in this potential region is due to double-layer charging. Plot of charging current as a function of scan rate gives a straight line with a slope which is equal to C_{DL}. ECSA is then calculated by dividing C_{DL} by the specific capacitance (C_S) according to the equation:

$$\text{ECSA} = \frac{C_{\text{DL}}}{C_{\text{S}}}$$

For alkaline electrolyte, C_S = 0.040 mF cm⁻².

$$\text{ECSA/gram}_{\text{EC}} = \frac{\text{ECSA}}{\text{Mass loading of EC}}$$

10. Detailed analysis of results indicating contributions made towards increasing the state of knowledge in the subject:

Results and discussion

Characterization related to $\text{CuO}_x\text{-CeO}_2/\text{C}$, CuO_x/C and CeO_2/C

XRD analysis: The phase purity and the crystalline structure of the electrocatalysts (ECs) and VC were determined by p-XRD. Figure 1a shows the p-XRD patterns of CuO_x/C , CeO_2/C , $\text{CuO}_x\text{-CeO}_2/\text{C}$ and VC. A broad peak observed at *ca.* $2\theta = 24^\circ$ corresponds to VC (JCPDS #75-1621). The weaker nature of this peak in all the ECs is due to overlapping from highly crystalline CuO_x and CeO_2 phases. The sharp and highly crystalline peaks at 2θ values of 28.5° , 33.0° , 47.4° , 56.3° , 59.1° , 69.4° , 76.7° and 79.1° corresponding to (111), (200), (220), (311), (222), (400), (331) and (420) planes, respectively, are characteristics of face-centered cubic (fcc) fluorite CeO_2 phase (JCPDS #34-0394). The diffraction peaks appearing at 2θ values of 32.4° , 35.4° , 38.7° , 48.7° , 53.4° , 58.3° , 61.5° , 66.2° , 68.0° , 72.4° and 75.2° are respectively indexed to (110), (002), (111), (202), (020), (202), (113), (311), (220), (311) and (222) crystalline phases of monoclinic CuO (JCPDS #45-0937). The presence of all the characteristic diffraction peaks corresponding to fcc fluorite CeO_2 and monoclinic CuO phases indicates the co-existence of CuO and CeO_2 phases in the resultant $\text{CuO}_x\text{-CeO}_2/\text{C}$ EC.

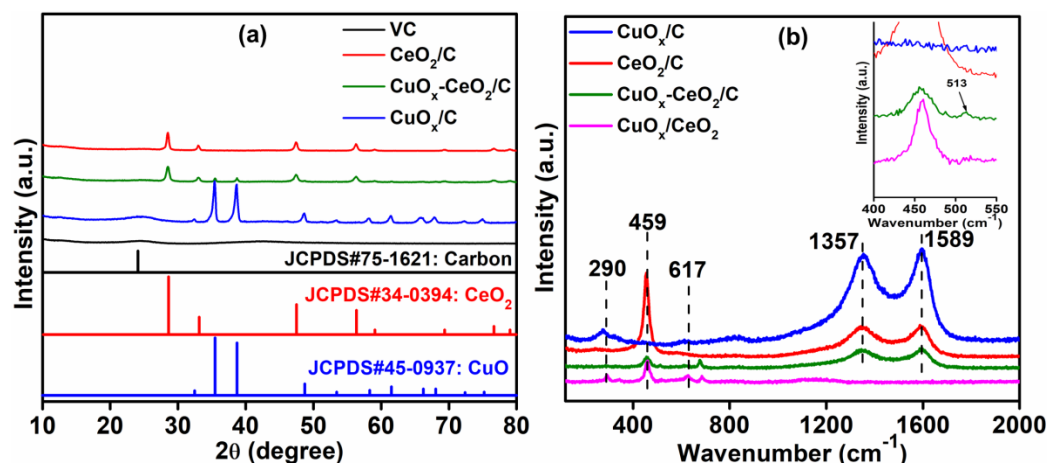


Figure 1. (a) p-XRD patterns of CeO_2/C , CuO_x/C , $\text{CuO}_x\text{-CeO}_2/\text{C}$ ECs and VC, and (b) Raman spectra of CeO_2/C , CuO_x/C , $\text{CuO}_x/\text{CeO}_2$ and $\text{CuO}_x\text{-CeO}_2/\text{C}$ ECs (Inset: magnified Raman spectra of the respective ECs).

Raman analysis: Raman spectroscopy was carried to further elucidate the phases of the as-synthesized materials. It acts as a non-destructive technique that can differentiate between ordered and disordered carbon. Figure 1b represents the Raman spectra of CeO_2/C , CuO_x/C ,

CuO_x/CeO₂, and CuO_x-CeO₂/C ECs. All the ECs, except CuO_x/CeO₂ shows two characteristic peaks around ~1357 and ~1589 cm⁻¹ which are indexed to the disordered sp³ hybridized carbon atom (denoted by D) and the vibration due to sp² graphitic carbon atoms (denoted by G), respectively. The degree of disorder in carbon supported materials is often determined from the ratio of intensity of D band (I_D) to the intensity of G band (I_G). Interestingly, the I_D/I_G ratio for CuO_x-CeO₂/C (1.99) is found to be slightly greater than that of CeO₂/C (1.81), and CuO_x/C (1.94) which implies higher degree of disordered carbon. A sharp band at ~459 cm⁻¹ is observed for all the ECs containing CeO₂ which is assigned to the F_{2g} symmetric vibrational mode of fluorite type CeO₂ (Ce–O–Ce stretching). The peak at ~290 cm⁻¹ (A_g), ~341 cm⁻¹ (B_{1g}) and ~617 cm⁻¹ (B_{2g}) corresponds to the presence of monoclinic CuO (Cu²⁺) which is in good agreement with the p-XRD analysis. The magnified region in the inset of Figure 1b shows a peak at ~513 cm⁻¹ that corresponds to the presence of Cu₂O, which is more prominent in CuO_x-CeO₂/C among all the Cu containing materials.

EDX analysis: The presence of C, O, Cu and Ce in CuO_x-CeO₂/C EC was confirmed from EDX analysis as shown in Figure 2a. The corresponding SEM image (Figure 2b) along with the EDS elemental maps (Figure 2c-f) clearly shows the dispersion of MOs over the carbon support and also confirms the presence of only detectable elements, respectively. EDX analysis shows that the atomic percentage of Cu (0.44%) and Ce (0.46%) are in 1:1 ratio. The total MO loading over the carbon support was also found to be 27.67% which corroborates well with the experimentally targeted MO loading (30%).

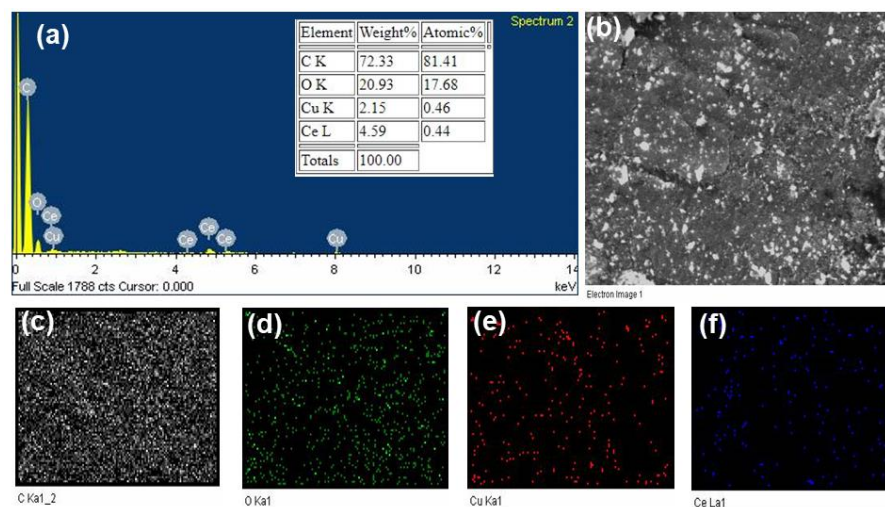


Figure 2. (a) EDX spectra of CuO_x-CeO₂/C EC; inset shows the table for elemental composition, (b) the corresponding SEM image and, (c-f) elemental maps for individual C, O, Cu and Ce.

TEM analysis: The size, morphology and microstructure of $\text{CuO}_x\text{-CeO}_2/\text{C}$ EC were further examined by TEM and HRTEM analyses. Figure 3a,b represents low-magnified TEM images of $\text{CuO}_x\text{-CeO}_2/\text{C}$ EC. These TEM images mainly show that the $\text{CuO}_x\text{-CeO}_2$ nanostructures of dark contrast are nearly spherical in shape and are highly dispersed over the carbon support of relatively lighter shades. The inset in Figure 3a represents the particle size distribution curve determined using Image J software. Most of the particles (both CuO and CeO_2) fall in the range of 8–14 nm and the average particle size of the $\text{CuO}_x\text{-CeO}_2$ nanostructures was calculated to be ~ 11 nm. Moreover, the presence of defect site on the surface of the nanostructures is also evident in the HRTEM image denoted by yellow dotted circle in Figure 3c. Figure 3d denotes the selected area electron diffraction (SAED) pattern which clearly exhibits well-defined concentric rings, indicating the polycrystalline nature of the material.

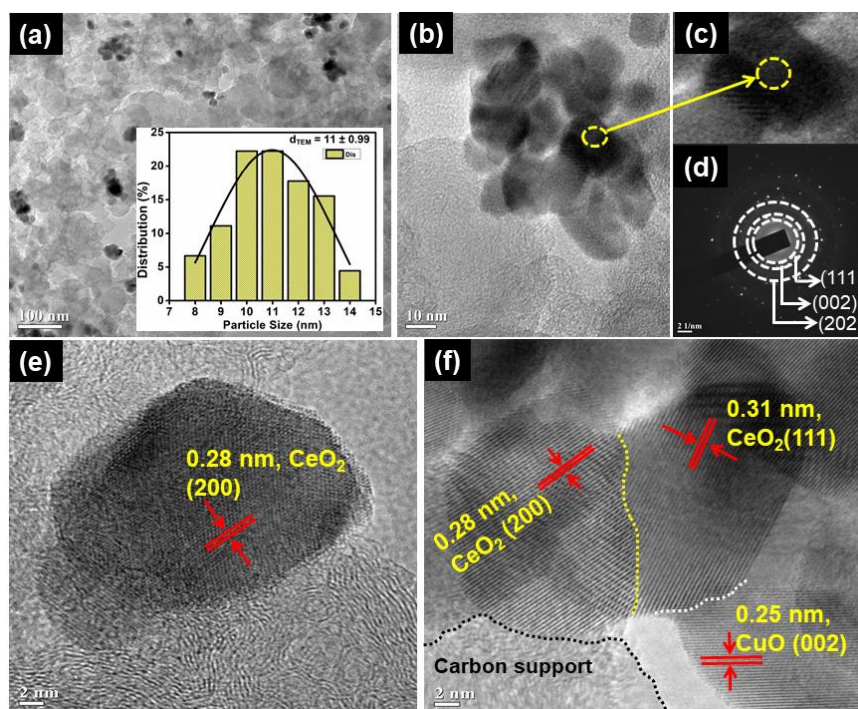


Figure 3. (a-c, e, f) TEM and HRTEM images with distinguished lattice fringes, the particle size distribution curve (inset image a) and (d) the SAED pattern for $\text{CuO}_x\text{-CeO}_2/\text{C}$ EC.

The HRTEM images shown in Figure 3(e,f) also exhibits clear lattice fringes corresponding to different facets associated with monoclinic CuO and fcc CeO_2 . From the lattice fringes of adjacent facets, the d-spacing was calculated. A d-spacing of 0.31 nm and 0.28 nm is very close to (111) and (200) facets of CeO_2 and a d-spacing of 0.25 nm can be indexed to (002) facet of

CuO, signifying high crystallinity. Further, precise observation of the HRTEM images directed us to define two distinguished interfaces *viz.*, the oxide-oxide and the oxide-carbon interface. The yellow, white and black dotted lines in Figure 3f outline the interface between different facets of CeO₂-CeO₂, CuO_x-CeO₂ and oxide-carbon. These interfaces are expected to synergistically promote the ease of charge transfer and electrical conductivity during the reaction which accounts for overall improvement in electrocatalytic activity of CuO_x-CeO₂/C EC.

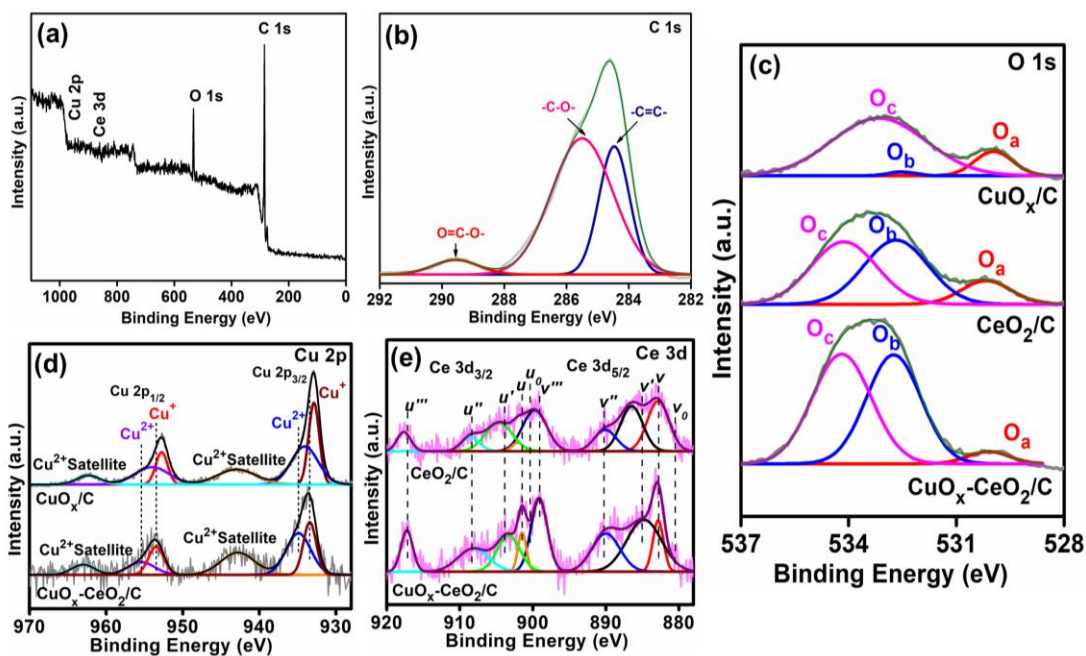


Figure 4. (a) XP survey spectrum, high resolution XP spectrum of (b) C 1s of CuO_x-CeO₂/C, (c) O 1s for CuO_x/C, CeO₂/C and CuO_x-CeO₂/C, (d) Cu 2p for CuO_x/C and CuO_x-CeO₂/C, and (e) Ce 3d for CeO₂/C and CuO_x-CeO₂/C.

XPS analysis: XPS was employed to obtain detailed information about the surface composition and electronic structure of the elements present in the synthesized ECs. Figure 4a represents the survey spectrum of CuO_x-CeO₂/C ECs in the BE range 1000–0 eV, which depicts four distinct peaks corresponding to C 1s, O 1s, Cu 2p and Ce 3d. The survey spectrum confirms the high purity of the sample thereby supporting EDX analysis data. The fitted C 1s core-level spectrum of CuO_x-CeO₂/C is comprised of three peaks as shown in Figure 4b. The two distinct peaks located at 285.5 and 284.6 eV are assigned to –C–O– and –C=C– groups, respectively. The faint peak around 289.5 eV is attributed to O=C–O chemical state. The combined high resolution spectra of O 1s for CuO_x/C, CeO₂/C and CuO_x-CeO₂/C ECs (Figure 4c) confirm the

existence of three types of oxygen species at different BEs. For $\text{CuO}_x\text{-CeO}_2/\text{C}$, the curve-fitting of the O 1s spectra gives two peaks at 530.1 and 532.7 eV which are the respective characteristics of lattice oxygen (O_a) in CeO_2 and adsorbed oxygen species such as OH^- , O^- and O^{2-} (O_b). O_b is generally related to the defect sites generated from low oxygen coordination. The peak at 534.1 eV (O_c) is ascribed to the water molecules adsorbed physically, respectively. The percentage of various oxygen species present in various ECs were calculated and presented in Table 1. The greater peak area of O_b in $\text{CuO}_x\text{-CeO}_2/\text{C}$ in comparison to that of CuO_x/C and CeO_2/C imply larger oxygen vacancies. The ratio of adsorbed oxygen to lattice oxygen *i.e.*, O_b/O_a also gives insight into the concentration of the surface oxygen vacancy. As observed, the O_b/O_a ratio is the highest for $\text{CuO}_x\text{-CeO}_2/\text{C}$ (11.7) in comparison to that of CuO_x/C (0.12), CeO_2/C (3.50) and $\text{CuO}_x/\text{CeO}_2$ (2.05) which is evident of more oxygen vacancies in $\text{CuO}_x\text{-CeO}_2/\text{C}$.

Table 1. Percentage of various oxygen species obtained from XPS analysis CeO_2/C , CuO_x/C , $\text{CuO}_x\text{-CeO}_2/\text{C}$ and $\text{CuO}_x/\text{CeO}_2$ composite.

ECs	O_a (%)	O_b (%)	O_c (%)	Ratio O_b/O_a
CeO_2/C	12.3	43.8	43.8	3.50
CuO_x/C	14.3	1.7	83.9	0.12
$\text{CuO}_x\text{-CeO}_2/\text{C}$	3.9	46.1	50.0	11.8
$\text{CuO}_x/\text{CeO}_2$	18.1	37.1	44.7	2.05

Figure 4d is the combined high resolution spectra of Cu 2p in CuO_x/C and $\text{CuO}_x\text{-CeO}_2/\text{C}$ ECs, which is mainly composed of two multiplets; a higher Cu $2p_{3/2}$ band and a lower Cu $2p_{1/2}$ band. The spin-orbit separation between the two multiplets was found to be 19.9 eV, which is in accordance with the reported literatures. Each of these multiplets is further deconvoluted into two peaks. For CuO_x/C , the peaks located at lower BEs (933 and 952.9 eV) correspond to Cu^+ species. The peaks at higher BEs (934.2 and 954.1 eV) along with two satellites at ~ 942.8 and ~ 962.9 eV are the characteristics of Cu^{2+} . The satellite peaks were observed at a BE which is 9 eV higher than the main Cu $2p_{3/2, 1/2}$ peaks. Similar peaks observed for Cu 2p spectrum in $\text{CuO}_x\text{-CeO}_2/\text{C}$ EC also confirms the presence of Cu^{2+} and Cu^+ species. From Figure 4d, it is also clear that all the peaks related to Cu^{2+} and Cu^+ undergo a positive shift of BE values in $\text{CuO}_x\text{-CeO}_2/\text{C}$, compared to that in CuO_x/C which indicates strong electronic coupling between CuO_x and CeO_2 . For Cu $2p_{1/2}$, a BE shift of 1.2 and 0.5 eV were observed for Cu^{2+} and Cu^+ ions $\text{CuO}_x\text{-CeO}_2/\text{C}$ and CuO_x/C , respectively. Likewise, a BE shift of 0.6 (Cu^{2+}) and 0.4 eV (Cu^+) were obtained for Cu $2p_{3/2}$.

As shown in Figure 4e, the high resolution spectra of Ce 3d for both CeO₂/C and CuO_x-CeO₂/C ECs is composed of two multiplets, *viz.*, Ce 3d_{5/2} (denoted by *v*) and Ce 3d_{3/2} (denoted by *u*). The deconvolution of these multiplets gives a total of eight peaks centered at 882.8 (*v*), 884.7 (*v'*), 889.9 (*v''*), 899.1 (*v'''*), 901.4 (*u*), 903.3 (*u'*), 908.1 (*u''*) and 917.2 (*u'''*) eV for CuO_x-CeO₂/C. Two more peaks at around 880.5 eV (*v₀*) and 900.3 eV (*u₀*) basically corresponds to Ce³⁺. However, very low intensity of these peaks limits the deconvolution of the Ce 3d spectra into eight, rather than ten components. Similar peaks are also obtained for CeO₂/C with a slight shift in the peak positions towards higher BE values which signifies electronic modification in CuO_x-CeO₂/C. The peaks labeled as *u*, *u''*, *u'''*, *v*, *v''* and *v'''* are associated with Ce⁴⁺ with an electronic configuration of 3d¹⁰4f⁰, while the peaks marked as *u'* and *v'* are attributed to Ce³⁺, thereby, indicating the co-occurrence of Ce⁴⁺ and Ce³⁺ in CuO_x-CeO₂/C. The existence of oxygen vacancies and charge redistribution at CuO_x-CeO₂ interface can further be proved by determining the relative percentage of Ce³⁺ from the high resolution spectra of Ce 3d. Additionally, the presence of Ce³⁺ in a material is itself an evidence of surface oxygen vacancies. The relative percentage of Ce³⁺ (*u₀* + *u'* + *v₀* + *v'*) and Ce⁴⁺ (*u* + *u''* + *u'''* + *v* + *v''* + *v'''*) is calculated from the fitted areas of the corresponding peaks according to the following equation:

$$\text{Percentage of Ce}^{3+} = \frac{[A(\text{Ce}^{3+})]}{[A(\text{Ce}^{3+}) + A(\text{Ce}^{4+})]} \times 100 \quad (1)$$

where, A is area under the peak.

The relative percentage of Ce³⁺ is estimated to be 38 % and 35 % for CuO_x-CeO₂/C and CeO₂/C, respectively. Clearly, CuO_x-CeO₂/C contains more Ce³⁺ ions compared to that of CeO₂/C which proves the occurrence of charge redistribution on the CuO_x-CeO₂ interface. The main interaction that happen at the CuO_x-CeO₂ interface stabilizes the more active Cu⁺ species than Cu²⁺ and can be represented as follows: Ce³⁺ + Cu²⁺ → Ce⁴⁺ + Cu⁺. These interactions positively affect the overall bifunctional ORR/OER activity of CuO_x-CeO₂/C EC.

BET surface area analysis: N₂ adsorption/desorption experiment was performed for all the ECs to determine specific surface area and porosity. Figure 5a-c illustrates the N₂ adsorption/desorption isotherms of CeO₂/C, CuO_x/C and CuO_x-CeO₂/C ECs. All the ECs exhibited type IV isotherm with a distinct H3 hysteresis loop in relatively high pressure region. The respective pore size distribution curves for all ECs were also obtained by BJH method from the desorption path of the isotherm, as shown in insets of Figure 5. The calculated pore diameter was 3.1 nm for all the ECs, which indicates their mesoporous nature. It could be seen

that the specific surface area calculated by the multipoint BET method for CuO_x-CeO₂/C (134.4 m² g⁻¹) is relatively smaller than that of CeO₂/C (135.9 m² g⁻¹) and CuO_x/C (140.7 m² g⁻¹) ECs. However, the reduced surface area of CuO_x-CeO₂/C doesn't affect its overall electrocatalytic activity towards ORR and OER. This might be due to the synergistic effect between CeO₂ and CuO_x that effectively overcomes the reduced specific surface area of CuO_x-CeO₂/C.

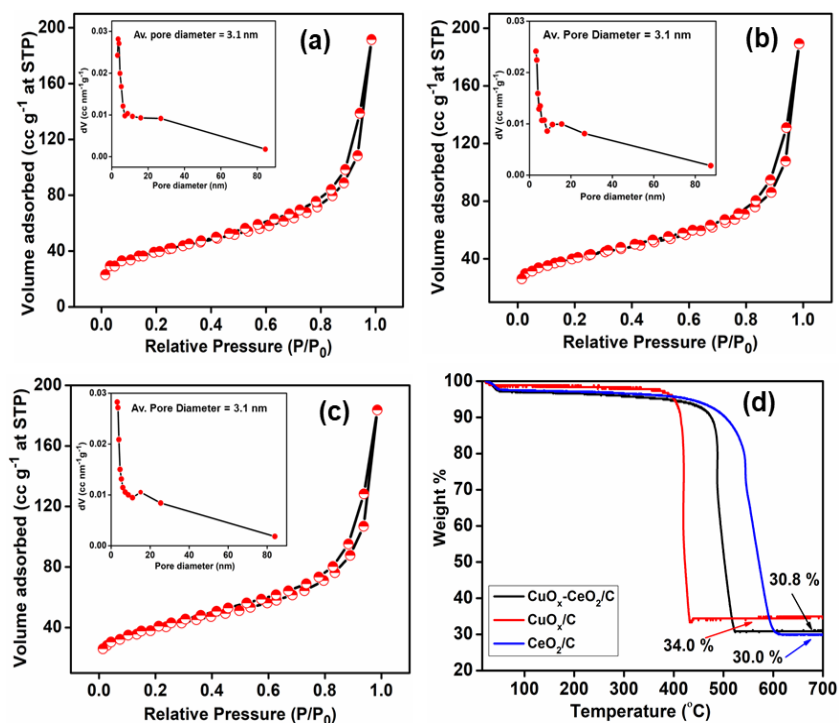


Figure 5. N₂ adsorption/desorption isotherms of (a) CeO₂/C, (b) CuO_x/C, (c) CuO_x-CeO₂/C ECs (inset shows the corresponding average pore diameter) and (d) TGA profile of CeO₂/C, CuO_x/C and CuO_x-CeO₂/C ECs in air atmosphere.

TGA analysis: Figure 5d shows the TGA profile of CeO₂/C, CuO_x/C and CuO_x-CeO₂/C ECs in air atmosphere up to 700 °C. The graph shows that conversion of carbon to CO₂ occurs at about 450–550 °C. However, decomposition of carbon support from CuO_x-CeO₂/C is negligible after 550 °C and the graph reaches a stable value of ~30% for all the ECs. This value is equivalent to the targeted weight % of the MO loading (*i.e.*, 30 wt %) over the carbon support.

Electrocatalytic oxygen reduction activity related to CuO_x-CeO₂/C, CuO_x/C and CeO₂/C ECs:

The electrocatalytic ORR performance of CeO₂/C, CuO_x/C and CuO_x-CeO₂/C ECs was evaluated using CV and LSV in 0.1 M KOH aqueous solution. Prior to the measurements, electrode surface cleaning was done by running CV up to 20 cycles in the potential window 0.2

to -0.8 V (vs. Ag/AgCl) to get stabilized signals and boost conductivity. In Figure 6a, the CV curves exhibit a prominent cathodic peak at -0.41 , -0.26 , -0.27 and -0.23 V for VC, CeO_2/C , CuO_x/C and $\text{CuO}_x\text{-CeO}_2/\text{C}$, respectively in O_2 -saturated electrolyte as compared to that in N_2 -saturated electrolyte. It suggests that the ECs are active towards ORR. The highest reduction peak towards more positive potential of $\text{CuO}_x\text{-CeO}_2/\text{C}$ among other ECs and VC indicates its superiority in electrochemical behavior towards ORR.

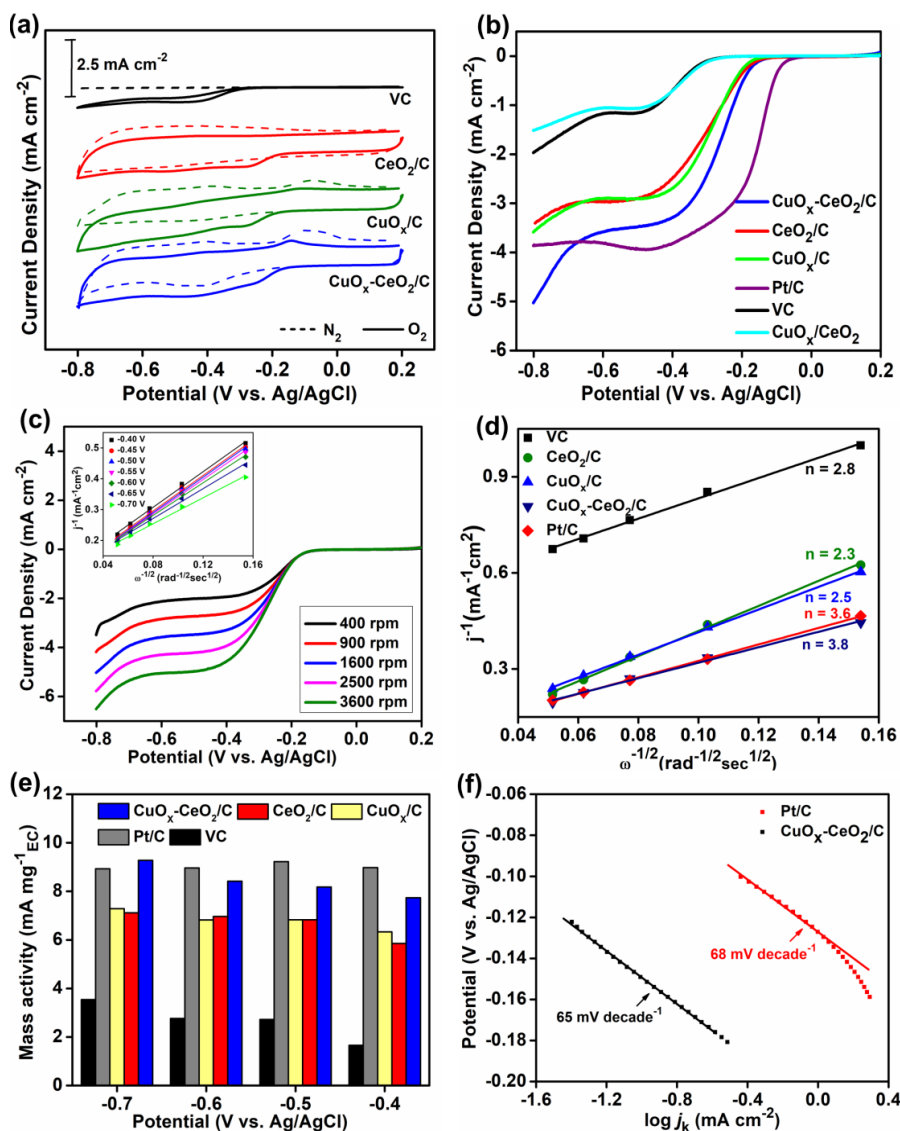


Figure 6. (a) CVs of VC, CeO_2/C , CuO_x/C , $\text{CuO}_x\text{-CeO}_2/\text{C}$ and Pt/C in N_2 -saturated (dash line) and O_2 -saturated (solid line) 0.1 M KOH (sweep rate = 50 mV s^{-1}); (b) Rotating rate dependent LSV curves for VC, CeO_2/C , CuO_x/C , $\text{CuO}_x\text{-CeO}_2/\text{C}$, Pt/C and $\text{CuO}_x/\text{CeO}_2$ in O_2 -saturated 0.1 M KOH at 1600 rpm (sweep rate = 10 mV s^{-1}); (c) Rotating rate dependent LSV curves for $\text{CuO}_x\text{-CeO}_2/\text{C}$ in O_2 -saturated 0.1 M KOH at various rotations (Insets: K-L plots at different

electrode potential); (d) K–L plots of different samples at -0.65 V, (e) Mass activities of all the samples under different potential values at 1600 rpm and (f) Tafel plots for $\text{CuO}_x\text{-CeO}_2/\text{C}$ and Pt/C derived from LSV curves at 1600 rpm.

LSV curves were also obtained on RDE to further evaluate the ORR activity of $\text{CuO}_x\text{-CeO}_2/\text{C}$ in O_2 -saturated 0.1 M KOH electrolyte at a rotation rate of 1600 rpm. As evident from Figure 6b, $\text{CuO}_x\text{-CeO}_2/\text{C}$ could successfully catalyze ORR at an onset potential (E_{onset}) of -0.10 V unlike CeO_2/C ($E_{\text{onset}} = -0.13$ and V), CuO_x/C ($E_{\text{onset}} = -0.13$), and $\text{CuO}_x/\text{CeO}_2$ composite ($E_{\text{onset}} = -0.26$). $\text{CuO}_x\text{-CeO}_2/\text{C}$ EC also proved to be a better EC than CeO_2/C , CuO_x/C and $\text{CuO}_x/\text{CeO}_2$ composite in terms of half-wave potential ($E_{1/2}$) and limiting current density (j_m). The lower $E_{1/2}$ and the highest j_m of $\text{CuO}_x\text{-CeO}_2/\text{C}$ can be correlated to the rapid electron conduction as well as efficient mass transfer of reactants to the electrochemically active sites of the $\text{CuO}_x\text{-CeO}_2/\text{C}$ EC. The j_m values of VC ($j_m = -1.96 \text{ mA cm}^{-2}$) and $\text{CuO}_x/\text{CeO}_2$ composite ($j_m = -1.51 \text{ mA cm}^{-2}$) shows that the addition of VC enhances the electronic conduction of the resultant EC (Figure 6b). The values of different electrochemical parameters of the ECs, VC and Pt/C are presented in Table 2. The enhanced activity of $\text{CuO}_x\text{-CeO}_2/\text{C}$ EC is mainly ascribed to the synergistic interaction between CeO_2 , CuO_x and the carbon support due to the formation of strong oxide-oxide/carbon interfaces. Although, $E_{1/2}$ values for $\text{CuO}_x\text{-CeO}_2/\text{C}$ (-0.30 V) is 0.15 V more negative than Pt/C (-0.15 V), however, in terms of limiting current density $\text{CuO}_x\text{-CeO}_2/\text{C}$ (-5.03 mA cm^{-2}) outperforms Pt/C (-3.86 mA cm^{-2}) by a value of -1.17 mA cm^{-2} .

Table 2. Summary of E_{onset} , $E_{1/2}$ and j_m of CeO_2/C , CuO_x/C , $\text{CuO}_x\text{-CeO}_2/\text{C}$, VC, Pt/C , and $\text{CuO}_x/\text{CeO}_2$ composite for ORR derived from LSV curves at 1600 rpm.

Electrocatalysts	E_{onset} (V vs. Ag/AgCl)	$E_{1/2}$ (V vs. Ag/AgCl)	Limiting current density, j_m (mA cm^{-2})
CeO_2/C	-0.13	-0.31	-3.40
CuO_x/C	-0.13	-0.31	-3.58
$\text{CuO}_x\text{-CeO}_2/\text{C}$	-0.10	-0.30	-5.03
VC	-0.26	-0.44	-1.96
Pt/C	-0.05	-0.15	-3.86
$\text{CuO}_x/\text{CeO}_2$	-0.26	-0.41	-1.51

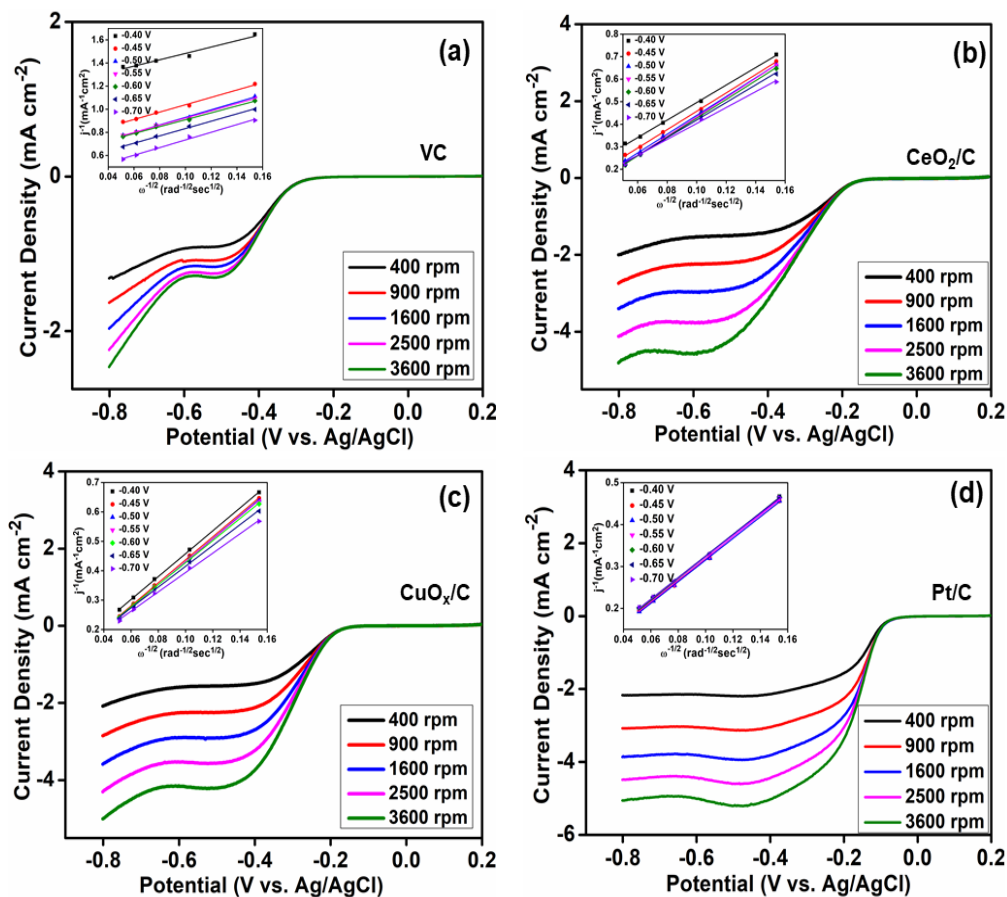


Figure 7. Rotating rate dependent LSV curves (sweep rate = 10 mV s^{-1}) and K–L plots (inset) for (a) VC, (b) CeO_2/C , (c) CuO_x/C and (d) Pt/C in O_2 -saturated 0.1 M KOH electrolyte.

Thus, to probe the ORR activity in depth, LSV curves for the ECs along with VC and Pt/C were also measured at various rotation speeds (400, 900, 1600, 2500 and 3600 rpm) applying a sweep rate of 10 mV s^{-1} in O_2 -saturated electrolyte. Figure 6c and Figure 7 clearly shows that $\text{CuO}_x\text{-CeO}_2/\text{C}$ EC has a promising current density compared to CuO_x/C , CeO_2/C , VC and Pt/C. From LSV curves, the K–L plots were derived at different electrode potential to understand the ORR kinetics. Inset of Figure 6c and Figure 7 shows the K–L plots for $\text{CuO}_x\text{-CeO}_2/\text{C}$ and other ECs, respectively, in the potential range -0.4 to -0.7 V . The K–L plots display good linearity and close parallelism thereby revealing first-order kinetics with respect to the amount of oxygen dissolved in the electrolyte. It is well reported in literatures that ORR proceed either by direct $4e^-$ pathway where the transformation of O_2 to $\text{OH}^-/\text{H}_2\text{O}$ occurs or by indirect $2e^-$ pathway which involves the formation of intermediates (*e.g.*, HO_2^- and OH^-) followed by conversion to $\text{OH}^-/\text{H}_2\text{O}$ depending on the electrolyte used. Thus, electron transfer count is a

crucial parameter to determine the pathway followed during ORR. Figure 6d depicts the K–L plots for different samples and the corresponding number of electrons transferred (n) at -0.65 V. Using the K–L equation, the ‘ n ’ of VC, CeO_2/C , CuO_x/C , $\text{CuO}_x\text{-CeO}_2/\text{C}$ and Pt/C at -0.65 V were calculated to be 2.8, 2.3, 2.5, 3.6 and 3.8 respectively.

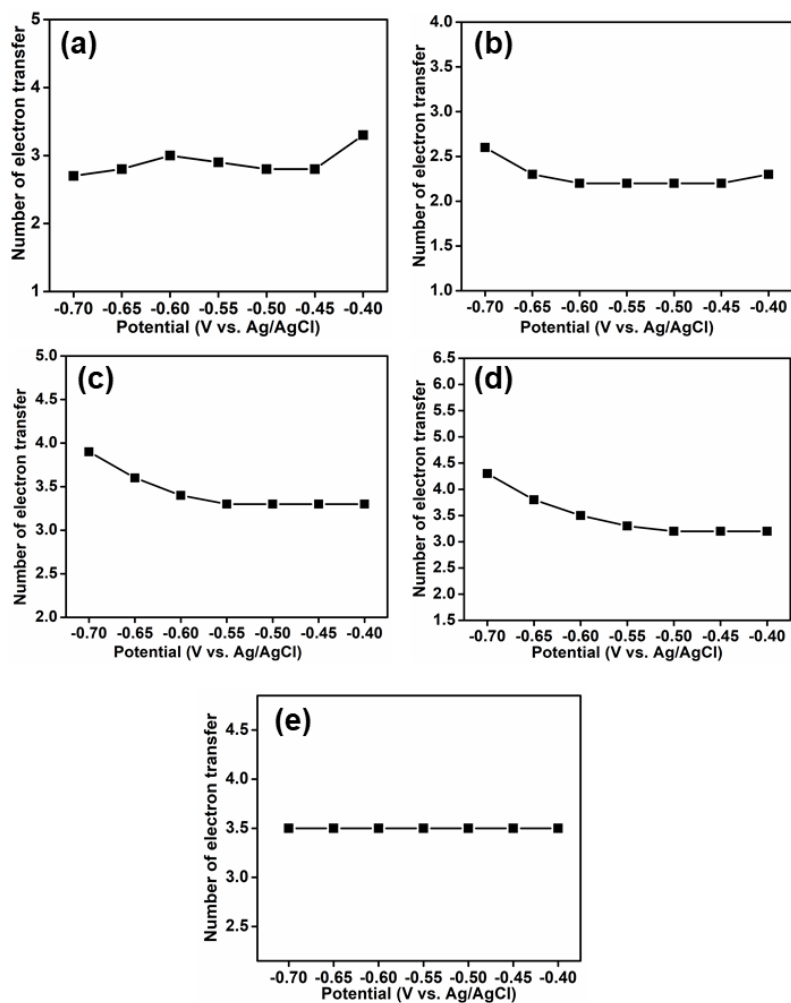


Figure 8. Plots of number of electron transferred (n) vs. potential in the range -0.4 to -0.7 V (vs. Ag/AgCl) for (a) VC, (b) CeO_2/C , (c) CuO_x/C , (d) $\text{CuO}_x\text{-CeO}_2/\text{C}$ and (e) Pt/C .

Figure 8 shows the plots of the ‘ n ’ vs. potential in a wide range -0.4 to -0.7 V. From the ‘ n ’ values it can be concluded that $\text{CuO}_x\text{-CeO}_2/\text{C}$ EC follows a highly favorable direct $4e^-$ pathway during the reaction, similar to that of Pt/C . On the other hand, ORR proceeds via indirect $2e^-$ pathway in the case of CeO_2/C and CuO_x/C ECs. This proves that $\text{CuO}_x\text{-CeO}_2/\text{C}$ is a better EC for ORR than CeO_2/C and CuO_x/C ECs. Figure 6e represents the comparison of mass activities

in the potential region -0.4 to -0.7 V for all ECs at 1600 rpm which shows that the mass activity of $\text{CuO}_x\text{-CeO}_2/\text{C}$ is much higher as compared to that of CuO_x/C and CeO_2/C ECs, while it is comparable to the mass activity of the Pt/C .

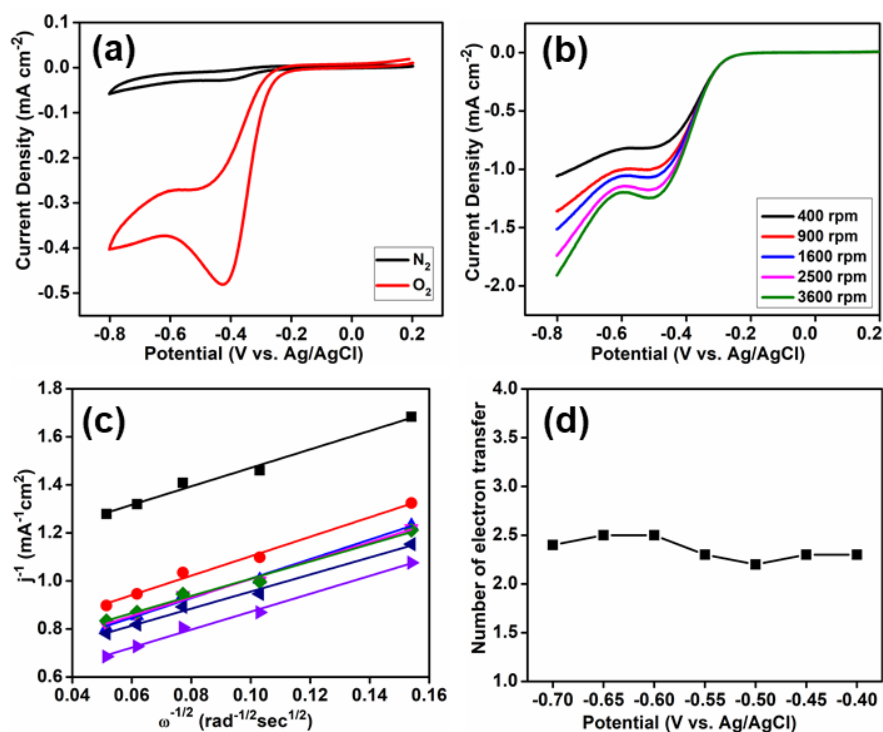


Figure 9. (a) CV plots in N_2 - and O_2 -saturated 0.1 M KOH, (b) Rotating rate dependent LSV curves (sweep rate = 10 mV s^{-1}) in O_2 -saturated 0.1 M KOH, (c) K–L plots and (d) plot of number of electron transferred (n) vs. potential for $\text{CuO}_x/\text{CeO}_2$ composite.

In order to elucidate the role of carbon on the resultant EC, the electrocatalytic activity of the $\text{CuO}_x/\text{CeO}_2$ composite towards ORR was also measured. The current densities at various rotations were observed to be the lowest for $\text{CuO}_x/\text{CeO}_2$ composite compared all other ECs and VC (Figure 9). This is mainly due to the absence of carbon support in the $\text{CuO}_x/\text{CeO}_2$ composite that leads to poor electron conductivity. Moreover, evaluation of K–L plots (Figure 9c) suggested that $\text{CuO}_x/\text{CeO}_2$ composite undergoes ORR via less preferred indirect $2e^-$ pathway. The plot of n in the potential region, -0.4 to -0.7 V is shown in Figure 9d.

Further insight into ORR kinetics can be assessed through Tafel slopes that were obtained in the kinetically controlled part from the linear plot of LSV curves measured at 1600 rpm. As can be observed from Figure 6f, the Tafel slope of $\text{CuO}_x\text{-CeO}_2/\text{C}$ ($65 \text{ mV decade}^{-1}$) is smaller than Pt/C ($68 \text{ mV decade}^{-1}$) implying a faster ORR kinetics and higher activity associated with

$\text{CuO}_x\text{-CeO}_2/\text{C}$ EC. It also implies that a similar reaction mechanism was followed by both the ECs. This is because earlier literatures exclusively reported that when Pt/C is used as an EC, the rate determining step is the first electron transfers to oxygen molecules.

Figure 10a represents the CA responses of $\text{CuO}_x\text{-CeO}_2/\text{C}$ EC and Pt/C. It is evident from the figure that $\text{CuO}_x\text{-CeO}_2/\text{C}$ exhibits higher stability for ORR in alkaline medium with a retention of $\sim 77\%$ of its initial current after 6 h of the experimental operation. On the other hand, Pt/C shows a faster initial current loss of the reaction and retains 72.1% of its initial current density after 6 h, indicating its inferiority over $\text{CuO}_x\text{-CeO}_2/\text{C}$ EC.

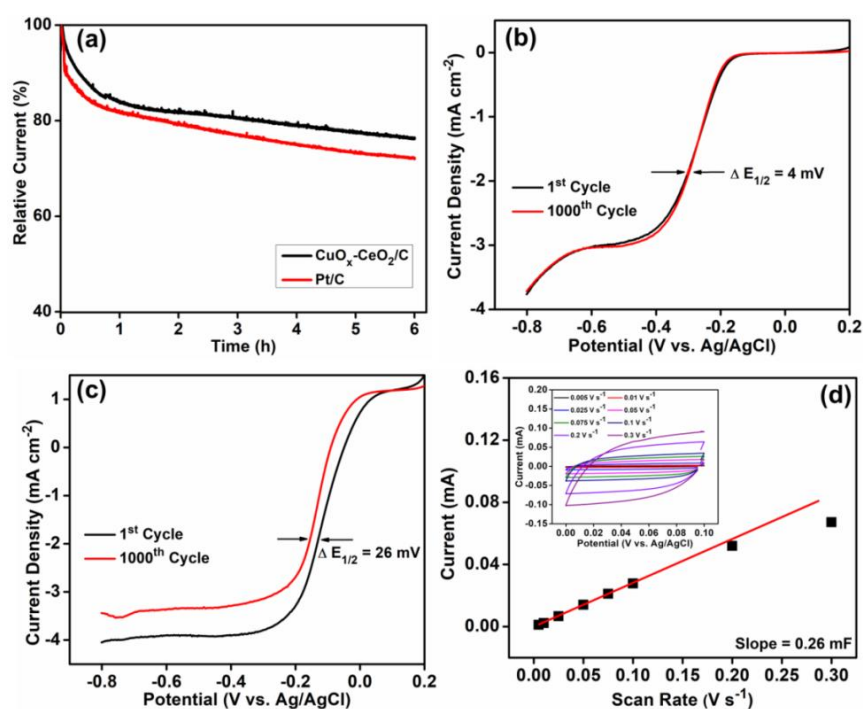


Figure 10. (a) CA curves of $\text{CuO}_x\text{-CeO}_2/\text{C}$ EC and Pt/C recorded at -0.3 V in O_2 -saturated 0.1 M KOH electrolyte at 1600 rpm, LSV curves of (b) $\text{CuO}_x\text{-CeO}_2/\text{C}$ and (c) Pt/C at 1600 rpm before and after the ADT up to 1000 cycles and (d) CVs in a non-Faradaic region of the voltammogram for $\text{CuO}_x\text{-CeO}_2/\text{C}$ EC in N_2 -saturated 0.1 M KOH electrolyte at different scan rates (inset) and the corresponding plot of anodic charging current as a function of scan rate at 0.05 V.

Accelerated durability test (ADT) was carried out to evaluate and compare the durability of $\text{CuO}_x\text{-CeO}_2/\text{C}$ EC with Pt/C up to 1000 CV cycles as shown in Figure 10b,c. The difference in $\Delta E_{1/2}$ for LSV curve recorded at 1600 rpm before and after 1000 cycles is very small for $\text{CuO}_x\text{-CeO}_2/\text{C}$ EC ($\Delta E_{1/2} = 4$ mV), while, for Pt/C a difference of 26 mV is observed. Moreover, a

clear drop of onset potential is observed in the case of Pt/C with a negative shift of 40 mV, whereas, the onset potential of $\text{CuO}_x\text{-CeO}_2/\text{C}$ EC remains almost intact after 1000 cycles which proves better cycling stability of $\text{CuO}_x\text{-CeO}_2/\text{C}$ EC compared to that of Pt/C. The improved stability and durability of $\text{CuO}_x\text{-CeO}_2/\text{C}$ EC can be ascribed to the synergistic presence of CuO_x , CeO_2 and the carbon support which brings about an electronic alteration in the resultant structure with improved activity. The electrochemically active surface area (ECSA) is one of the crucial parameters of an EC to estimate the electrochemically active sites.

Insets of Figure 10d and Figure 11a,b show the scan rate dependent CVs in a non-Faradaic region for electrochemical double-layer capacitance (C_{DL}) measurement of $\text{CuO}_x\text{-CeO}_2/\text{C}$, CeO_2/C and CuO_x/C ECs. As expected, the corresponding plot of anodic charging current versus scan rate at 0.05 V has a linear relationship, the slope of which gives C_{DL} . The C_{DL} values for the ECs follow the order: $\text{CuO}_x\text{-CeO}_2/\text{C}$ (0.28 mF) > CeO_2/C (0.22 mF) > CuO_x/C (0.05 mF). Generally, higher the value of C_{DL} , higher will be its exposed electrochemically active sites which promote satisfactory mass transfer of O_2 . The corresponding value of ECSA per gram of the EC is found to be the highest for $\text{CuO}_x\text{-CeO}_2/\text{C}$ ($23.33 \text{ m}^2 \text{ g}^{-1}$) than those of CeO_2/C ($18.33 \text{ m}^2 \text{ g}^{-1}$) and CuO_x/C ($4.17 \text{ m}^2 \text{ g}^{-1}$). Therefore, $\text{CuO}_x\text{-CeO}_2/\text{C}$ EC owns more exposed active sites which in turn contribute to its enhanced electrocatalytic activity.

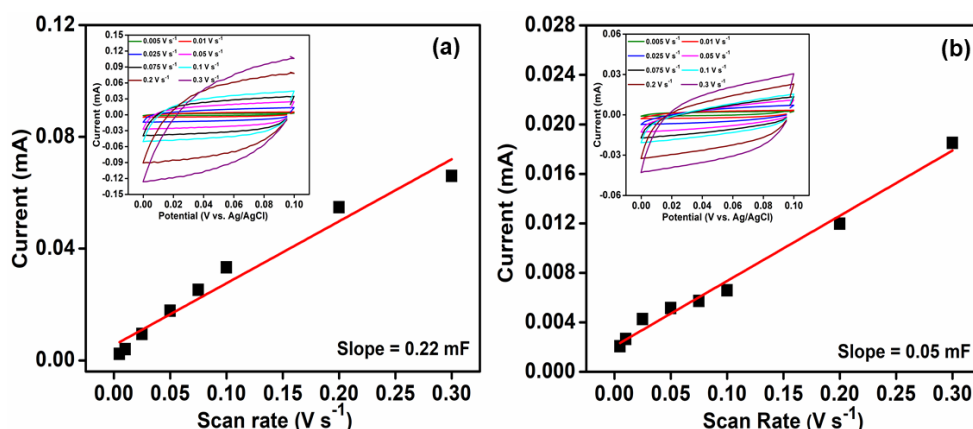


Figure 11. CVs in a non-Faradaic region of the voltammogram for (a) CeO_2/C and (b) CuO_x/C ECs in N_2 -saturated 0.1 M KOH electrolyte at different scan rates (inset) and the corresponding plot of anodic charging current as a function of scan rate at 0.05 V (vs. Ag/AgCl).

Electrocatalytic oxygen evolution activity related to $\text{CuO}_x\text{-CeO}_2/\text{C}$, CuO_x/C and CeO_2/C ECs:

The electrocatalytic OER performance of CeO_2/C , CuO_x/C and $\text{CuO}_x\text{-CeO}_2/\text{C}$ ECs was measured using RDE in N_2 -saturated 0.1 M KOH electrolyte at a rotation speed and sweep rate

of 1600 rpm and 10 mV s^{-1} , respectively. The corresponding potential window was 0.2 to 1.5 V. It is already reported that 10 mA cm^{-2} (j_{10}) is the average current density for 10% proficient energy conversion in a water-splitting device. Clearly, the LSV curves in Figure 12a show that $\text{CuO}_x\text{-CeO}_2/\text{C}$ EC attained 10 mA cm^{-2} at an overpotential (η_{10}) of 0.58 V which is 120 mV lower than that of CuO_x/C (0.70 V), suggesting higher efficiency of $\text{CuO}_x\text{-CeO}_2/\text{C}$ for OER. The corresponding potentials at j_{10} i.e., $E_{j_{10}}$ for CuO_x/C and $\text{CuO}_x\text{-CeO}_2/\text{C}$ are 0.94 and 0.82 V (vs. Ag/AgCl), respectively. Although, CeO_2/C has very low activity towards OER, however, its combination with CuO_x/C in the resultant EC made an obvious difference with enhanced OER performance. Moreover, E_{onset} for $\text{CuO}_x\text{-CeO}_2/\text{C}$ EC (0.20 V) is also more negative as compared to CuO_x/C (0.24 V) and CeO_2/C (0.81 V), suggesting its enriched OER activity.

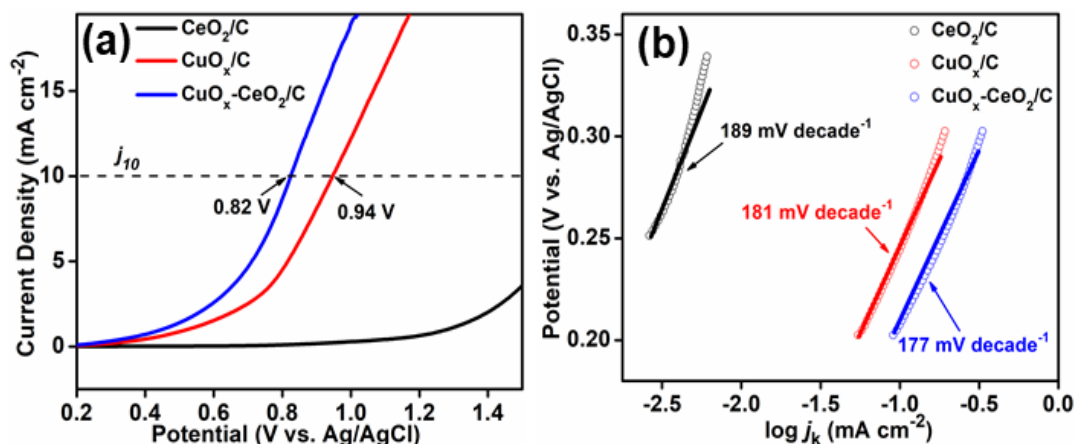


Figure 12. (a) LSV curves at 1600 rpm in the potential range 0.2 to 1.5 V and (b) Tafel plots of CeO_2/C , CuO_x/C and $\text{CuO}_x\text{-CeO}_2/\text{C}$ for OER.

Table 3. Summary of E_{onset} , $E_{j_{10}}$, overpotential at 10 mA cm^{-2} (η_{10}) and Tafel slopes of various ECs and RuO_2 for OER derived from LSV curve at 1600 rpm.

Electrocatalysts	E_{onset} (V vs. Ag/AgCl)	$E_{j_{10}}$ (V vs. Ag/AgCl)	η_{10} (V vs. Ag/AgCl)	Tafel slope (mV decade^{-1})
CeO_2/C	0.81	–	–	189
CuO_x/C	0.24	0.94	0.70	181
$\text{CuO}_x\text{-CeO}_2/\text{C}$	0.20	0.82	0.58	177

The OER kinetics of the ECs is further investigated by Tafel plots as shown in Figure 12b. Notably, $\text{CuO}_x\text{-CeO}_2/\text{C}$ EC has the smallest Tafel slope of $177 \text{ mV decade}^{-1}$ in low current density region among CeO_2/C and CuO_x/C ECs, indicating that $\text{CuO}_x\text{-CeO}_2/\text{C}$ has faster rate of

oxygen evolution at the anode. The values of E_{onset} , $E_{j_{10}}$, η_{10} and Tafel slopes for all the ECs are summarized in Table 3. These results reflect the superiority of $\text{CuO}_x\text{-CeO}_2/\text{C}$ EC among all the samples towards OER in alkaline medium.

Characterization related to $\text{Co}_3\text{O}_4\text{-CeO}_2/\text{C}$ hybrid, $\text{Co}_3\text{O}_4/\text{C}$ and CeO_2/C

XRD analysis: The crystalline phases of CeO_2/C , $\text{Co}_3\text{O}_4/\text{C}$ and $\text{Co}_3\text{O}_4\text{-CeO}_2/\text{C}$ hybrid ECs were characterized by p-XRD as shown in Figure 13a. All the diffraction peaks centered at $2\theta = 19^\circ$, 31.27° , 36.85° , 44.81° , 59.29° and 65.23° match well with various crystalline facets of Co_3O_4 according to the JCPDS No. 42-1467. The prominent peaks appearing at $2\theta = 28.5^\circ$, 33.1° , 47.5° , 56.3° , 69.4° , 76.7° and 79.1° are in good agreement with the different crystalline planes of face centered cubic (*fcc*) fluorite CeO_2 (JCPDS No. 45-0937). The reduction in intensity of the peaks in the $\text{Co}_3\text{O}_4\text{-CeO}_2/\text{C}$ hybrid indicates that $\text{Co}_3\text{O}_4\text{-CeO}_2$ particles are smaller as compared to that of CeO_2 and Co_3O_4 particles. A faint and very low crystalline peak at around 24° is ascribed to the carbon support (JCPDS No. 75-1621). All the peaks correspond to the different planes of CeO_2 and Co_3O_4 were appeared in the $\text{Co}_3\text{O}_4\text{-CeO}_2/\text{C}$ hybrid, suggesting the co-existence of CeO_2 and Co_3O_4 phases. Moreover, the highly crystalline nature of the diffraction peaks ensures high electrical conductivity. Compared to that of CeO_2/C and $\text{Co}_3\text{O}_4/\text{C}$, the crystallite size of the $\text{Co}_3\text{O}_4\text{-CeO}_2/\text{C}$ hybrid determined by using Scherrer's equation is found to be smaller (Table 4).

FTIR analysis: Further insight into the structural details of the ECs was investigated using FTIR. Figure 13b presents the FTIR spectra of CeO_2/C , $\text{Co}_3\text{O}_4/\text{C}$ and $\text{Co}_3\text{O}_4\text{-CeO}_2/\text{C}$ hybrid ECs. The peak at 656 cm^{-1} can be attributed to Co^{2+} in tetrahedral holes and that at 564 cm^{-1} corresponds to Co^{3+} in octahedral holes, which are the characteristics of Co_3O_4 in its spinel form. It is reported that the Co-Co interactions through the octahedral edges in a spinel structure directly influences the electrocatalytic activity via enhanced electronic conductivity. The various peaks in the range $1460\text{-}1240\text{ cm}^{-1}$ are the characteristics of CeO_2 , which appear as a broad peak in the $\text{Co}_3\text{O}_4\text{-CeO}_2/\text{C}$ hybrid. The peaks at 3424 and 1627 cm^{-1} can be respectively assigned to the -OH bending and stretching vibrations of the residual water molecules. All the peaks correspond to Co_3O_4 and CeO_2 can be observed in the $\text{Co}_3\text{O}_4\text{-CeO}_2/\text{C}$ hybrid, confirming its formation.

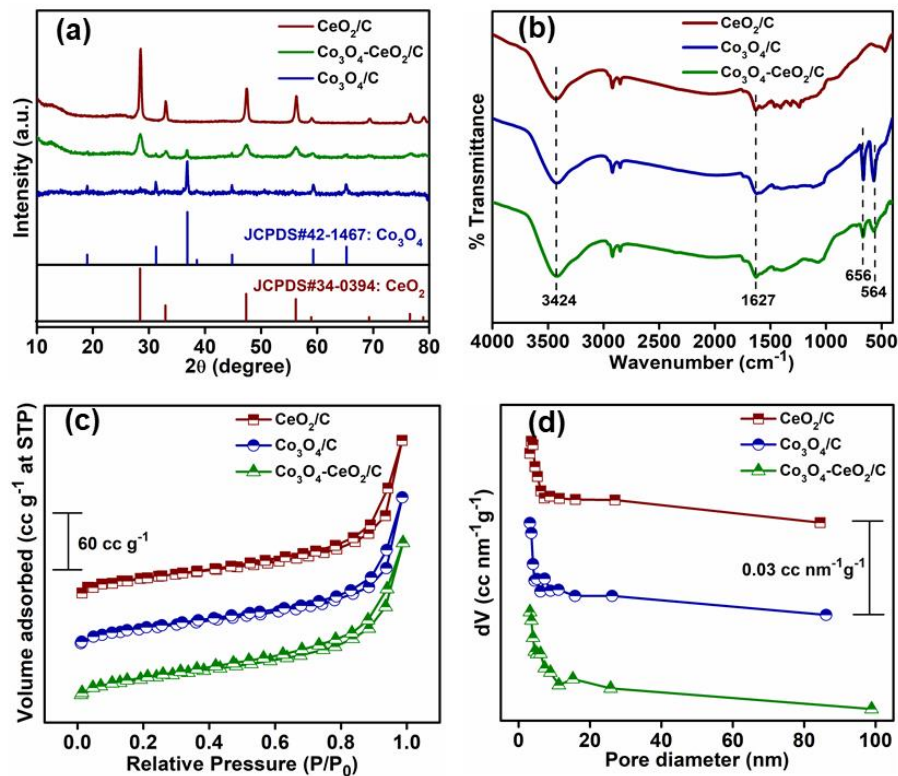


Figure 13. (a) p-XRD patterns, (b) FTIR spectra, (c) N₂ adsorption/desorption isotherms, and (d) corresponding pore size distribution curves of CeO₂/C, Co₃O₄/C and Co₃O₄-CeO₂/C hybrid ECs.

Table 4. Summary of structural parameters for CeO₂/C, Co₃O₄/C and Co₃O₄-CeO₂/C hybrid ECs obtained from XRD and BET surface area analyses

Material	Specific surface area (m ² g ⁻¹)	Pore diameter (nm)	Pore volume (cc g ⁻¹)	Crystallite size (nm)
CeO ₂ /C	135.9	3.1	0.25	23.8
Co ₃ O ₄ /C	151.5	3.1	0.24	11.6
Co ₃ O ₄ -CeO ₂ /C hybrid	165.5	3.1	0.25	9.0

BET surface area analysis: The specific surface area and porous nature of the synthesized ECs were determined by the N₂ adsorption/desorption analyses obtained at -196 °C. Figure 13c clearly represents that the N₂ adsorption/desorption isotherms of CeO₂/C, Co₃O₄/C and Co₃O₄-CeO₂/C hybrid follows Type IV isotherm with a distinct H3 type hysteresis loop in relatively high pressure region (*i.e.*, 0.8–0.1), which is an indication of mesoporosity. The

textural properties obtained from the N₂ adsorption/desorption experiment are also summarized in Table 4. All the synthesized ECs have a pore diameter of 3.1 nm, confirming the presence of mesopores in their structure. Figure 13d shows the corresponding Barrett-Joyner-Halenda (BJH) pore size distribution curves. The specific surface area determined using BET multipoint method shows that Co₃O₄-CeO₂/C hybrid (165.5 m² g⁻¹) has higher surface area as compared to that of CeO₂/C (135.9 m² g⁻¹) and Co₃O₄/C (151.5 m² g⁻¹) ECs.

Raman Analysis: Figure 14a represents the Raman spectra of CeO₂/C, Co₃O₄/C and Co₃O₄-CeO₂/C hybrid ECs, where two distinct peaks at ~1344.4 and ~1590 cm⁻¹ corresponds to the D (arising from the disordered sp³-hybridized carbon atom) and G bands (attributed to the disordered graphitic carbon with sp² hybridization). A sharp peak at ~459 cm⁻¹ could be indexed to the F_{2g} vibrational mode of CeO₂ with symmetric Ce-O-Ce stretching. Four Raman active modes 191.3 cm⁻¹ (F_{2g}²), 468.8 cm⁻¹ (E_g), 515 cm⁻¹ (F_{2g}¹) and 678.7 cm⁻¹ (A_{1g}) confirms the cubic phase of Co₃O₄. Most of the vibrational modes related to CeO₂ and Co₃O₄ are observed in the Raman spectrum of Co₃O₄-CeO₂/C hybrid which supports its formation.

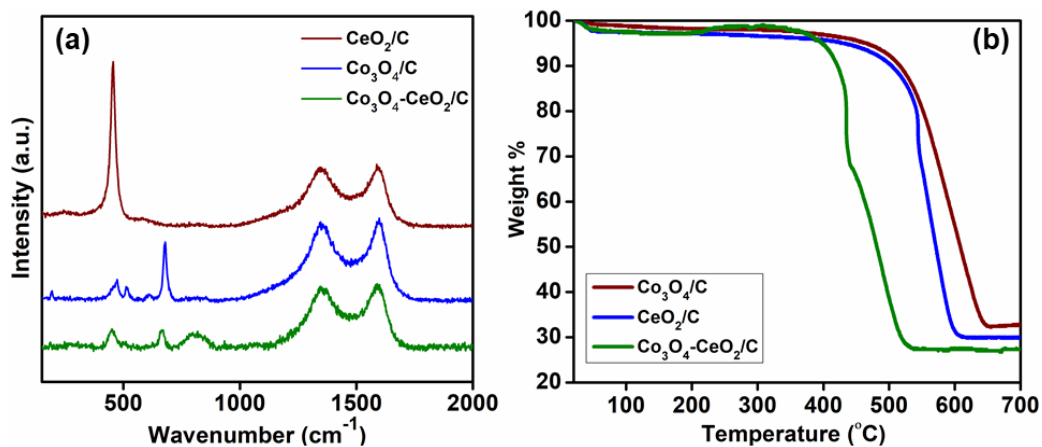


Figure 14. (a) Raman spectra and (b) TGA curves in air atmosphere for Co₃O₄/C, CeO₂/C and Co₃O₄-CeO₂/C hybrid ECs.

TGA analysis: The total MO loading over the carbon support was established from the TGA curves of the ECs. Figure 14b in the present the TGA curves of Co₃O₄/C, CeO₂/C and Co₃O₄-CeO₂/C hybrid ECs. The TGA analysis shows a weight loss at about 450–500 °C due to oxidative conversion of carbon from the sample after heating it in air. For Co₃O₄-CeO₂/C hybrid, no weight loss is observed in the TGA pattern after 530 °C. The residue left after

oxidation was found to be 28% that is very close to the theoretically targeted value *i.e.*, 30%. Similarly, $\text{Co}_3\text{O}_4/\text{C}$ and CeO_2/C also attains a steady state after 600 °C.

EDX analysis: Figure 15a,b in the Supporting Information shows the EDX spectrum and the SEM image of the $\text{Co}_3\text{O}_4\text{-CeO}_2/\text{C}$ hybrid. The Co/Ce atomic ratio deduced from EDS study (inset of Figure 15a) confirms that Co (0.31) and Ce (0.36) existed in nearly 1:1 ratio, which is consistent with the theoretical values. Moreover, the total loading of $\text{Co}_3\text{O}_4\text{-CeO}_2$ (29.62%) on the carbon support (70.38%) obtained from EDX analysis corroborates well with the TGA results. The corresponding elemental maps that verify the presence and uniform distribution of C, O, Co and Ce elements are shown in Figure 15c–f.

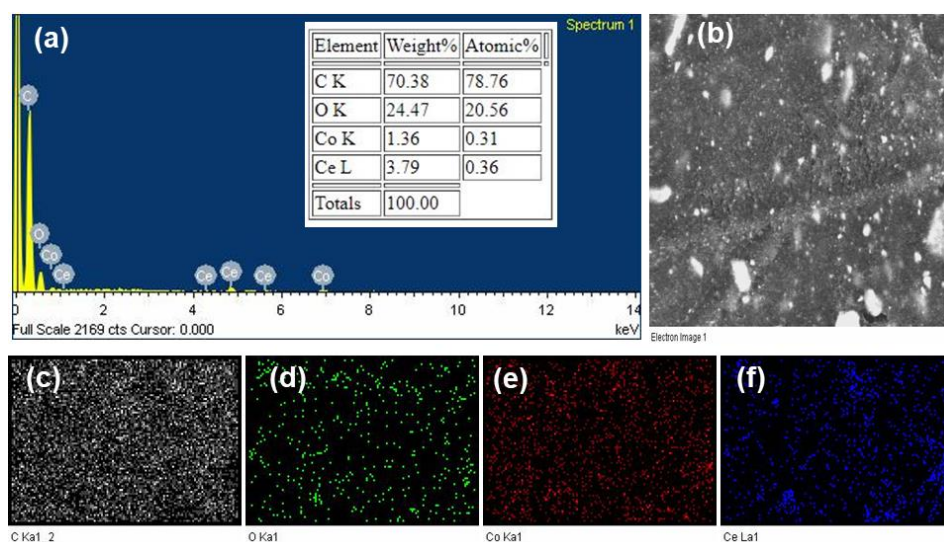


Figure 15. a) EDX spectrum of $\text{Co}_3\text{O}_4\text{-CeO}_2/\text{C}$ hybrid EC; inset shows the table for elemental composition, (b) the corresponding SEM image and, (c-f) elemental maps for individual C, O, Co and Ce.

TEM analysis: The microstructure and size of the $\text{Co}_3\text{O}_4\text{-CeO}_2/\text{C}$ hybrid was investigated by means of TEM and HRTEM analyses as depicted in Figure 16. It is understandable from Figure 16a that the $\text{Co}_3\text{O}_4\text{-CeO}_2$ particles assume spherical morphology and are evenly dispersed over the carbon matrix of relatively larger size. The tiny oxide particles have diameter in the range of 8–18 nm with an average diameter of 12 nm as determined from the particle size distribution plot, shown in Figure 16b. Figure 16c represents an HRTEM image of $\text{Co}_3\text{O}_4\text{-CeO}_2/\text{C}$ hybrid showing distinct oxide/carbon and oxide/oxide interfaces that are denoted by black and yellow dashed lines, respectively. Figure 16d and Figure 16f are the HRTEM images obtained from

highly magnified portions of a particular region in Figures 16c and 16e, respectively. The d -spacing of 0.19 and 0.31 nm, respectively, corresponds to the (220) and (111) planes of CeO_2 , while, the d -spacing of 0.25 and 0.28 nm can be attributed to the (311) and (220) planes of Co_3O_4 . These results corroborate well with the p-XRD pattern of $\text{Co}_3\text{O}_4\text{-CeO}_2/\text{C}$ hybrid.

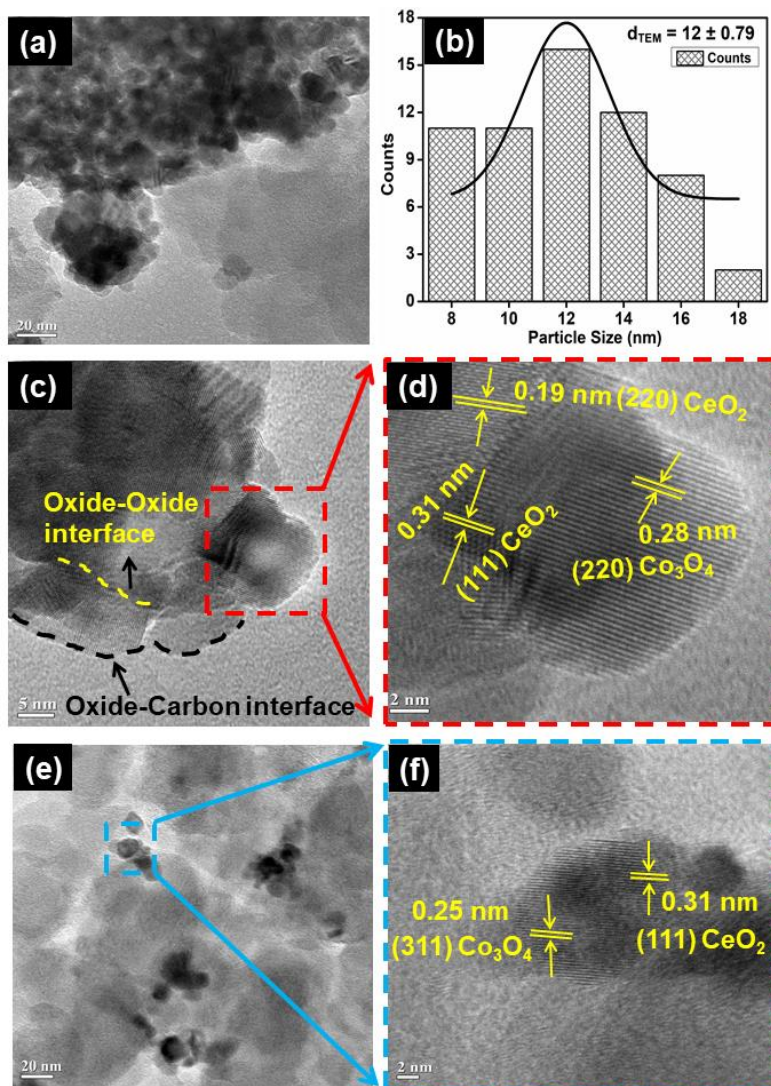


Figure 16. (a) Low magnification TEM image, (b) the corresponding particle size distribution curve and (c)-(f) HRTEM images with distinguished lattice fringes and hetero-interfaces for $\text{Co}_3\text{O}_4\text{-CeO}_2/\text{C}$ hybrid.

XPS analysis: The survey spectrum revealed the presence of C, O, Co and Ce in $\text{Co}_3\text{O}_4\text{-CeO}_2/\text{C}$ hybrid with no other elements detected as shown in Figure 17a, suggesting high purity of the sample. The survey spectrum of CeO_2/C and $\text{Co}_3\text{O}_4/\text{C}$ were represented in Figure 17b and

Figure 17b, respectively, which confirms the existence of only detectable elements in the corresponding samples.

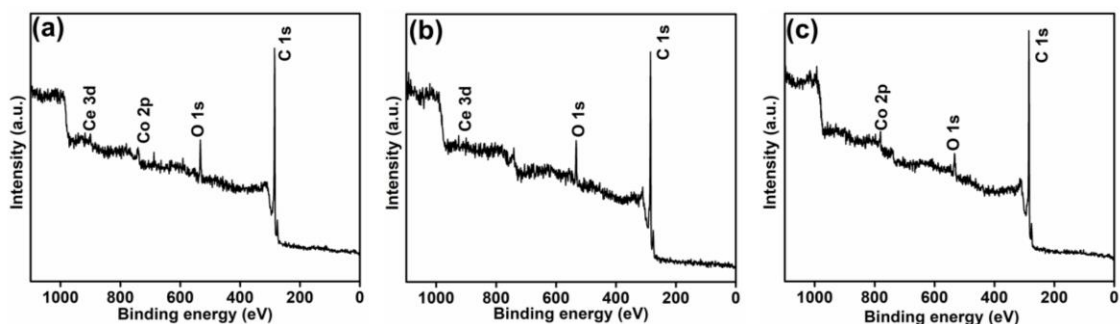


Figure 17. Survey spectrum of (a) $\text{Co}_3\text{O}_4\text{-CeO}_2/\text{C}$, (b) CeO_2/C and (c) $\text{Co}_3\text{O}_4/\text{C}$.

Figures 18a-c are the high resolution XP spectra of C 1s for the $\text{Co}_3\text{O}_4\text{-CeO}_2/\text{C}$ hybrid, CeO_2/C , and $\text{Co}_3\text{O}_4/\text{C}$ ECs, respectively. C 1s spectrum is further resolved into three components at BEs of 288.6, 285.3 and 284.5 eV that corresponds to $\text{O}=\text{C}-\text{O}$, $-\text{C}-\text{O}-$ and $-\text{C}=\text{C}-$ groups, respectively.

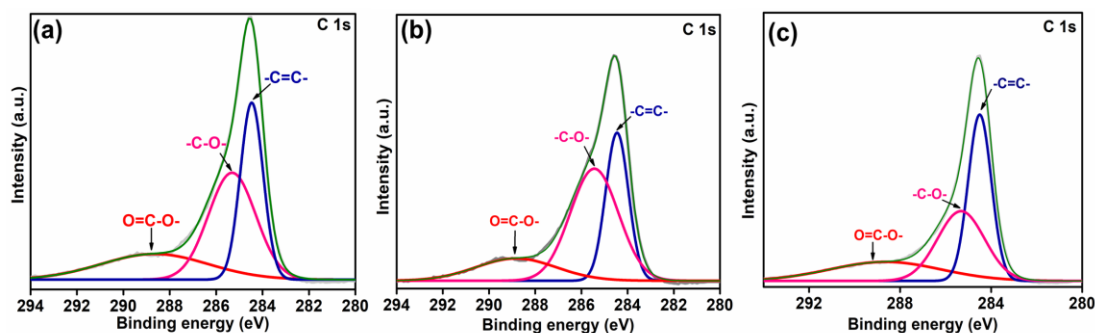


Figure 18. High resolution C 1s XP spectra of (a) $\text{Co}_3\text{O}_4\text{-CeO}_2/\text{C}$ hybrid, (b) CeO_2/C , and (c) $\text{Co}_3\text{O}_4/\text{C}$.

The peak fitting of the high resolution O 1s spectra of CeO_2/C , $\text{Co}_3\text{O}_4/\text{C}$ and $\text{Co}_3\text{O}_4\text{-CeO}_2/\text{C}$ hybrid ECs gives three characteristic peaks, as shown in Figure 19a. The peaks at 530.1 eV (CeO_2/C) and 529.9 eV ($\text{Co}_3\text{O}_4/\text{C}$) are the characteristic metal-oxygen bond in the lattice (O_a), the peaks at 532.6 eV (CeO_2/C) and 532.0 eV ($\text{Co}_3\text{O}_4/\text{C}$) are indexed to low-coordinated oxygen vacancies (O_b), while, the peaks ~ 534.1 eV (CeO_2/C) and ~ 533.6 eV ($\text{Co}_3\text{O}_4/\text{C}$) are the physically adsorbed water molecules on the surface of MOs (O_c). Most of the peaks related to O 1s of the $\text{Co}_3\text{O}_4\text{-CeO}_2/\text{C}$ hybrid were shifted to higher values. This might be due to the

electronic rearrangement that takes place due to electronic interaction between Co_3O_4 and CeO_2 phases. Notably, the percentage of O_b and the ratio O_b/O_a was found to be the highest for $\text{Co}_3\text{O}_4\text{-CeO}_2/\text{C}$ hybrid (58% and 4.6) in comparison to that of CeO_2/C (43.8% and 3.5) and $\text{Co}_3\text{O}_4/\text{C}$ (52.2% and 2.7), implying a higher concentration of surface oxygen vacancies in the former. The percentage of various oxygen species and the corresponding O_b/O_a ratio were summarized in Table 5.

Table 5. Percentage of various oxygen species obtained from XPS analysis for CeO_2/C , $\text{Co}_3\text{O}_4/\text{C}$ and $\text{Co}_3\text{O}_4\text{-CeO}_2/\text{C}$ hybrid.

ECs	O_a (%)	O_b (%)	O_c (%)	Ratio O_b/O_a
CeO_2/C	12.3	43.8	43.8	3.5
$\text{Co}_3\text{O}_4/\text{C}$	19.3	52.2	28.4	2.7
$\text{Co}_3\text{O}_4\text{-CeO}_2/\text{C}$	12.7	58.0	29.4	4.6

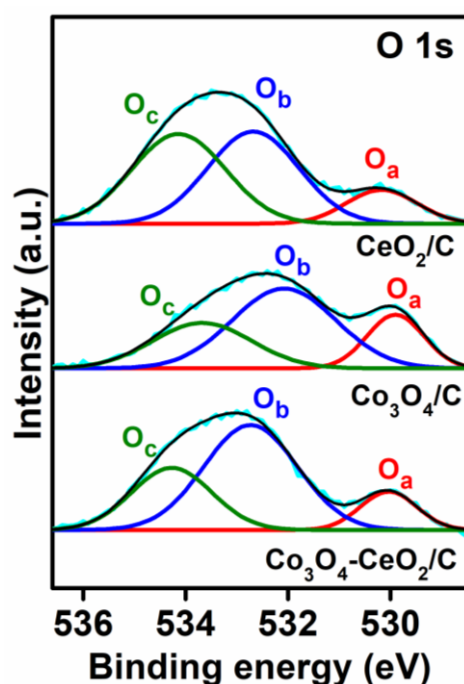


Figure 19. High resolution XP spectra of O 1s for CeO_2/C , $\text{Co}_3\text{O}_4/\text{C}$ and $\text{Co}_3\text{O}_4\text{-CeO}_2/\text{C}$ hybrid.

Figures 20a,b represents the Co 2p spectrum of $\text{Co}_3\text{O}_4\text{-CeO}_2/\text{C}$ hybrid and $\text{Co}_3\text{O}_4/\text{C}$, respectively, which consists of a doublet located at ~ 780.4 eV ($\text{Co } 2p_{3/2}$) and ~ 795.4 eV ($\text{Co } 2p_{1/2}$) with a spin orbit splitting of 15.1 eV, along with two satellite peaks located at ~ 786.9 and ~ 803.9 eV. $\text{Co } 2p_{3/2}$ and $\text{Co } 2p_{1/2}$ are further resolved into two components corresponding to

Co³⁺ and Co²⁺ species, where Co²⁺ is assigned to higher BE in accordance with the formerly reported literatures. For Co₃O₄-CeO₂/C hybrid, the peaks at 782.0 and 797.9 eV are attributed to Co²⁺, while, the peaks at 780.2 and 795.4 eV are ascribed to Co³⁺. These results are consistent with the spinel structure of Co₃O₄ where the high spin Co²⁺ ($t_{2g}^5 e_g^2$) ions occupy one-eighth of the tetrahedral sites and low spin Co³⁺ ($t_{2g}^6 e_g^0$) occupy one-half of the octahedral sites with oxide ions (O²⁻) in the closed packed *fcc* lattice. The BE values related to Co³⁺ and Co²⁺ species in both Co₃O₄/C and Co₃O₄-CeO₂/C hybrid are summarized in Table 6. Clearly, all the peaks in Co₃O₄-CeO₂/C hybrid undergo a shift towards high BE (upshift) than that of Co₃O₄/C, indicating strong coupling between the electron clouds of Co₃O₄ and CeO₂ in the resultant hybrid. Previous studies revealed that the Co²⁺/Co³⁺ ratio is directly proportional to the amount of surface oxygen vacancy in a sample and also indicates the presence of defective sites in Co₃O₄. The Co²⁺/Co³⁺ ratio for Co₃O₄/C and Co₃O₄-CeO₂/C hybrid are respectively 0.99 and 1.1, which confirms higher oxygen vacancy in Co₃O₄-CeO₂/C hybrid.

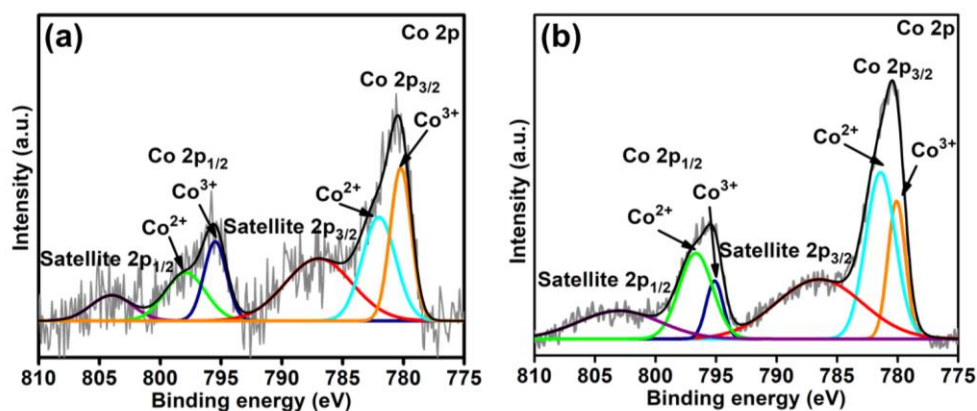


Figure 20. High resolution XP spectra of Co 2p for (a) Co₃O₄-CeO₂/C hybrid and (b) Co₃O₄/C.

Table 6. Comparison of BE values of Co²⁺ and Co³⁺ in Co₃O₄/C and Co₃O₄-CeO₂/C hybrid

Multiplets	Species	BE for Co ₃ O ₄ /C (in eV)	BE for Co ₃ O ₄ -CeO ₂ /C hybrid (in eV)	Shift in BE (in eV)
Co 2p _{3/2}	Co ²⁺	781.4	782.0	0.6
	Co ³⁺	780.0	780.2	0.2
Co 2p _{1/2}	Co ²⁺	796.6	797.9	1.3
	Co ³⁺	795.1	795.4	0.3

Figures 21a,b show the Ce 3d core level spectra for Co₃O₄-CeO₂/C hybrid and CeO₂/C, respectively. The spectra are composed of two multiplets *i.e.*, Ce 3d_{5/2} (denoted by *v*) and Ce

$3d_{3/2}$ (denoted by u). The peak fitting of these multiplets give rise to eight peaks at various BEs for both CeO_2/C and $\text{Co}_3\text{O}_4\text{-CeO}_2/\text{C}$ hybrid and are labeled as $u, u', u'', u''', v, v', v''$ and v''' on the basis of earlier reports. The u' and v'' components are associated with Ce^{3+} , while the rest six peaks (u, u'', u''', v, v' and v''') confirmed the presence of Ce^{4+} . These results proved the co-existence of Ce^{3+} and Ce^{4+} in CeO_2/C and $\text{Co}_3\text{O}_4\text{-CeO}_2/\text{C}$ hybrid. The presence of Ce^{3+} ions is also an indication of defective ceria that ensures oxygen vacancies in both CeO_2/C and $\text{Co}_3\text{O}_4\text{-CeO}_2/\text{C}$ hybrid ECs. The relative percentage of Ce^{3+} for $\text{Co}_3\text{O}_4\text{-CeO}_2/\text{C}$ hybrid (34%) and CeO_2/C (35%) is comparable.

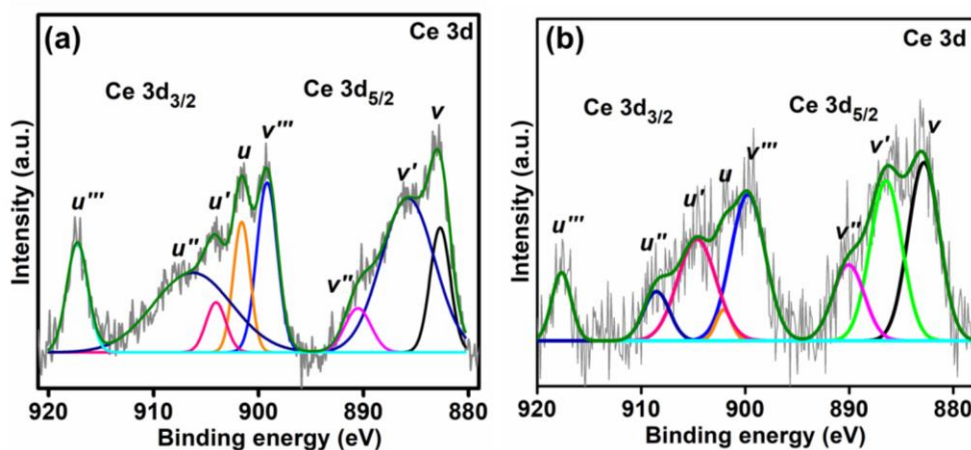


Figure 21. High resolution XP spectra of Ce 3d for (a) $\text{Co}_3\text{O}_4\text{-CeO}_2/\text{C}$ hybrid and (b) $\text{Co}_3\text{O}_4/\text{C}$.

The CV curves of the synthesized ECs along with VC and Pt/C recorded at a scan rate of 50 mV s^{-1} are represented in Figure 22a. An obvious reduction peak can be observed in O_2 -saturated 0.1 M KOH electrolyte, whereas no such peak is observed in N_2 -saturated electrolyte, suggesting good ORR performance of the measured ECs. Notably, the reduction potential values of $\text{Co}_3\text{O}_4\text{-CeO}_2/\text{C}$ hybrid and Pt/C are identical, emphasizing the active nature of the hybrid towards ORR like the Pt/C, which is considered as the standard for ORR. The LSV curves at 1600 rpm for all the samples in O_2 -saturated electrolyte are represented in Figure 22b. VC and $\text{Co}_3\text{O}_4/\text{CeO}_2$ are relatively found to be less active towards ORR. However, the combination of both in the resultant hybrid *i.e.*, $\text{Co}_3\text{O}_4\text{-CeO}_2/\text{C}$ significantly enhances the ORR activity. This can be attributed to the robust electronic interaction between the oxide and carbon phases and the generation of oxide/carbon interfaces that lead to improved ORR performance. The E_{onset} values of $\text{Co}_3\text{O}_4\text{-CeO}_2/\text{C}$, $(\text{Co}_3\text{O}_4+\text{CeO}_2) + \text{C}$, $\text{Co}_3\text{O}_4/\text{CeO}_2$, $\text{Co}_3\text{O}_4/\text{C}$, CeO_2/C , Pt/C and VC are $-0.12, -0.14, -0.22, -0.12, -0.13, -0.05$ and -0.26 V , respectively. Similarly, $E_{1/2}$

values of $\text{Co}_3\text{O}_4\text{-CeO}_2/\text{C}$, $(\text{Co}_3\text{O}_4+\text{CeO}_2) + \text{C}$, $\text{Co}_3\text{O}_4/\text{CeO}_2$, $\text{Co}_3\text{O}_4/\text{C}$, CeO_2/C , Pt/C and VC are -0.27 , -0.32 , -0.40 , -0.27 , -0.31 , -0.15 and -0.44 V, respectively.

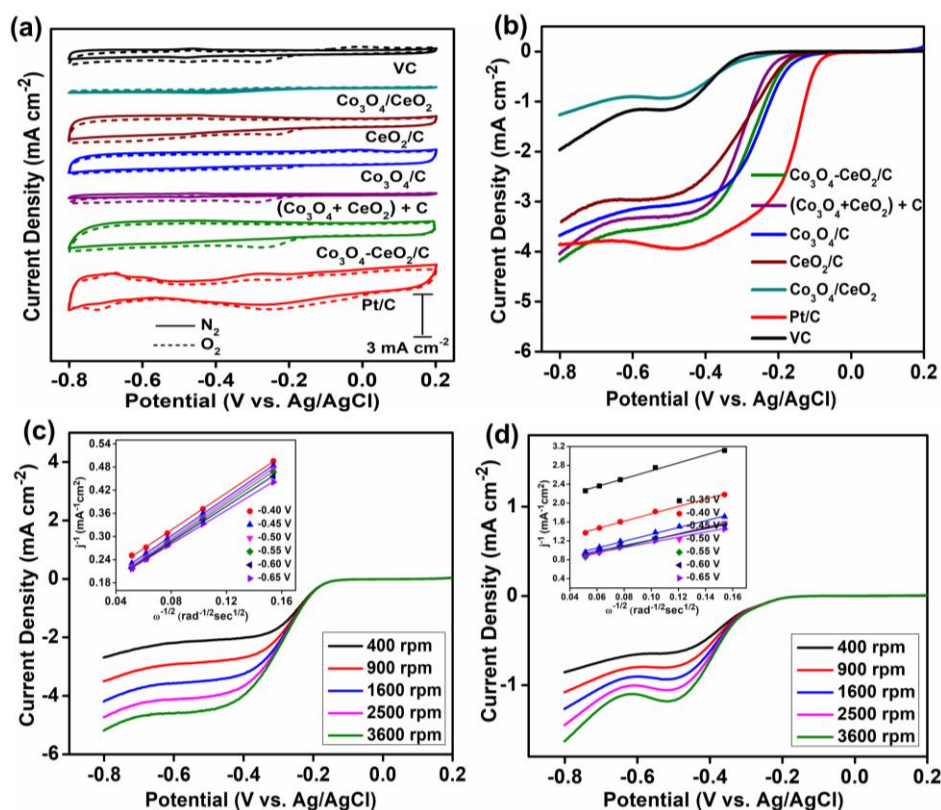


Figure 22. (a) CVs in N_2 - and O_2 -saturated 0.1 M KOH solution, (b) rotating rate dependent LSV plots (scan rate = 10 mV s^{-1}) in O_2 -saturated 0.1 M KOH solution for $\text{Co}_3\text{O}_4\text{-CeO}_2/\text{C}$ hybrid, $(\text{Co}_3\text{O}_4+\text{CeO}_2) + \text{C}$, $\text{Co}_3\text{O}_4/\text{C}$, CeO_2/C , $\text{Co}_3\text{O}_4/\text{CeO}_2$, Pt/C and VC , LSV plots at various rotations of (c) $\text{Co}_3\text{O}_4\text{-CeO}_2/\text{C}$ hybrid and (d) $\text{Co}_3\text{O}_4/\text{CeO}_2$, in O_2 -saturated 0.1 M KOH (Inset of c, d: K–L plots of $\text{Co}_3\text{O}_4\text{-CeO}_2/\text{C}$ hybrid and $\text{Co}_3\text{O}_4/\text{CeO}_2$, respectively).

These values indicate that the E_{onset} and $E_{1/2}$ of $\text{Co}_3\text{O}_4\text{-CeO}_2/\text{C}$ hybrid are almost comparable to that of Pt/C catalyst. Even though the E_{onset} and $E_{1/2}$ values of $\text{Co}_3\text{O}_4\text{-CeO}_2/\text{C}$ hybrid and $\text{Co}_3\text{O}_4/\text{C}$ are identical, yet, the former (-4.20 mA cm^{-2}) is superior to the later (-3.67 mA cm^{-2}) as well as Pt/C (-3.86 mA cm^{-2}) pertaining to the limiting current density (j_m), indicating effective electronic conduction among Co_3O_4 , CeO_2 and the carbon support in case of $\text{Co}_3\text{O}_4\text{-CeO}_2/\text{C}$. The electrochemical parameters of all the ECs were summarized in Table 7.

Table 7. Summary of the electrochemical parameters for ORR of the as-synthesized ECs, VC and Pt/C derived from LSV curves at 1600 rpm.

Catalysts	E_{onset} (V vs. Ag/AgCl)	$E_{1/2}$ (V vs. Ag/AgCl)	j_m (mA cm ⁻²)
CeO ₂ /C	-0.13	-0.31	-3.40
Co ₃ O ₄ /C	-0.12	-0.27	-3.67
Co ₃ O ₄ -CeO ₂ /C hybrid	-0.12	-0.27	-4.20
(Co ₃ O ₄ +CeO ₂) + C	-0.14	-0.32	-4.04
Co ₃ O ₄ -CeO ₂	-0.22	-0.40	-1.26
VC	-0.26	-0.44	-1.96
Pt/C	-0.05	-0.15	-3.86

Figures 22c, 22d, 23a, 23c, 23e, 23g, and 23i shows the corresponding LSV curves of Co₃O₄-CeO₂/C hybrid, Co₃O₄/CeO₂, VC, CeO₂/C, Co₃O₄/C, (Co₃O₄+CeO₂) + C and Pt/C catalyst, respectively. The increase in current density at higher rotating speeds is expected all the ECs. This is due to the fast electron movement and the ease of acceleration of O₂ molecules towards the catalyst surface at elevated rotation speeds. Further, from Figure 22c, d it is clear that the current density immensely increases after addition of the carbon support.

The linear and parallel K-L plots shown in the inset of Figure 22c,d for Co₃O₄-CeO₂/C hybrid and Co₃O₄/CeO₂ ECs implies first order kinetics in regard to the concentration of the dissolved O₂. Similar kinetics were also followed for VC, CeO₂/C, Co₃O₄/C, (Co₃O₄+CeO₂) + C, and Pt/C catalyst as obtained from their respective K-L plots, depicted in Figures 23b, 23d, 23f, 23h, and 23j. The “n” at -0.60 V (Figure 24a) obtained from the slope of K-L plots of Co₃O₄-CeO₂/C hybrid, (Co₃O₄+CeO₂) + C, Co₃O₄/C, CeO₂/C, Co₃O₄/CeO₂, Pt/C and VC is 3.9, 3.1, 3.2, 2.2, 1.5, 3.5 and 3.0, respectively. It implicates that oxygen reduction proceeds via the ideal direct “4e⁻” pathway (O₂ + 2H₂O + 4e⁻ → 4OH⁻) on Co₃O₄-CeO₂/C like that of Pt/C catalyst. Thus, among the synthesized ECs, Co₃O₄-CeO₂/C shows the best ORR activity. The ‘n’ values for (Co₃O₄+CeO₂) + C, Co₃O₄/CeO₂, CeO₂/C, Co₃O₄/C and VC suggest the formation of anionic species favoring indirect “2e⁻” pathway (O₂ + H₂O + 2e⁻ → HO₂⁻ + OH⁻; HO₂⁻ + H₂O + 2e⁻ → 3OH⁻). Co₃O₄-CeO₂/C hybrid maintained ‘n’ values of 3.8 – 4.1 over the potential range of -0.35 to -0.65 V, similar to that of Pt/C catalyst (n = 3.3 – 3.5) in the same potential region (Figure 24b). It is noteworthy to mention that the indirect “2e⁻” pathway has been adopted in the recent years as an efficient and selective way to produce H₂O₂. Nonetheless, direct pathway is more favorable for exclusive ORR studies.

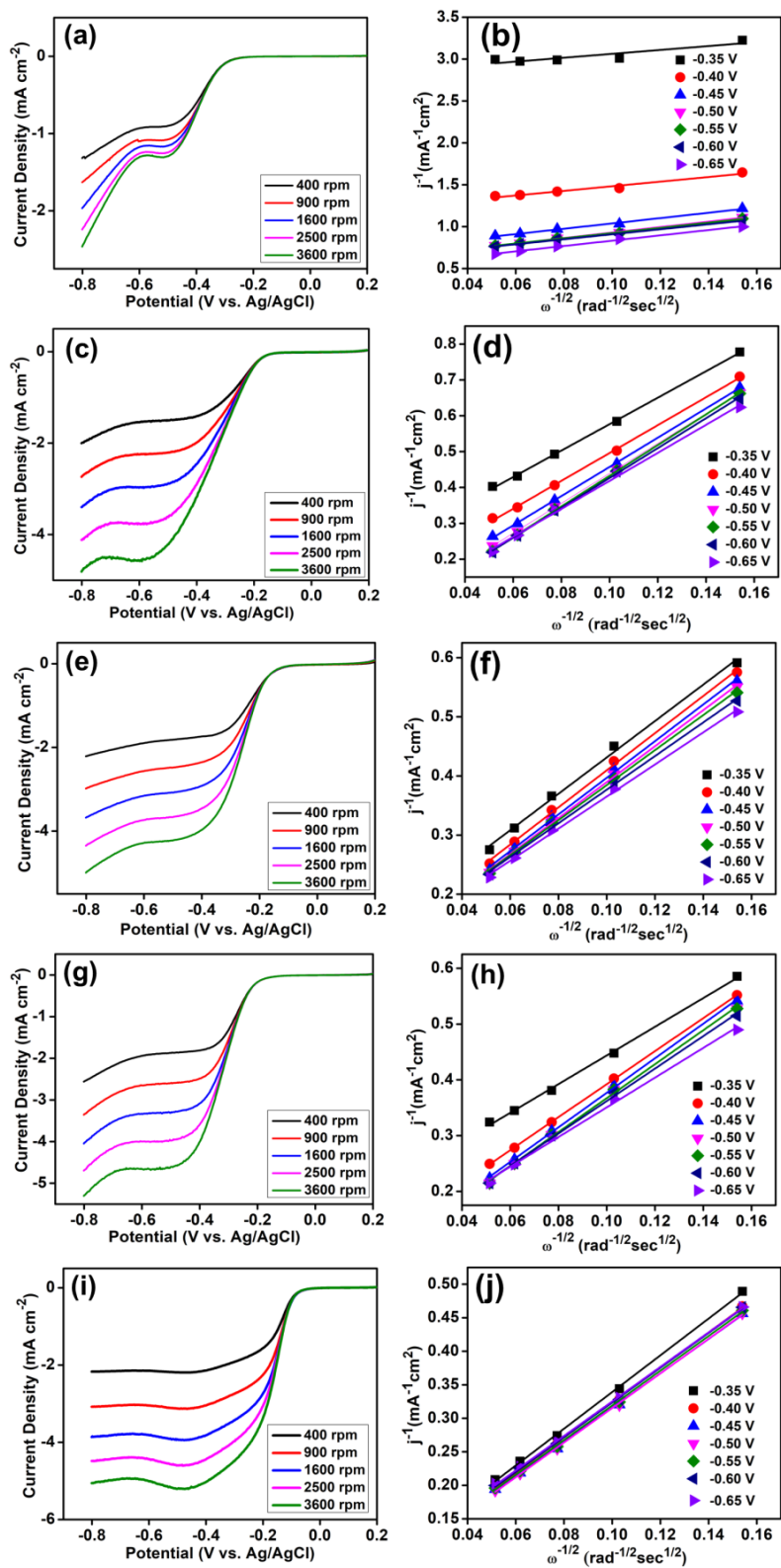


Figure 23. LSVs and K-L plots respectively for (a, b) VC, (c, d) CeO_2/C , (e, f) $\text{Co}_3\text{O}_4/\text{C}$, (g, h) $(\text{Co}_3\text{O}_4+\text{CeO}_2) + \text{C}$ and (i, j) Pt/C in O_2 -saturated 0.1 M KOH.

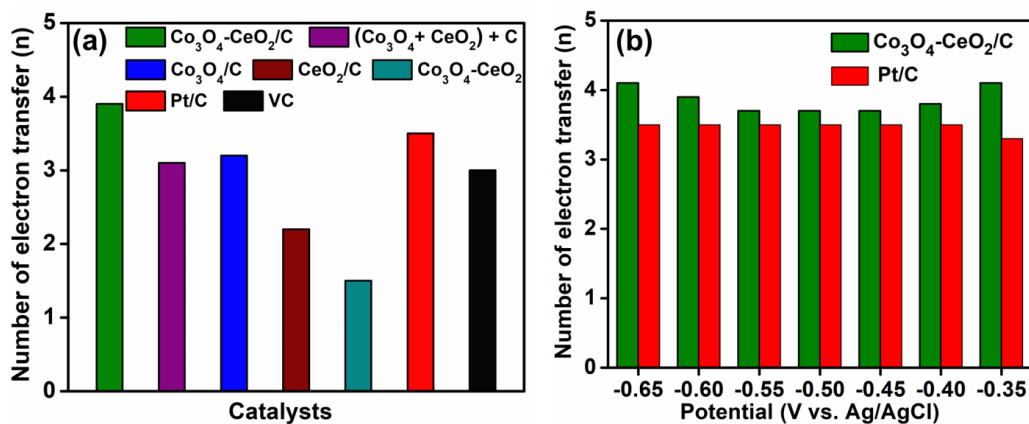


Figure 24. (a) Plot of number of electron transfer (n) at -0.6 V for $\text{Co}_3\text{O}_4\text{-CeO}_2/\text{C}$ hybrid, $(\text{Co}_3\text{O}_4+\text{CeO}_2) + \text{C}$, $\text{Co}_3\text{O}_4/\text{C}$, CeO_2/C , $\text{Co}_3\text{O}_4\text{-CeO}_2$, Pt/C and VC , and (b) number of electrons transfer (n) in potential range from -0.35 to -0.65 V for $\text{Co}_3\text{O}_4\text{-CeO}_2/\text{C}$ hybrid and Pt/C .

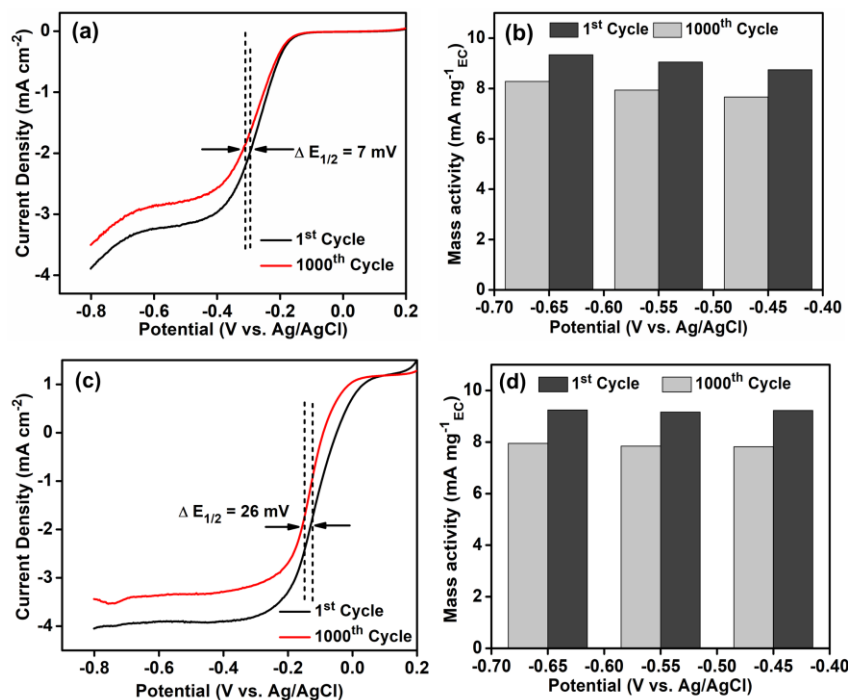


Figure 25. (a) LSV curves and (b) mass activity of $\text{Co}_3\text{O}_4\text{-CeO}_2/\text{C}$ hybrid before and after the ADT.

The evaluation of long-term durability of the $\text{Co}_3\text{O}_4\text{-CeO}_2/\text{C}$ hybrid EC for ORR was done by ADT where the working electrode was cycled between -0.15 to -0.35V in O_2 -saturated 0.1 M KOH solution at 100 mV s^{-1} . The LSV curves in Figure 25a and Figure 25c revealed that the $E_{1/2}$ for $\text{Co}_3\text{O}_4\text{-CeO}_2/\text{C}$ hybrid is shifted nearly by 7 mV after 1000 CV cycles in comparison to a shift of 26 mV for Pt/C catalyst. Moreover, the LSV curves before and after ADT have same E_{onset} values for $\text{Co}_3\text{O}_4\text{-CeO}_2/\text{C}$ hybrid, while about 23 mV shift in E_{onset} is observed for Pt/C catalyst, suggesting better durability of the $\text{Co}_3\text{O}_4\text{-CeO}_2/\text{C}$ hybrid. The agglomeration, dissolution and surface oxidation of Pt/C lead to its degradation in alkaline medium and lower its durability. Figure 25b unveiled that the degradation of mass activity after ADT for $\text{Co}_3\text{O}_4\text{-CeO}_2/\text{C}$ hybrid is 12.3% , 12.2% and 11.3% at -0.45 , -0.55 and -0.65 V , respectively. On the other hand, the degradation of mass activity for Pt/C is around 14.5% in the same potential range (Figure 25d), endorsing the superiority of the $\text{Co}_3\text{O}_4\text{-CeO}_2/\text{C}$ than Pt/C towards ORR.

Figure 26a shows that $\text{Co}_3\text{O}_4\text{-CeO}_2/\text{C}$ hybrid undergoes slow current degradation, retaining up to 81.7% of its initial current at the end of 6 h . Conversely, Pt/C catalyst loses 27.9% of its initial current after 6 h of the test. Thus, the $\text{Co}_3\text{O}_4\text{-CeO}_2/\text{C}$ hybrid can act as a promising EC with long-term stability and durability in practice. The Tafel plots of $\text{Co}_3\text{O}_4\text{-CeO}_2/\text{C}$ hybrid, CeO_2/C , $\text{Co}_3\text{O}_4/\text{C}$ and Pt/C derived from the linear plots of LSV curve at 1600 rpm are represented in Figure 26b. $\text{Co}_3\text{O}_4\text{-CeO}_2/\text{C}$ hybrid (69 mV decade^{-1}) delivers a much lower Tafel slope compared to that of $\text{Co}_3\text{O}_4/\text{C}$ (90 mV decade^{-1}) and CeO_2/C (75 mV decade^{-1}) which suggests a fast charge transfer and improved reaction kinetics of the hybrid due to synergistic effects. However, the proximity in the Tafel slopes of $\text{Co}_3\text{O}_4\text{-CeO}_2/\text{C}$ hybrid (69 mV decade^{-1}) and Pt/C catalyst (68 mV decade^{-1}) is an indication of similar kinetics followed during ORR. The improved ORR activity of the $\text{Co}_3\text{O}_4\text{-CeO}_2/\text{C}$ hybrid compared to all other catalysts can be attributed to the strong oxide/oxide and oxide/carbon hetero-interfaces that possess exceptional properties like fast ionic/electronic conduction and oxygen adsorption paths. Moreover, the synergistic presence of Ce^{3+} and Ce^{4+} ions increases the O_2 adsorption affinity. Thereafter, establishes an easy transport of oxide species which were produced by adsorbed O_2 molecules after accepting electrons, thereafter reaches the active sites (Co^{2+}) of Co_3O_4 where ORR actually occurs.

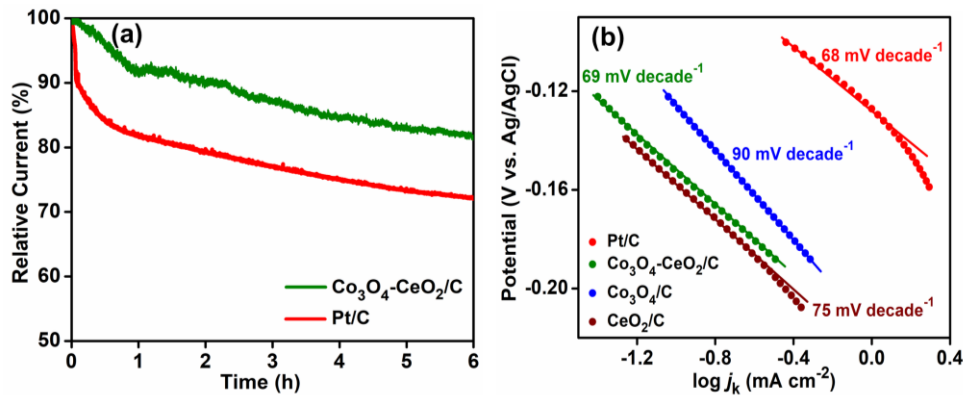


Figure 26. (a) CA responses in O_2 -saturated 0.1 M KOH electrolyte of $Co_3O_4-CeO_2/C$ hybrid and Pt/C at -0.3 V and (b) Tafel plots for $Co_3O_4-CeO_2/C$ hybrid, Co_3O_4/C , CeO_2/C and Pt/C.

The electrochemical OER was evaluated from the LSV at 1600 rpm in 0.1 M KOH solution between 0.2 to 1.5 V as shown in Figure 27a. $Co_3O_4-CeO_2/C$ hybrid EC shows the best OER performance with a maximum current density of 80 mA cm^{-2} at 1.4 V among all the ECs and the standard RuO_2 catalyst. At the same potential CeO_2/C , Co_3O_4/C and RuO_2 catalyst delivers a maximum current density of 4, 50 and 35 mA cm^{-2} , respectively. The E_{onset} for $Co_3O_4-CeO_2/C$ hybrid EC (0.23 V) is smaller compared to that of CeO_2/C (1.27 V), Co_3O_4/C (0.25 V) and RuO_2 catalyst (0.45 V) which is an implication of OER at a lower activation energy in case of the hybrid EC. An effective OER catalyst must possess a lower η_{10} value. The LSV plots and inset image in Figure 6a revealed that $Co_3O_4-CeO_2/C$ hybrid has the lowest $E(j_{10})$ (0.76 V) as well as η_{10} (520 mV) values among all the ECs which clearly explain its superiority towards OER.

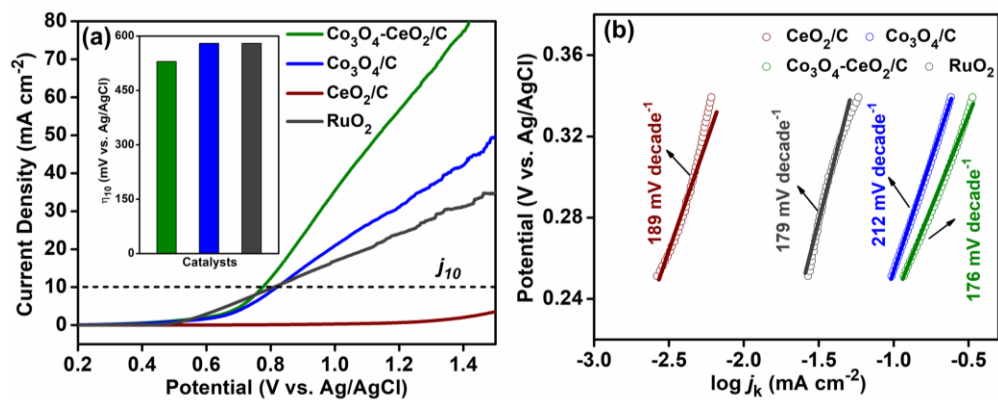


Figure 27. (a) LSV curves in the potential range 0.2 to 1.5 V at 1600 rpm and (b) Tafel plots of CeO_2/C , Co_3O_4/C , $Co_3O_4-CeO_2/C$ and RuO_2 for OER [Inset (a): comparison of overpotential at j_{10}].

Table 8. Summary of onset potential (E_{onset}), overpotential at 10 mA cm^{-2} (η_{10}) and Tafel slopes of CeO_2/C , $\text{Co}_3\text{O}_4/\text{C}$, $\text{Co}_3\text{O}_4\text{-CeO}_2/\text{C}$ hybrid and RuO_2 for OER.

Electrocatalysts	E_{onset} (V vs. Ag/AgCl)	$E_{j_{10}}$ (V vs. Ag/AgCl)	η_{10} (mV vs. Ag/AgCl)	Tafel slope (mV decade ⁻¹)
CeO_2/C	0.81	–	–	189
$\text{Co}_3\text{O}_4/\text{C}$	0.25	0.82	580	212
$\text{Co}_3\text{O}_4\text{-CeO}_2/\text{C}$	0.23	0.76	520	176
RuO_2	0.45	0.81	570	179

All the electrochemical parameters related to OER were summarized in Table 8. The Tafel plots in Figure 27b revealed a smaller Tafel slope for $\text{Co}_3\text{O}_4\text{-CeO}_2/\text{C}$ hybrid (176 mV decade⁻¹) compared to CeO_2/C (189 mV decade⁻¹), $\text{Co}_3\text{O}_4/\text{C}$ (212 mV decade⁻¹), and RuO_2 (179 mV decade⁻¹) in the same potential window, ensuring more favorable OER kinetics of the $\text{Co}_3\text{O}_4\text{-CeO}_2/\text{C}$ hybrid. The durability of the $\text{Co}_3\text{O}_4\text{-CeO}_2/\text{C}$ hybrid towards OER was attained via recording the LSV after 1000 potential cycles under alkaline conditions (Figure 28). A current density difference of 11.5 mA cm^{-2} is observed at 1.4 V in the LSV plot obtained after 1000 cycles, which is moderately acceptable. Interestingly, there is negligible change in the E_{onset} and $E(j_{10})$ values, implying high stability of the hybrid in alkaline medium. From the electrochemical parameters of OER, it can be inferred that the combination of CeO_2 and Co_3O_4 in the hybrid synergistically enhances the electronic interaction and charge transfer process across the oxide-oxide/carbon interfaces resulting in improved kinetics. The enhanced OER activity of the $\text{Co}_3\text{O}_4\text{-CeO}_2/\text{C}$ hybrid can also be attributed to the abundant oxygen vacancies and the mesoporous nature of the hybrid that allows easy release of oxygen from its pores during OER. The Ce^{3+} ions on the surface of the hybrid EC generates highly oxidative species ($\text{O}_2^{2-}/\text{O}_2^-$) which is easily drifted to the active sites of Co_3O_4 from the CeO_2 surface by spillover effect. This in turn accelerates the OER.

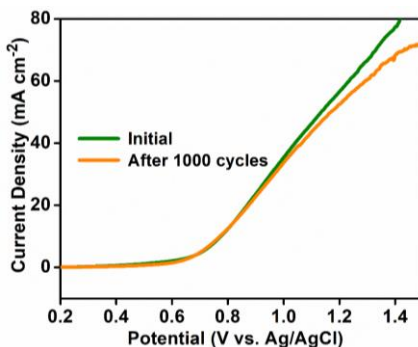


Figure 28. LSV curves of the $\text{Co}_3\text{O}_4\text{-CeO}_2/\text{C}$ hybrid after 1000 CV cycles at 1600 rpm for OER.

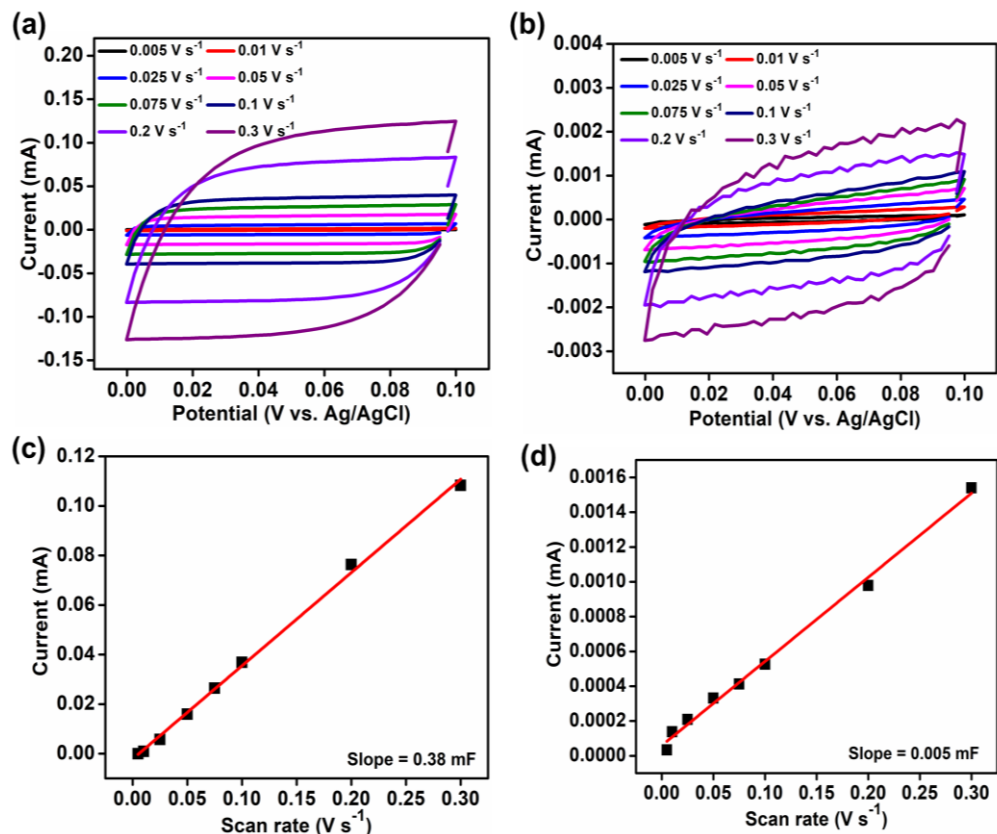


Figure 29. (a, b) Scan rate dependent CVs in a non-Faradaic region and (c, d) the anodic charging current measured as a function of scan rate, for Co₃O₄-CeO₂/C hybrid and Co₃O₄-CeO₂ in N₂-saturated 0.1 M KOH, respectively.

Figures 29 and 30 show the double-layer capacitance (C_{DL}) measurement of the ECs in N₂ saturated 0.1 M KOH electrolyte to determine the ECSA. Figure 29a and Figure 29b represents the scan rate dependent CVs measured in the non-Faradaic region for Co₃O₄-CeO₂/C hybrid and Co₃O₄-CeO₂, respectively. The C_{DL} obtained from the slope of the plot of anodic charging current vs. scan rate for Co₃O₄-CeO₂/C hybrid (Figure 29c), Co₃O₄-CeO₂ (Figure 29d), CeO₂/C (Figure 30b), Co₃O₄/C (Figure 30d), and (Co₃O₄+CeO₂) + C (Figure 30f) are 0.38, 0.22, 0.34, 0.076, and 0.005 mF, respectively. The corresponding ECSA for CeO₂/C, Co₃O₄/C, Co₃O₄-CeO₂/C hybrid, and Co₃O₄/CeO₂ are 18.3, 34, 37, 7.6 and 0.63 m² g⁻¹, respectively, indicating the presence of more electrochemically active sites in the Co₃O₄-CeO₂/C hybrid. The highest ECSA of the Co₃O₄-CeO₂/C hybrid can be ascribed to the proper synergistic effect between the corresponding mono-MOs and the carbon support in the hybrid.

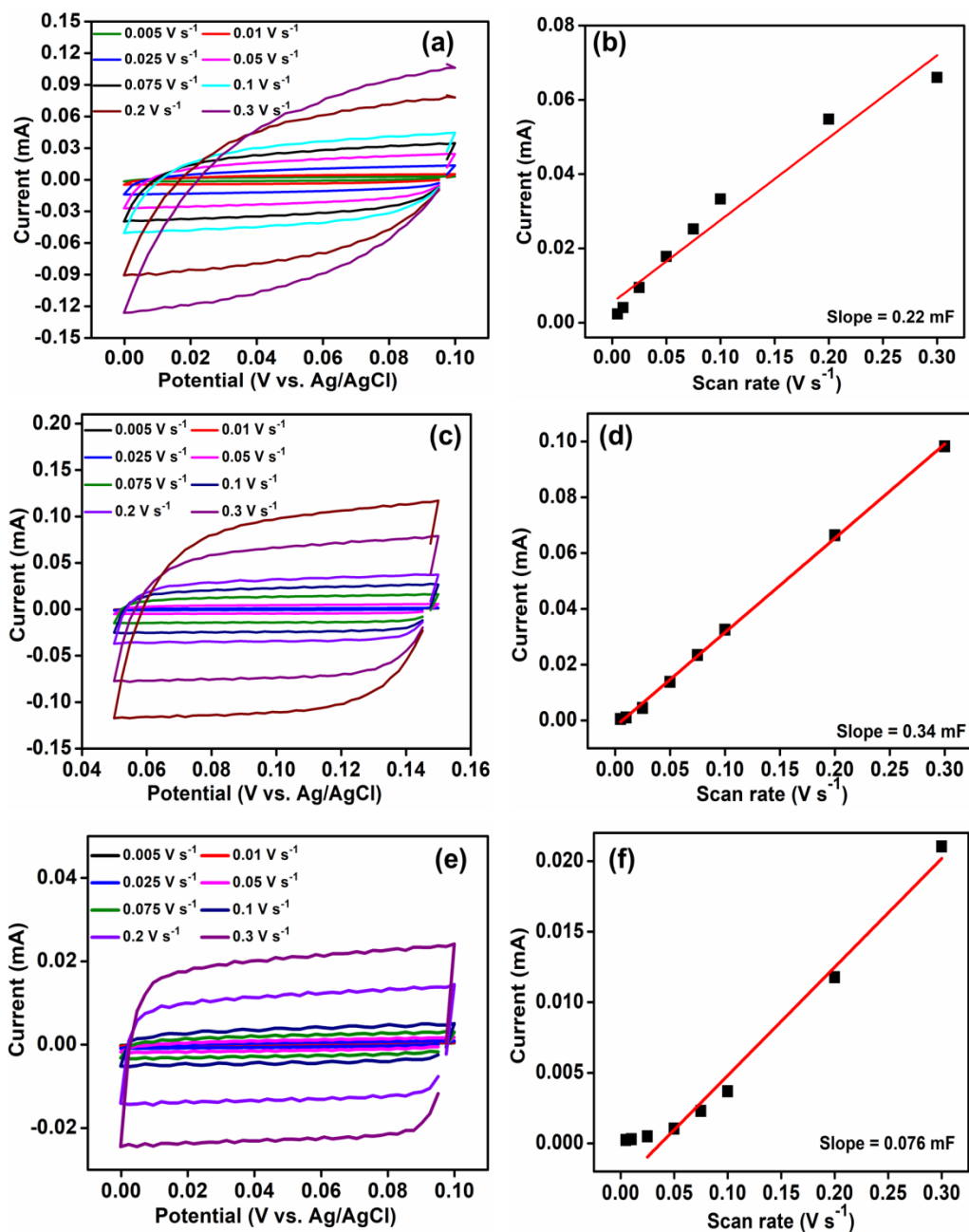


Figure 30. Scan rate dependent CVs in a non-Faradaic region and the anodic charging current measured as a function of scan rate for (a, b) CeO₂/C, (c, d) Co₃O₄/C and (e, f) (Co₃O₄+CeO₂) + C in N₂-saturated 0.1 M KOH.

Characterizations of the carbon-supported Pd–Cu alloy NPs

XRD analysis: Figure 31a shows the p-XRD profile of the as-synthesized PdCu₃/C, PdCu/C, Pd₃Cu/C and Pd/C NPs. The p-XRD profile shows that the PdCu NPs are well crystallized as observed from the four distinct diffraction peaks. A broad characteristic diffraction peak of

carbon (JCPDS No. 75-1621) from (002) crystalline plane at $2\theta = 24.8^\circ$ can be observed for all the three composition of carbon-supported Pd–Cu NPs. The three main diffraction peaks at $2\theta = \sim 39.9^\circ$, $\sim 46.7^\circ$ and $\sim 68.2^\circ$ were indexed to the (111), (200) and (220) crystal planes of *fcc* Pd NPs, respectively, according to JCPDS No. 88-2335.

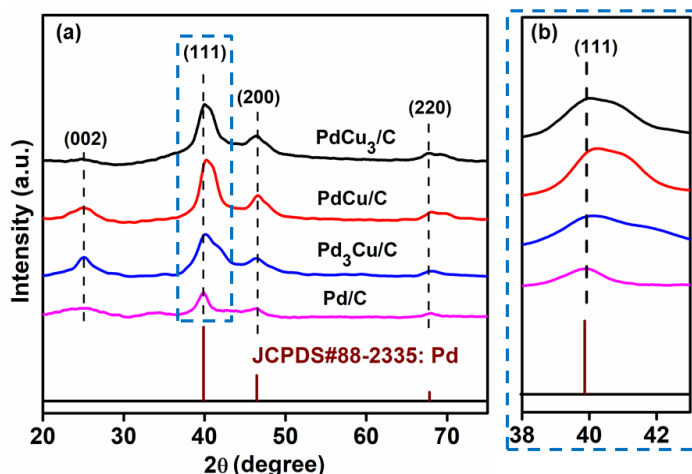


Figure 31. (a) p-XRD patterns and (b) magnified view of the Pd (111) diffraction peak of PdCu₃/C, PdCu/C, Pd₃Cu/C and Pd/C NPs.

After Cu incorporation, the diffraction peak at 39.9° corresponding to the (111) plane is slightly shifted to the higher angles, indicating the formation of Pd–Cu alloy NPs. The shift of Pd (111) peak is shown as a magnified view in Figure 31b. This shift might be due to the Pd lattice contraction owing to the smaller radius of Cu (0.128 nm) as compared to that of Pd (0.137 nm).

EDX analysis: The presence of C, Cu and Pd in the Pd₃Cu/C NPs were confirmed by EDX analysis. Figure 32a,b represents the electron image and the EDX spectra of Pd₃Cu/C NPs, respectively. The table in the inset of Figure 32b confirmed the atomic percentages of Pd (2.05%) and Cu (0.90%) in Pd₃Cu/C which is in consistent with the theoretically determined values. The EDX elemental maps for individual C, Cu and Pd shown in Figure 32c-e represent the spatial dissemination of the elements. Notably, the absence of other elements in the EDX pattern confirms the purity of the material.

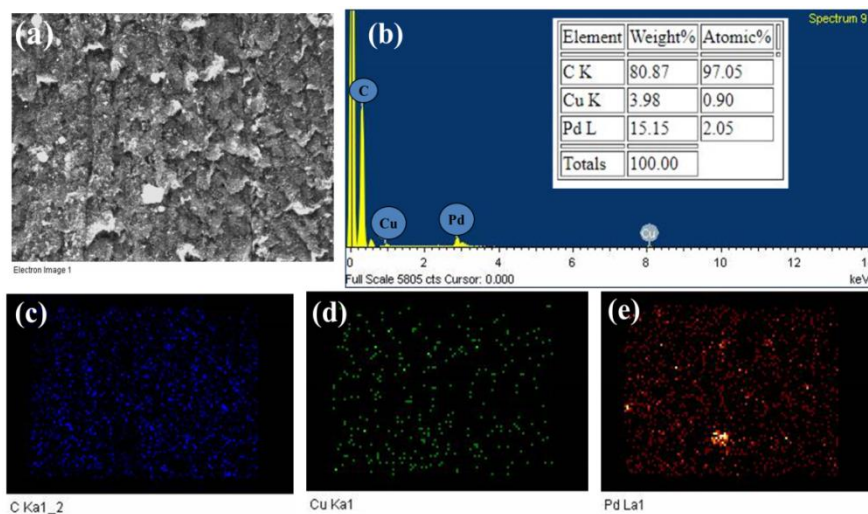


Figure 32. EDX spectra of Pd₃Cu/C alloy NPs (a) the electron image (b) the EDX pattern and (c)-(e) elemental maps for individual C, Cu and Pd, respectively.

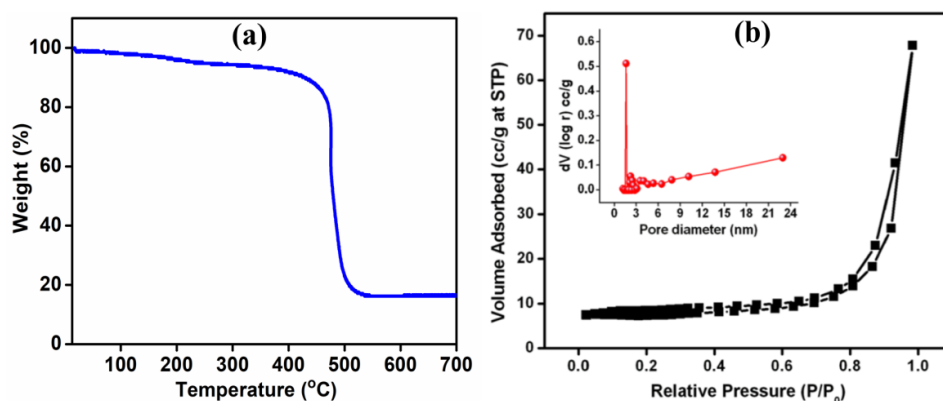


Figure 33. (a) TGA profile and (b) N₂ adsorption/desorption isotherm and the pore size distribution curve (inset) of Pd₃Cu/C alloy NPs.

TGA analysis: Figure 33a shows the TGA profile of Pd₃Cu/C. A distinct weight loss at ~350 °C is due to the conversion of carbon to CO₂ in an oxidative environment. After 500 °C, decomposition of carbon from Pd₃Cu/C is negligible and reaches a stable weight % (~19%), which confirms that the total metal loading on the carbon support is 20%.

BET surface area analysis: The N₂ adsorption/desorption isotherms of Pd₃Cu/C alloy NPs is represented in Figure 33b. A type IV isotherm and H3 hysteresis loop are observed from the isotherm pattern. The specific surface area determined using BET method is found to be 30.1 m²g⁻¹. Inset of Figure 33b shows the pore size distribution curve of Pd₃Cu/C. The average pore

diameter obtained using BJH measurement is found to be 3.2 nm which suggests that the particles mesoporous in nature.

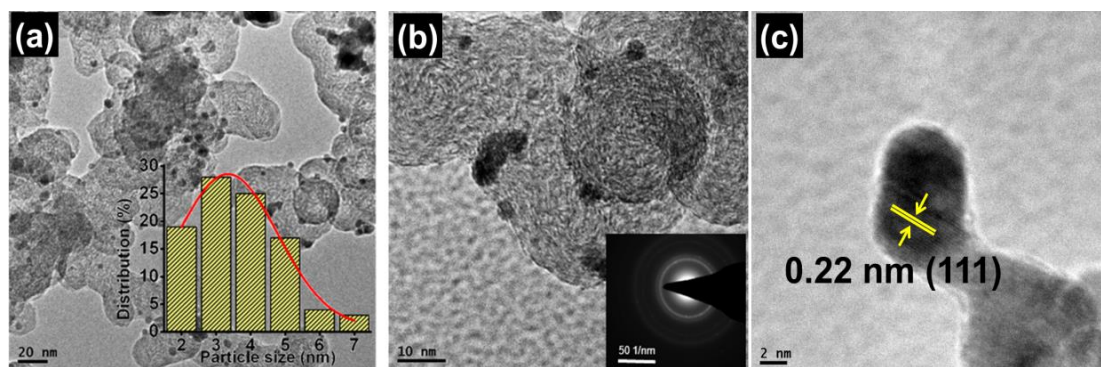


Figure 34. (a,b) TEM images at two different resolutions; the particle size distribution (inset image a), SAED pattern (inset image b) and (c) HRTEM image for Pd₃Cu/C alloy NPs.

TEM analysis: The morphology and size of the Pd₃Cu/C alloy NPs were determined by TEM and HRTEM analysis. Figure 34a,b exhibit the TEM images of Pd₃Cu/C alloy NPs at two different resolutions which clearly demonstrates the spherical morphology of the metallic counterparts. The spherical metals are homogeneously dispersed over the carbon matrix with less aggregation which confirms high stability of the NPs. The corresponding size and the distribution of the NPs were determined and found that most of the particles fall in the range of 3–5 nm with an average size of about 3 nm. Moreover, the SAED pattern represents well defined concentric rings which signify the polycrystallinity of the sample. The HRTEM image in Figure 34c indicate clear lattices fringes with a *d*-spacing of 0.22 nm corresponding to the (111) facet of Pd NPs, which corroborates well with the p-XRD results.

Figure 35a represents the survey spectrum which confirms the presence of all the elements in Pd₃Cu/C. Figure 35b shows the high resolution C 1s XP spectrum which is deconvoluted into four different components at the BEs of 284.9, 285.4, 286.6 and 289.3 eV, corresponding to C–C (sp³), C=C (sp²), C–O and O=C–H species, respectively. The peak intensity of C–C bond is quite strong which signify the presence of more sp³-hybridized carbon in the synthesized NPs. Figure 35c displays the high resolution Cu 2p core-level XP spectrum. In the Cu 2p spectrum, two major peaks located at the BE of 932.3 and 952.1 eV indicates the presence of zero-valent Cu in the alloy. However, the deconvoluted spectrum shows two more additional peaks which are due to the presence of Cu²⁺ species. Figure 35d illustrates the comparison of BEs obtained from XP spectra of Pd 3d in Pd₃Cu/C and Pd/C NPs. The Pd 3d region shows predominantly two major peaks at BEs of 335.4 and 340.7 eV which are assigned

respectively to the low energy band (Pd 3d_{5/2}) and high-energy band (Pd 3d_{3/2}). Additionally, two broad peaks were observed after deconvolution at around 336.9 and 340.6 eV corresponding to PdO species. However, Pd is present mostly in the zero-valent state as the intensity of the peak at 335.2 eV is much higher than that of the other. Compared to the BEs of Pd/C NPs (335.2 eV for Pd 3d_{5/2} and 340.4 eV for Pd 3d_{3/2}), BEs of Pd 3d_{5/2} and Pd 3d_{3/2} in Pd₃Cu/C NPs show a clear positive shift of ~0.2 and ~0.3 eV, respectively. The upshift in BE may be explained on the basis of lattice contraction of Pd caused by insertion of Cu into it and the electronic modification in Pd₃Cu/C due to partial electron transfer to Pd from Cu.

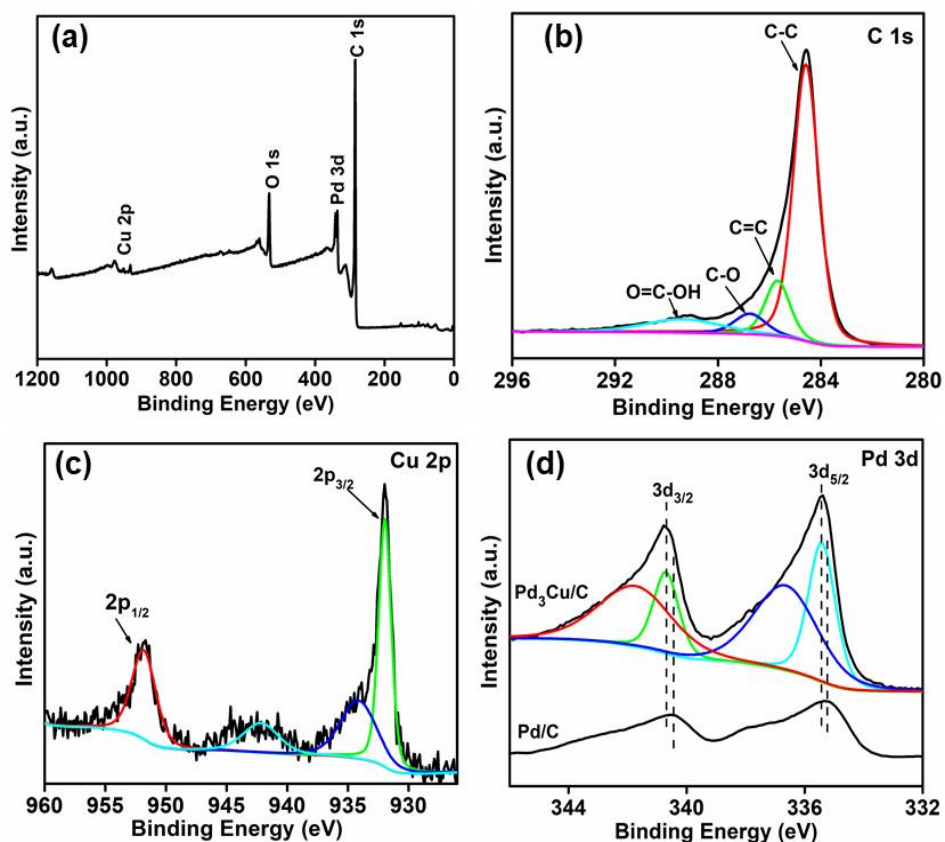


Figure 35. (a) The survey spectrum, the high resolution XP spectra of (b) C 1s and (c) Cu 2p in Pd₃Cu/C NPs and (d) Pd 3d region in Pd₃Cu/C and Pd/C NPs.

Characterizations of the carbon-supported Pd–Ni alloy NPs

XRD analysis: The representative p-XRD patterns of the as-synthesized PdNi₃/C, PdNi/C, Pd₃Ni/C and Pd/C ECs are shown in Figure 36a. The broad diffraction peak located at 2θ = 24.8° corresponds to (002) crystalline plane of carbon according to the JCPDS No. 75-1621.

The other three diffraction peaks located at 2θ values of ~ 39.9 , ~ 46.7 , and $\sim 68.2^\circ$ could be indexed to the (111), (200) and (220) crystal planes of *fcc* type of Pd NPs (JCPDS No. 88-2335), respectively. A broad and low intensity diffraction peak at about $2\theta = 44.4^\circ$ appeared in case of PdNi₃/C corresponds to the (111) crystalline plane of *fcc* lattice of cubic Ni NPs according to the JCPDS No. 87-0712, which might be due to increase in the Ni content. A slight shift in the diffraction peak to higher angles corresponding to Pd (111) plane was observed, as shown in Figure 36b, due to incorporation of Ni with smaller atomic radius into the Pd lattice of comparatively larger size, suggesting the formation of Pd–Ni alloys.

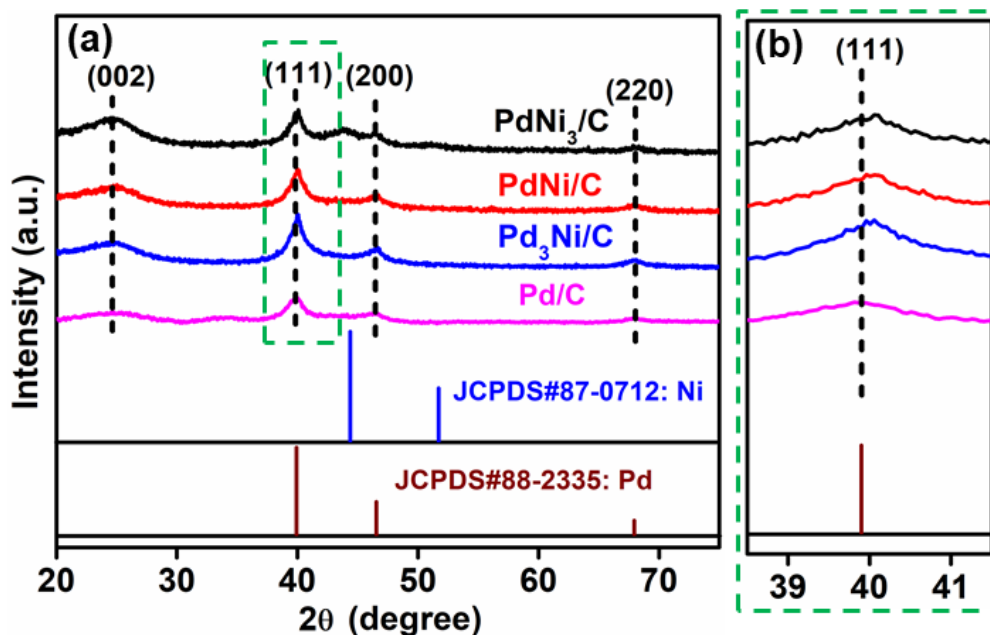


Figure 36. (a) p-XRD patterns and (b) magnified view of the typical (111) diffraction peak of PdNi₃/C, PdNi/C, Pd₃Ni/C and Pd/C.

EDX analysis: To determine the elements present in the Pd₃Ni/C EC, EDX analysis was carried out. Figure 37 shows the EDX pattern of Pd₃Ni/C along with the EDX based elemental maps for individual C, Pd and Ni. The presence of only detectable elements *i.e.*, Pd, Ni and C in Pd₃Ni/C signify high purity of the sample. The table in the inset of Figure 37b confirmed that the atomic percentages of Pd (0.78%) and Ni (0.28%) in Pd₃Ni/C corroborates well with the theoretically determined ratio of 3:1 for Pd:Ni.

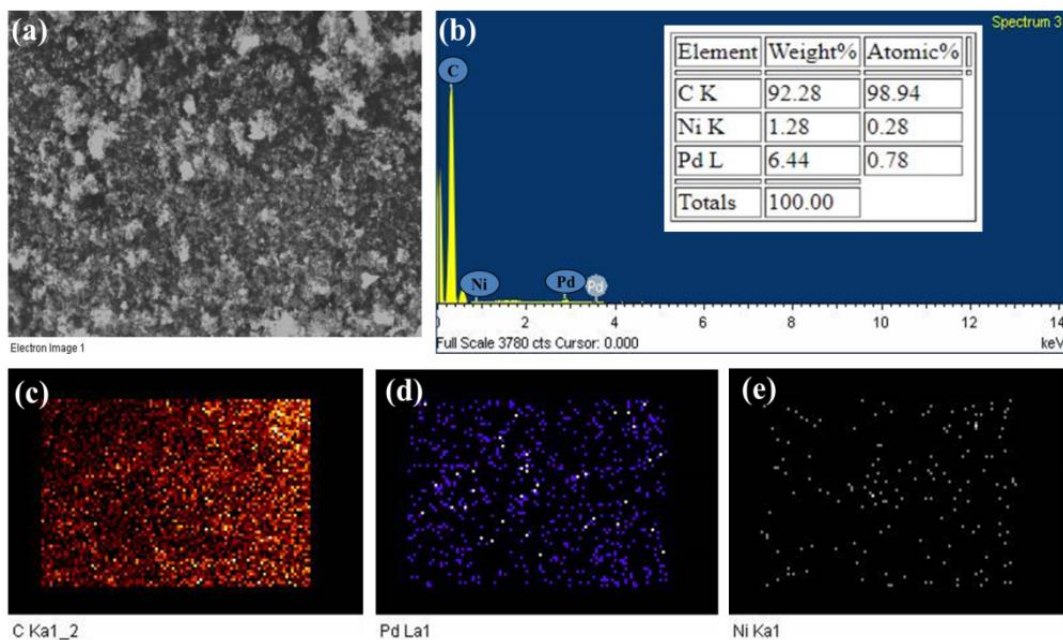


Figure 37. EDX spectra of Pd₃Ni/C; (a) the electron image (b) the EDX pattern and (c)-(e) elemental maps for individual C, Pd and Ni, respectively.

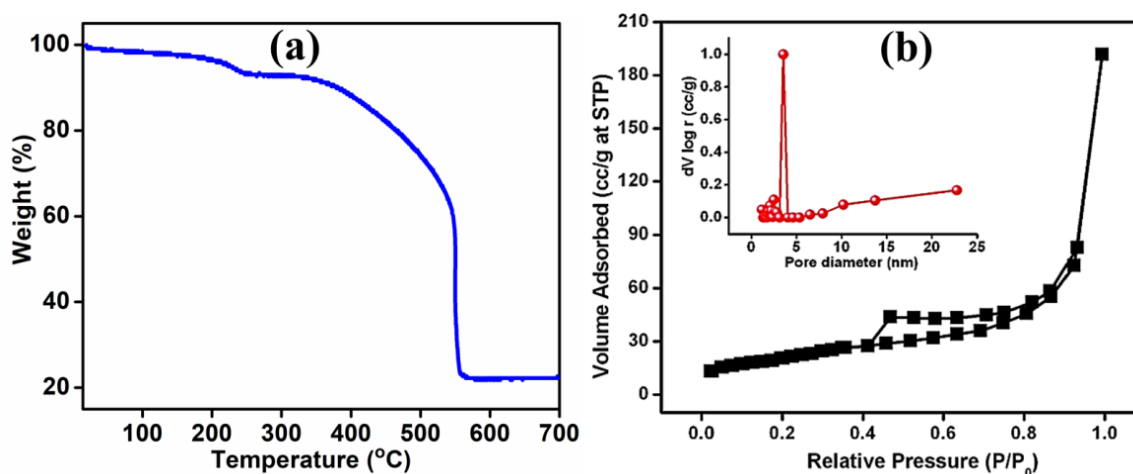


Figure 38. (a) TGA profile and (b) N₂ adsorption/desorption isotherm and the pore size distribution curve (inset) of Pd₃Ni/C alloy NPs.

TGA analysis: The TGA profile of Pd₃Ni/C EC shows a sudden weight loss at about 350 °C, which is due to the oxidation of carbon to CO₂ as shown in Figure 38a. However, the decomposition of carbon from Pd₃Ni/C is negligible after 500 °C and reaches a stable weight of ~21.9%, confirming that the total metal loading on the carbon support is nearly 20 wt%.

BET surface area analysis: Figure 38b shows the N₂ adsorption/desorption isotherm performed at -196 °C and pore size distribution (inset) for Pd₃Ni/C EC. It exhibits type IV isotherm with H3 hysteresis loop, indicating the presence of slit-shaped pores. The BET surface area was found to be 21.6 m²g⁻¹. The average pore diameter calculated by BJH method was found to be 2.9 nm. The pore diameter range suggests that the particles are mesoporous in nature.

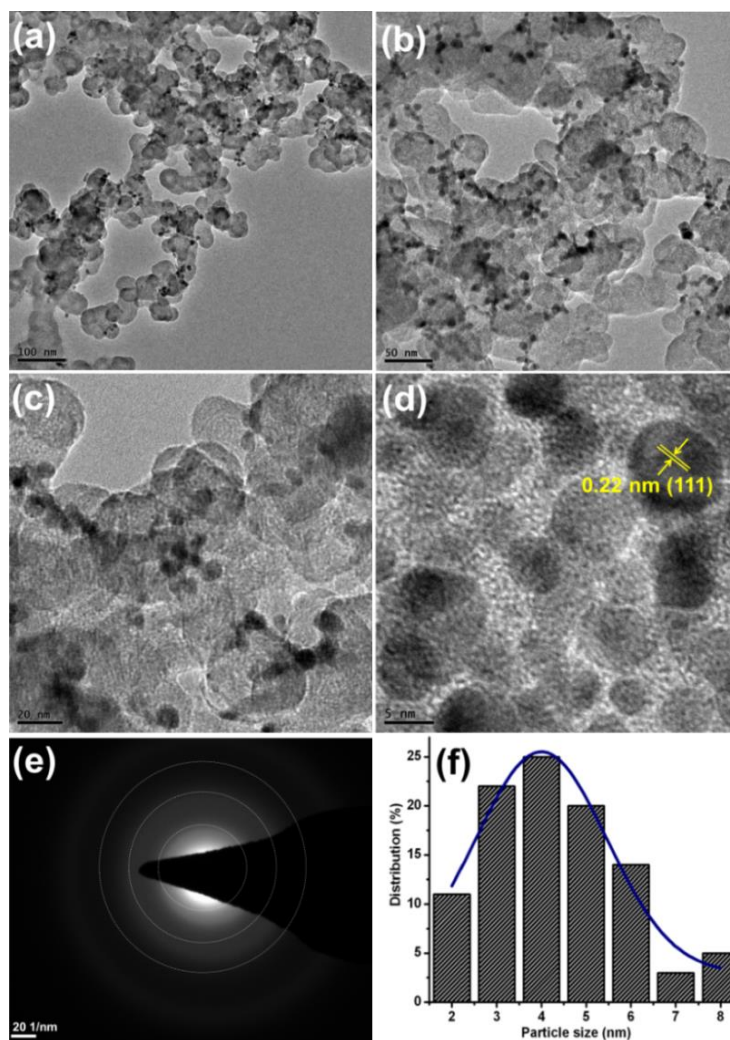


Figure 39. (a,b) Low magnification TEM images, (c,d) HRTEM images, (e) the SAED pattern and (f) corresponding particle size distribution for Pd₃Ni/C.

TEM analysis: The morphology of the Pd₃Ni/C was characterized by TEM and HRTEM analysis. The representative low magnification TEM images of Pd₃Ni/C are shown in Figure 39a,b. Smaller sized metallic particles with sphere-like shapes are homogeneously distributed on the carbon support as seen from the HRTEM image (Figure 39c). The HRTEM image in Figure 39d shows clear lattice fringes with a *d*-spacing of ~0.22 nm that is ascribed to Pd (111)

plane. Figure 39e shows the SAED pattern, which represents well-defined concentric rings. From this observation, the polycrystallinity of the synthesized EC is established. Moreover, the size and the distribution of the particles were also determined by using ImageJ software and plotted in a histogram as shown in Figure 39f. Most of the metallic particles are less than 8 nm with an average size of 4.2 nm.

XPS analysis: The survey spectrum in Figure 40a confirmed the presence of Pd, Ni and C in Pd₃Ni/C. Figure 40b shows the high resolution C 1s XP spectrum with four different components. The most intense peak at BE of 284.6 eV corresponds to sp³ hybridized C–C species. Other three peaks at the BEs of 285.4, 286.6 and 289.3 eV are assigned to C=C (sp²), C–O and O=C–OH species, respectively. Figure 40c shows the core-level XP spectrum of Ni 2p. Two major peaks at BEs of 856.4 and 873.4 eV were found, which correspond to Ni 2p_{3/2} and Ni 2p_{1/2}, respectively. In addition, two more satellite peaks at the BEs of 861.2 and 879.9 eV are observed, which are basically due to the presence of Ni²⁺ species in the Pd₃Ni/C.

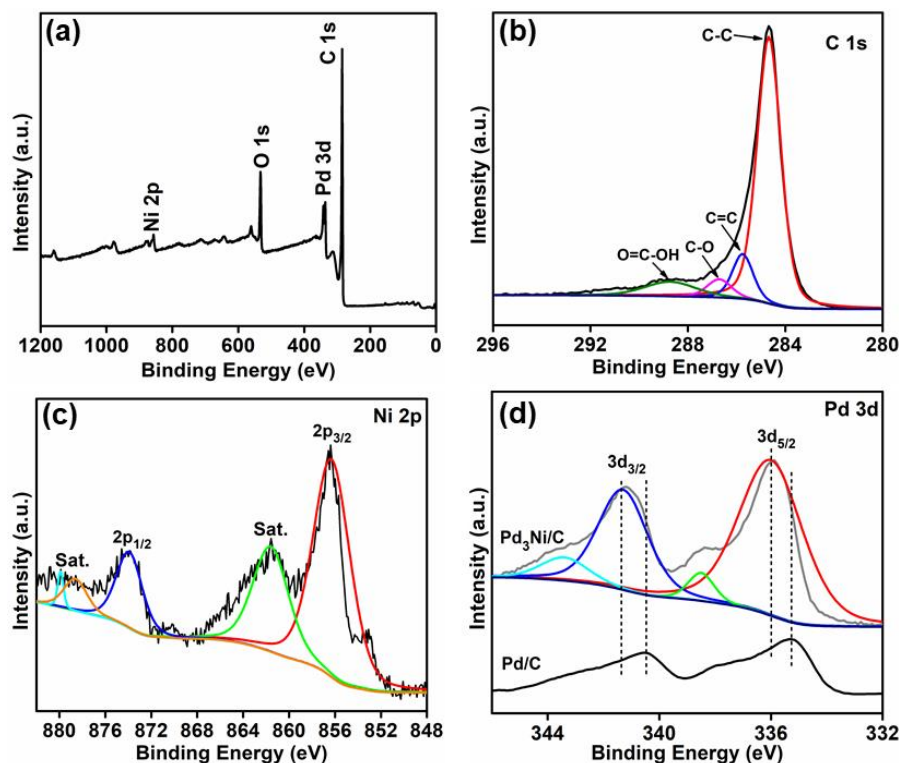


Figure 40. XP spectra of Pd₃Ni/C and Pd/C; (a) the survey spectrum and the high resolution XP spectra of (b) C 1s and (c) Ni 2p in Pd₃Ni/C and (d) Pd 3d region in Pd₃Ni/C and Pd/C.

The core-level Pd 3d XP spectra of Pd₃Ni/C and Pd/C ECs are shown in Figure 40d. The two major peaks at the BEs of 335.9 and 341.3 eV for Pd₃Ni/C can be assigned to Pd 3d_{5/2} (low energy band) and Pd 3d_{3/2} (high energy band) spin-orbit states, respectively. This indicates that Pd species are mostly in metallic state (Pd⁰). In addition, two minor peaks were observed at 338.5 and 343.4 eV correspond to Pd²⁺ 3d_{5/2} and Pd²⁺ 3d_{3/2}, respectively, indicating the presence of surface PdO species. It is observed that the BEs of Pd 3d_{5/2} and 3d_{3/2} in Pd₃Ni/C, respectively, shows a positive shift of nearly 0.7 and 0.9 eV than that of BEs of Pd 3d_{5/2} (335.2 eV) and 3d_{3/2} (340.4 eV) in Pd/C.

Characterizations of the Pd₃M/C–CeO₂ (M = Ni and Cu) NPs

XRD analysis: Figure 41a compares the XRD patterns of C–CeO₂, Pd/C–CeO₂, Pd₃Ni/C–CeO₂, PdNi/C–CeO₂ and PdNi₃/C–CeO₂. All the Pd-based samples exhibited typical peaks (denoted by ‘#’) characteristic of *fcc* Pd NPs. These peaks are in consistent with JCPDS No. 88-2335. Further, the diffraction peaks denoted by ‘*’ in all the three compositions of Pd–Ni including C–CeO₂ corresponds to different planes of *fcc* CeO₂ (JCPDS No. 34-0394). Generally, a broad peak is observed at 2θ = ~24° due to the presence of carbon (JCPDS No. 75-1621). However, this peak is very faint due to overlapping of highly crystalline CeO₂ phases. Similarly, Figure 41b represent the p-XRD patterns of C–CeO₂ supported Pd–Cu alloy NPs. All the peaks related to *fcc* Pd NPs and *fcc* CeO₂ can be observed, implying the co-existence of Pd and CeO₂ in the materials.

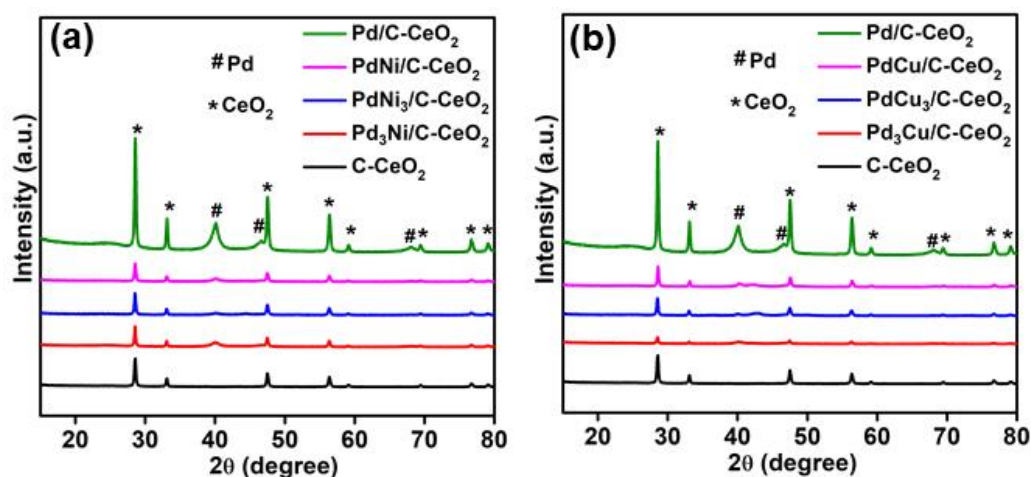


Figure 41. p-XRD profile of C–CeO₂, Pd/C–CeO₂, Pd₃M/C–CeO₂, PdM/C–CeO₂ and Pd₃M/C–CeO₂, (a) M = Ni and (b) M = Cu.

EDX analysis: The presence of elements and their atomic percentages in Pd₃M/C–CeO₂ (M = Ni and Cu) ECs were confirmed by EDX analysis. Figure 42 shows the EDX pattern of Pd₃Cu/C–CeO₂ along with the EDX elemental maps for individual C, O, Cu, Pd and Ce, signifying high purity of the sample. The table in the inset of Figure 42b confirmed that the atomic percentages of Pd (4.99%) and Cu (1.83%) in Pd₃Cu/C–CeO₂ agreed well with the targeted ratio for Pd and Cu *i.e.*, 3:1. Similarly, Figure 43 represents the EDX patterns and elemental maps of Pd₃Ni/C–CeO₂ which confirmed the presence of only detectable elements in the respective samples. The atomic percentages of Pd (2.16%) and Ni (0.64%) is in 3:1 ratio.

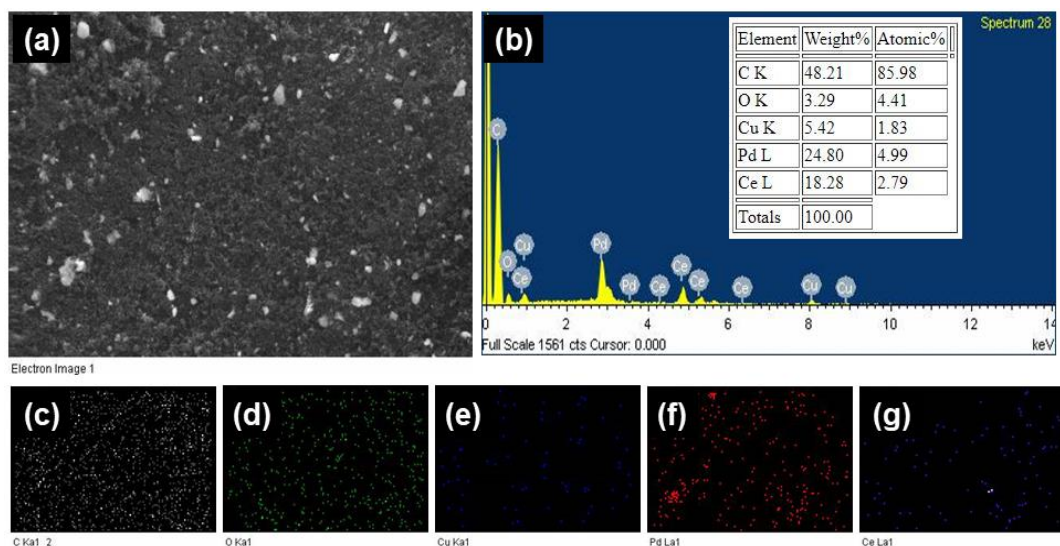


Figure 42. EDX analysis of Pd₃Cu/C–CeO₂; (a) electron image (b) EDX pattern and (c)-(g) elemental maps for individual C, O, Cu, Pd and Ce, respectively.

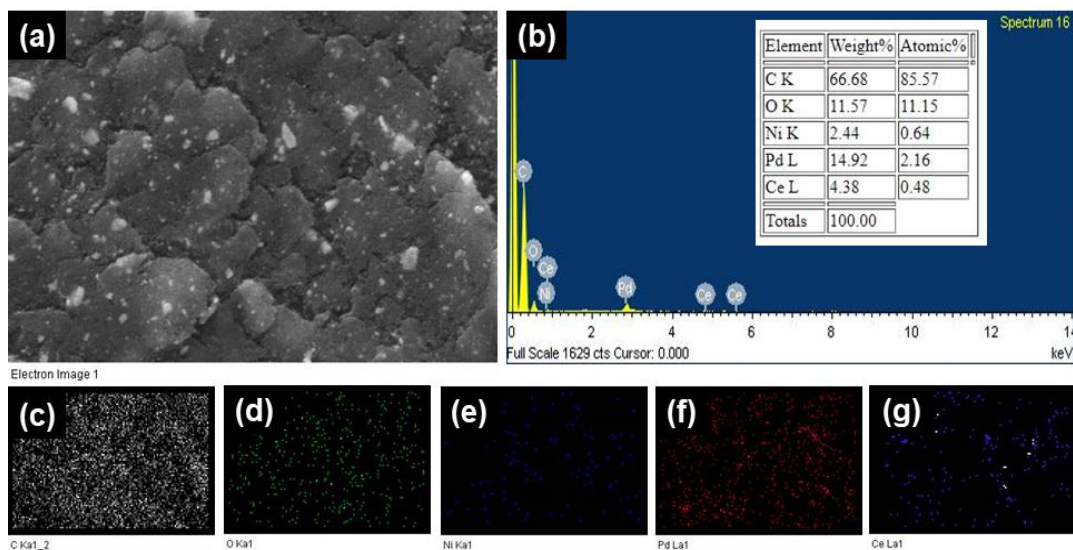


Figure 43: EDX analysis of Pd₃Ni/C–CeO₂; (a) electron image (b) EDX pattern and (c)-(g) elemental maps for individual C, O, Ni, Pd and Ce, respectively.

TEM analysis: The low magnification TEM images of Pd₃Ni/C–CeO₂ are represented in Figure 44a,b. The small and spherical dark contrasts are the metallic counterparts, while the bigger and comparatively less dark contrasts are the CeO₂ particles. A homogeneous distribution of the metallic particles over the entire support can be encountered. The metallic particles have an average diameter of 2.15 nm as determined from the particle size distribution curve (Inset Figure 44b). The SAED pattern confirmed different planes associated with CeO₂ and Pd lattices, as depicted in Figure 44c. Figure 44d-f depicts the HRTEM images of Pd₃Ni/C–CeO₂ NPs. A *d*-spacing of 0.13 nm was obtained from the HRTEM images (Figure 44d,f), corresponding to Pd (220) plane. A *d* value equal to 0.27 nm is ascribed to (200) plane of CeO₂ (Figure 44e).

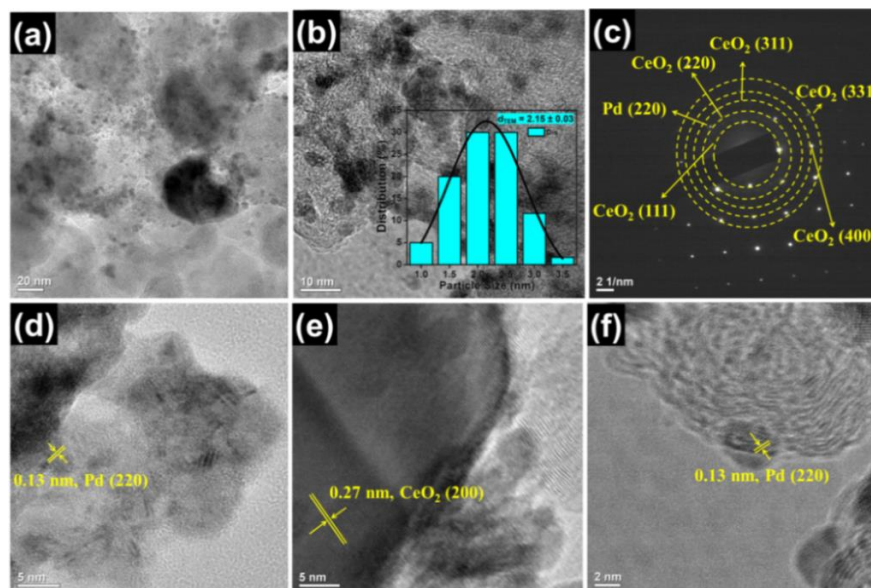


Figure 44. (a,b) Low magnification TEM images (inset b: particle size distribution plot), (c) the SAED pattern and (d)-(f) HRTEM images of Pd₃Ni/C–CeO₂.

Figure 45a represents the low magnification TEM micrographs of Pd₃Cu/C–CeO₂. The micrographs clearly show the homogeneous dispersion of the metallic particles over the support. Like earlier, all the metallic particles were found to have spherical morphology. Inset in Figure 45a is the histogram showing particle size distribution. All the metallic counterparts fall in the range of 1–6 nm, with a mean diameter of about 2.8 nm. In Figure 45b, the relatively dark contrasts of bigger size can be ascribed to CeO₂, on which smaller metallic particles were

seen to be embedded. The SAED pattern (Figure 45c) corresponds to various planes of CeO₂ and (111) plane of Pd, confirming the formation of Pd₃Cu/C–CeO₂. The HRTEM images shown in Figure 45d,e displayed clear lattice fringes with *d*-spacings of 0.22 nm and 0.27 nm attributable to Pd (111) and CeO₂ (200) facets, respectively.

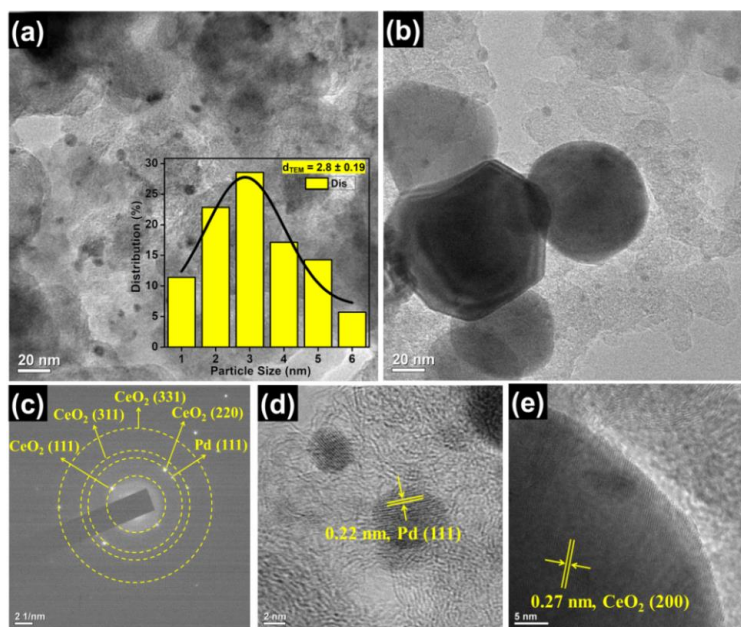


Figure 45. (a,b) Low magnification TEM images (inset a: particle size distribution plot), (c) the SAED pattern and (d,e) HRTEM images of Pd₃Cu/C–CeO₂.

XPS analysis: The survey spectrum of Pd₃Ni/C–CeO₂ showed characteristic signatures of C, O, Ni, Pd and Ce (Figure 46a). Figure 46b represents the high resolution spectrum of C 1s which is fitted into two components *viz.*, C–C and C=C corresponding to different BEs. The O 1s spectrum of Pd₃Ni/C–CeO₂ can be fitted into three peaks denoted by O_a (lattice oxygen), O_b (defect sites) and O_c (physisorbed water), as presented in Figure 46c. Pd 3d also gives two doublets *i.e.*, 3d_{5/2} (low energy band) and 3d_{3/2} (high energy band), deconvolution of which gives a total of four peaks at different BEs (Figure 46d). Higher BE peaks are related to Pd²⁺, while, lower BEs corresponds to Pd⁰. This confirmed that Pd is present in both 0 and +2 oxidation states. Since, a part of the BE of both Ni and Ce fall in the same region, high resolution XP spectrum of Ni 2p and Ce 3d appear as combined, as shown in Figure 46e. The peak at 856.5 eV is attributed to Ni 2p_{3/2} band with a satellite peak at 861.4 eV due to smaller amounts of Ni²⁺ species like Ni(OH)₂. Again, the co-existence of Ce³⁺ and Ce⁴⁺ could be

observed in the XP spectrum of Pd₃Ni/C–CeO₂ (Figure 46e), suggesting the defective CeO₂ with oxygen vacancies.

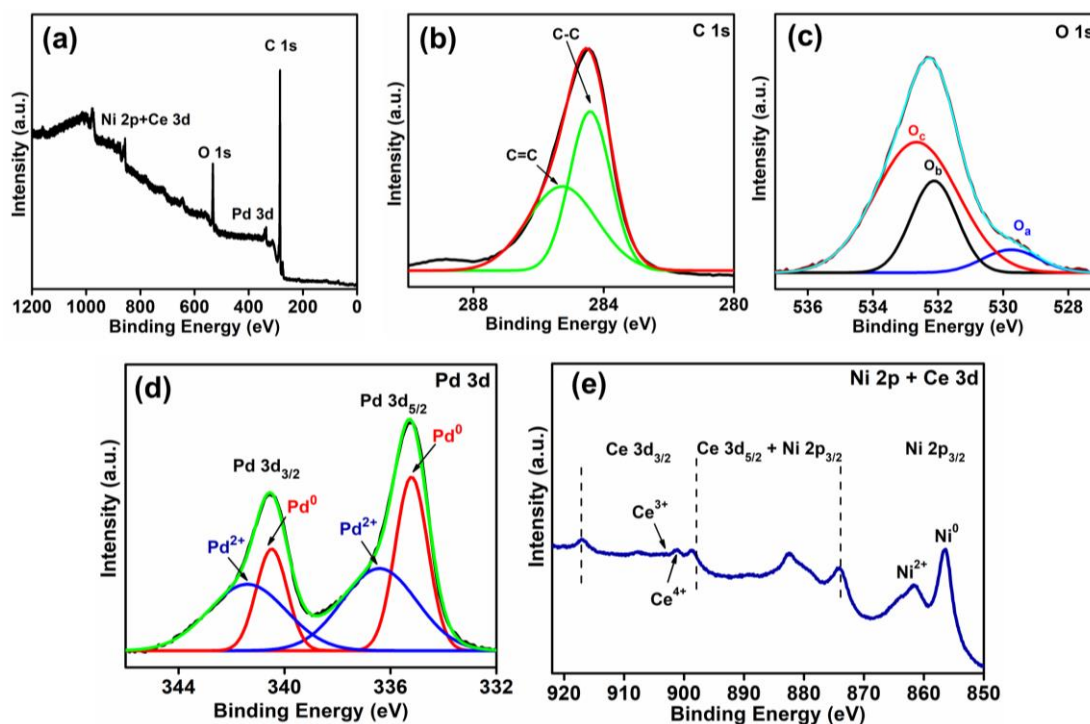


Figure 46. XPS analysis of Pd₃Ni/C–CeO₂; (a) the survey spectrum and the high resolution XP spectra of (b) C 1s, (c) O 1s, (d) Pd 3d, (e) Ni 2p + Ce 3d.

XP spectra of Pd₃Cu/C–CeO₂ are shown in Figure 47a-f. Clearly, the survey spectrum (Figure 47a) established the presence of only detectable elements in Pd₃Cu/C–CeO₂. Figure 47b,c and Figure 47e,f shows the high resolution XP spectra of C 1s, O 1s, Pd 3d and Ce 3d, respectively. Cu 2p XP spectrum (Figure 47d) gives two doublets, Cu 2p_{1/2} and Cu 2p_{3/2} upon fitting. The peaks at BEs of 932.4 and 952.2 eV confirmed the presence of zero-valent Cu. And, the peaks at higher BEs *i.e.*, 934.0 and 954.0 eV along with two satellite peaks at 942.6 and 962.4 eV are the characteristic of Cu²⁺.

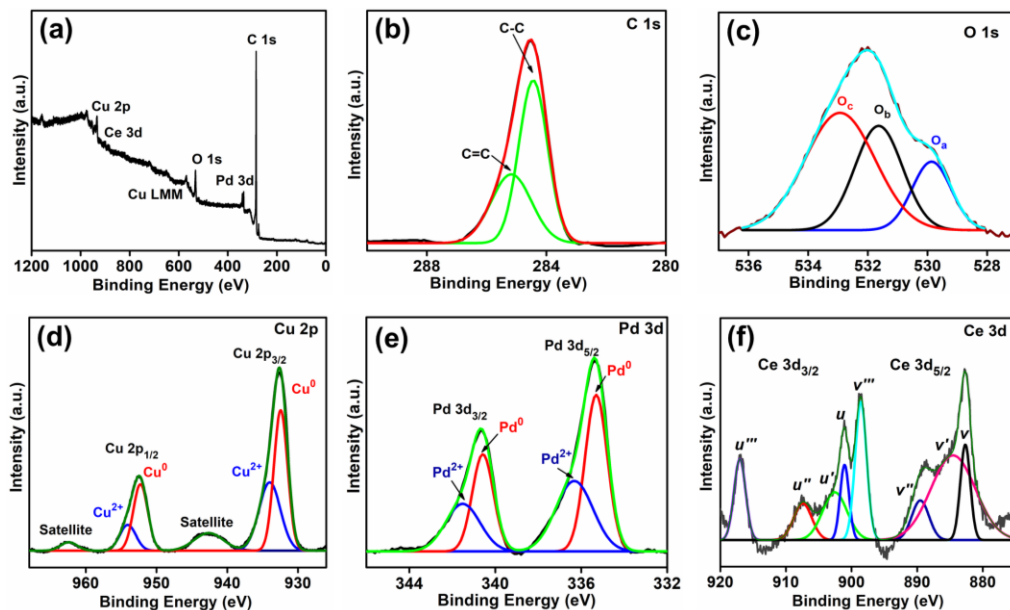


Figure 47. XPS analysis of Pd₃Cu/C–CeO₂; (a) the survey spectrum and the high resolution XP spectrum of (b) C 1s, (c) O 1s, (d) Cu 2p, (e) Pd 3d and (f) Ce 3d.

11. Conclusions summarising the achievements and indication of scope for future work:

In both of these works, a facile and cost-effective hydrothermal method assisted by calcination and carbonization was utilized to synthesize the ECs and characterized by various analytical and electrochemical techniques. CuO_x-CeO₂/C also proceeds via the most favorable “direct four electron reduction pathway” during ORR. Interestingly, CuO_x-CeO₂/C also exhibits relatively better activity than RuO₂ during OER as confirmed from its less positive E_{onset} and small Tafel slope values. Co₃O₄-CeO₂/C hybrid exhibited excellent ORR and OER activity which even surpasses Pt/C (ORR) and RuO₂ (OER) catalysts. Likewise, Co₃O₄-CeO₂/C hybrid proved to have high stability and durability in alkaline medium for ORR as compared to Pt/C catalyst. On the other hand, it also exhibited very high current density (80 mA cm⁻²) for OER at 1.5 V and low η₁₀ (520 mV) relative to a current density of 35 mA cm⁻² and overpotential of 570 mV for RuO₂. The remarkable electrocatalytic performance of the resultant hybrid can be directly correlated to its high ECSA, surface oxygen vacancies and synergistic effects between Co₃O₄ and CeO₂ phases in Co₃O₄-CeO₂/C. This project also enabled us to develop various compositions of bimetallic Pd-based hybrid ECs with or without CeO₂ as promoter having tunable properties that can be studied towards electrochemical CO₂ reduction. Therefore, the project work offers new possibilities for the development of sustainable energy conversion and

related technologies with superior activity, favourable kinetics and long term durability in relatively low cost.

12. S&T benefits accrued:

i. List of Research publications

S No	Authors	Title of paper	Name of the Journal	Volume	Pages	Year	IF
1.	Goswami, C., Hazarika, K. K., Yamada, Y., and Bharali, P.	Nonprecious Hybrid Metal Oxide for Bifunctional Oxygen Electrodes: Endorsing the Role of Interfaces in Electrocatalytic Enhancement	Energy & Fuels	35	13370–13381	2021	3.421
2.	Chutia, B., Hussain, N., Puzari, P., Jampaiah, D., Bhargava, S. K., Matus, E. V., Ismagilov, I. Z., Kerzhentsev, M. and Bharali, P.	Unraveling the Role of CeO ₂ in Stabilization of Multivalent Mn Species on α -MnO ₂ /Mn ₃ O ₄ /CeO ₂ /C Surface for Enhanced Electrocatalysis	Energy & Fuels	35	10756–10769	2021	3.421
3.	Hazarika, K. K., Yamada, Y., Matus, E. V., Kerzhentsev, M.	Enhancing the electrocatalytic activity via hybridization of Cu(I/II) oxides with Co ₃ O ₄ towards oxygen	Journal of Power Sources	587–490	229511	2021	8.128

	ev, M., and Bharali, P.	electrode reactions					
4.	Goswami, C., Yamada, Y., Matus, E. V., Ismagilov , I. Z., Kerzhents ev, M., and Bharali, P.	Elucidating the role of oxide– oxide/carbon interfaces of CuO _x – CeO ₂ /C in boosting electrocatalytic performance.	Langmuir	36	15141– 15152	2020	3.882

- ii. Manpower trained on the project
 - a) Research Scientists or Research Associates: NIL
 - b) No. of Ph.D. produced: 1
 - c) Other Technical Personnel trained: NIL
- iii. Patents taken, if any: NIL

13. Financial Position:

No	Financial Position/ Budget Head	Funds Sanctioned	Expenditure	% of Total cost
I	Salaries/ Manpower costs	6,00,000	6,00,000	100
II	Equipment	-	-	-
III	Supplies & Materials	3,00,000	2,99,596	99.9
IV	Contingencies	89,879	91,919	102.3
V	Travel	4,81,200	4,76,846	99.1
VI	Overhead Expenses	96,000	95,713	99.7
VII	Others, if any (Interest)	8,840	8688 (returned to Bharatkosh)	98.2
	Total	15,75,919	15,72,762	99.8%

14. Procurement/Usage of Equipment

NIL

a)

S No	Name of Equipment	Make/Model	Cost (FE/Rs)	Date of Installation	Utilisation Rate (%)	Remarks regarding maintenance/breakdown

b) Plans for utilizing the equipment facilities in future

Not applicable

15. Exchange visits undertaken

a) India to Partner Country

S No	Name of Scientist	Institutions visited	Duration	Remarks if any
1.	Dr. Pankaj Bharali	Boreskov Institute of Catalysis	10 days	
2.	Dr. Biraj Jyoti Borah	Boreskov Institute of Catalysis	10 days	

a) Partner Country to India

S No	Name of Scientist	Institutions visited	Duration	Remarks if any
-	-	-	-	-

Name and Signature with Date

a. Dr. Pankaj Bharali
(Principal Investigator)

b. Not applicable
(Co-Investigator)

GFR 12 – A
[(SEE RULE 238 (1))]
FORM OF UTILIZATION CERTIFICATE FOR THE GRANTEE ORGANIZATION INCLUDING
AUTONOMOUS ORGANIZATIONS

UTILIZATION CERTIFICATE FOR THE YEAR..2018-2019.....
(period ending 31st March 2019)
In respect of recurring/non-recurring
GRANT-IN-AID/SALARIES/CREATION OF CAPITAL ASSETS

1. Name of the scheme Directed functionalization of oxide and carbon nanomaterials for the development of efficient catalysts for carbon dioxide conversion into value-added products (DST-RFBR)
2. Whether recurring or non-recurring grants Recurring
3. Grants position at the beginning of the financial year
 - (i) Cash in Hand/Bank NIL
 - (ii) Unadjusted advances NIL
 - (iii) Total NIL

4. Details of grants received, expenditure incurred and closing balances: (Actuals)

Unspent Balances of Grants received year [figure as at Sl No 3(iii)]	Interest earned thereon	Interest deposited back to the government	Grant received during the year			Total Available funds (1+2-3+4)	Expenditure incurred	Closing Balance (5-6)
			Sanction no. (i)	Date (ii)	Amount (iii)			
1	2	3	4			5	6	7
NIL	3308/-	NIL	INT/RUS/RFBR/P-322	02.01.2019	11,47,200/-	11,50,508/-	1,40,885/-	10,09,623/-

5. Component wise utilization of grants:

Grants-in-aid-General	Grant-in-aid -Salary	Grants-in-aid-creation of capital	Total
1,06,956/-	33,929/-	NIL	1,40,885/-

6. Details of grants position at end of the year
 - (i) Cash in Hand /Bank 10,09,623/-
 - (ii) Unadjusted Advance NIL
 - (iii) Total 10,09,623/-

7. Certified that I have satisfied myself that the conditions on which grants were sanctioned have been duly fulfilled /are being fulfilled and that I have exercised following checks to see that the money has been actually utilized for the purpose for which it was sanctioned:

Handwritten signature
2015/19

- (i) The main accounts and other subsidiary accounts and registers (including assets register) are maintained as prescribed in the relevant Act/Rules/standing instructions (mention the Act/Rules) and have been duly audited by designated auditors. The figures depicted above tally with the audited figures mentioned in financial statements/accounts.
- (ii) There exist internal controls for safeguarding public funds/assets, watching outcomes and achievements of physical targets against the financial inputs, ensuring quality in asset creation etc. & the periodic evaluation of internal controls is exercised to ensure their effectiveness.
- (iii) To the best of our knowledge and belief, no transactions have been entered that are in violation of relevant Act/Rules/standing instructions and scheme guidelines.
- (iv) The responsibilities among the key functionaries for execution of the scheme have been assigned in clear terms and are not general in nature.
- (v) The benefits were extended to the intended beneficiaries and only such areas/districts were covered where the scheme was intended to operate.
- (vi) The expenditure on various components of the scheme was in the proportions authorized as per the scheme guidelines and terms and conditions of the grants-in-aid.
- (vii) It has been ensured that the physical and financial performance under.....(name of the scheme has been according to the requirements, as prescribed in the guidelines issued by Govt. of India and the performance/targets achieved statement for the year to which the utilization of the fund resulted in outcomes give at Annexure- I duly enclosed.
- (viii) The utilization of the fund resulted in outcomes given at Annexure – II duly enclosed (to be formulated by the Ministry /Department concerned as per their requirements/specifications.)
- (ix) Details of various schemes executed by the agency through grants-in-aid received from the same Ministry or from other Ministries is enclosed at Annexure—II (to be formulated by the Ministry/Department concerned as per their requirements/specifications).

Date:

Place:

Signature

[Handwritten Signature]
 Name
 Chief Finance Officer
 (Head of the Finance)

Finance Officer
Tezpur University

Signature

[Handwritten Signature]
 Name
 Head of the Organisation

Registrar
Tezpur University

(TO BE FILLED IN BY DST)

2. Certified that I have satisfied myself that the conditions on which the grants-in-aid was sanctioned have been fulfilled/are being fulfilled and that I have exercised the following checks to see that the money was actually utilised for the purpose for which it was sanctioned:

Kinds of checks exercised.

- 1.
- 2.
- 3.
- 4.
- 5.

Signature
 Designation
 Date

**REQUEST FOR ANNUAL INSTALLMENT WITH
UP-TO-DATE STATEMENT OF EXPENDITURE**

(Year Means Financial Year i.e.. 1 st April to 31 st March of Next Year)

- | | | | |
|--|--------------------|----|------------------------------|
| 1. Sanction Letter No. | INT/RUS/RFBR/P-322 | 6. | Grant Received in each year: |
| 2. Total Project Cost Rs. | 21,84,400/- | a. | I year Rs . 11,47,200/- |
| 3. Sanctioned/Revised project cost (if applicable) Rs. | None | b. | II year Rs. |
| 4. Date of commencement of Project | 12.02.2019 | c. | III year Rs. |
| 5. Statement of Expenditure | | d. | Interest, Rs. 3,308/- if any |
| | | e. | Total Rs. 11,50,508/- |

<u>Month</u>	<u>Year</u>	
	Month & Year	Expenditure incurred/ committed
	March 2019	33,929 + 6,480 + 49,763 + 13,002 + 21,402 + 16,309
	Total	1,40,885

Note:

1. Expenditure under the sanctioned heads, at any point of time, should not exceed funds allocated under the head, without prior approval of DST i.e. Figures in Column (vii) should not exceed corresponding figures in Column (iii)
2. Utilisation Certificate for each financial year ending 31st March has to be enclosed, along with request for carry-forward permission to next year

Annexure IInd Continued

Sl. No.	Sanctioned Heads**	Funds Allocated (*)	Expenditure Incurred				Balance as on date (Col. iii - vii)	Required Funds till 31 March	Remarks (if any)
			I Yr.	II Yr.	III Yr.	Total (iv+v+vi)			
i.	ii.	iii.	iv.	v.	vi.	vii.	viii.	ix.	x.
1.	Salaries	3,60,000	33,929	NA	NA	33,929	3,26,071	3,60,000	
2.	Permanent Equipments	NIL	-	-	-	-	-	-	
3.	Supplies & Materials/consumables	2,00,000	1,00,476	-	-	1,00,476	99,524	1,00,000	
4.	Travel of Indian Scientists Abroad	4,81,200	NIL	-	-	NIL	4,81,200	4,81,200	
5.	Hospitality of Foreign Scientists - Per diem @ Rs. _____ - Accommodation	NA	-	-	-	-	-	-	
6.	Contingencies	50,000	6,480	-	-	6,480	43,520	50,000	
7.	Overhead Expenses	56,000	NIL			NIL	56,000	46,000	
8.	Interest earned	3,308	-	-	-	-	3,308	-	
	Total	11,50,508	1,40,885	-	-	1,40,885	10,09,623	10,37,200	

Note : * Please indicate heads and allocation as per original / revised (if any) sanction order approving/ revising the project

Name & Signature
Principal Investigator: *Dr. Pankaj Bhandal*
Date: *08/05/2019*

Signature of Competent financial authority
Date: *08/05/2019*
Finance Officer
Tezpur University

GFR 12 – A
[(SEE RULE 238 (1))
FORM OF UTILIZATION CERTIFICATE FOR THE GRANTEE ORGANIZATION INCLUDING
AUTONOMOUS ORGANIZATIONS

UTILIZATION CERTIFICATE FOR THE YEAR..2019-2020.....

(period ending 31st March 2020)

In respect of recurring/non-recurring

GRANT-IN-AID/SALARIES/CREATION OF CAPITAL ASSETS

1. Name of the scheme Directed functionalization of oxide and carbon nanomaterials for the development of efficient catalysts for carbon dioxide conversion into value-added products (DST-RFBR)
2. Whether recurring or non-recurring grants Recurring
3. Grants position at the beginning of the financial year
- (i) Cash in Hand/Bank 10,09,623/-
- (ii) Unadjusted advances NIL
- (iii) Total 10,09,623/-

4. Details of grants received, expenditure incurred and closing balances: (Actuals)

Unspent Balances of Grants received year [figure as at SI No 3(iii)]	Interest earned thereon	Interest deposited back to the government	Grant received during the year			Total Available funds (1+2-3+4)	Expenditure incurred	Closing Balance (5-6)
			Sanction no. (i)	Date (ii)	Amount (iii)			
1	2	3	4			5	6	7
10,09,623/-	5380/-	3308/-	INT/RUS/RFBR/P-322		NIL	10,11,695/-	8,70,194/-	141,501/-

5. Component wise utilization of grants:

Grants-in-aid-General	Grant-in-aid -Salary	Grants-in-aid-creation of capital	Total
5,70,194/-	3,00,000/-	NIL	8,70,194/-

6. Details of grants position at end of the year
- (i) Cash in Hand /Bank 1,41,501/-
- (ii) Unadjusted Advance NIL
- (iii) Total 1,41,501/-

7. Certified that I have satisfied myself that the conditions on which grants were sanctioned have been duly fulfilled /are being fulfilled and that I have exercised following checks to see that the money has been actually utilized for the purpose for which it was sanctioned:

- (i) The main accounts and other subsidiary accounts and registers (including assets register) are maintained as prescribed in the relevant Act/Rules/standing instructions (mention the Act/Rules) and have been duly audited by designated auditors. The figures depicted above tally with the audited figures mentioned in financial statements/accounts.
- (ii) There exist internal controls for safeguarding public funds/assets, watching outcomes and achievements of physical targets against the financial inputs, ensuring quality in asset creation etc. & the periodic evaluation of internal controls is exercised to ensure their effectiveness.
- (iii) To the best of our knowledge and belief, no transactions have been entered that are in violation of relevant Act/Rules/standing instructions and scheme guidelines.
- (iv) The responsibilities among the key functionaries for execution of the scheme have been assigned in clear terms and are not general in nature.
- (v) The benefits were extended to the intended beneficiaries and only such areas/districts were covered where the scheme was intended to operate.
- (vi) The expenditure on various components of the scheme was in the proportions authorized as per the scheme guidelines and terms and conditions of the grants-in-aid.
- (vii) It has been ensured that the physical and financial performance under.....(name of the scheme has been according to the requirements, as prescribed in the guidelines issued by Govt. of India and the performance/targets achieved statement for the year to which the utilization of the fund resulted in outcomes give at Annexure- I duly enclosed.
- (viii) The utilization of the fund resulted in outcomes given at Annexure – II duly enclosed (to be formulated by the Ministry /Department concerned as per their requirements/specifications.)
- (ix) Details of various schemes executed by the agency through grants-in-aid received from the same Ministry or from other Ministries is enclosed at Annexure—II (to be formulated by the Ministry/Department concerned as per their requirements/specifications).

Date:

Place: Tezpur

Signature

Name 14/07/20
Chief Finance Officer
(Head of the Finance)

*Finance Officer
Tezpur University*

Signature

Name
Head of the Organisation

*Registrar
Tezpur University*

(TO BE FILLED IN BY DST)

2. Certified that I have satisfied myself that the conditions on which the grants-in-aid was sanctioned have been fulfilled/are being fulfilled and that I have exercised the following checks to see that the money was actually utilised for the purpose for which it was sanctioned:

Kinds of checks exercised.

- 1.
- 2.
- 3.
- 4.
- 5.

Signature
Designation
Date

REQUEST FOR ANNUAL INSTALLMENT WITH UP-TO-DATE STATEMENT OF EXPENDITURE

(Year Means Financial Year i.e.. 1 st April to 31 st March of Next Year)

- | | |
|---|---|
| 1. Sanction Letter No. INT/RUS/RFBR/P-322
2. Total Project Cost Rs. 21,84,400/-
3. Sanctioned/Revised project cost (if applicable) Rs. None
4. Date of commencement of Project 12.02.2019
5. Statement of Expenditure | 6. Grant Received in each year:
a. I year Rs . 11,47,200/-
b. II year Rs. NIL
c. III year Rs.
d. Interest, if any Rs. 3,308/- + 5,380/-
e. Total Rs. 11,55,888/- |
|---|---|

Month Year

Month & Year	Expenditure incurred/ committed
April 2019	25,000
May 2019	$25,000 + 2,800 + 35,000 + 2,352 = 65,152$
June 2019	25,000
July 2019	25,000
August 2019	25,000
September 2019	$25,000 + 4,625 + 26,120 + 4,000 = 59,745$
October 2019	$25,000 + 5,958 = 30,958$
November 2019	25,000
December 2019	25,000
January 2020	25,000
February 2020	25,000
March 2020	$25,000 + 1,650 + 13,195 + 3,357 + 4,71,137 = 5,14,339$
Total	8,70,194

*** Purchase order placed before lockdown and payment is pending.**

Note:


1. Expenditure under the sanctioned heads, at any point of time, should not exceed funds allocated under the head, without prior approval of DST i.e. Figures in Column (vii) should not exceed corresponding figures in Column (iii)
2. Utilisation Certificate for each financial year ending 31st March has to be enclosed, along with request for carry-forward permission to next year


Annexure IInd Continued

Sl. No.	Sanctioned Heads**	Funds Allocated (*)	Expenditure Incurred				Balance as on date (Col. iii - vii)	Required Funds till 31 March	Remarks (if any)
			I Yr.	II Yr.	III Yr.	Total (iv+v+vi)			
i.	ii.	iii.	iv.	v.	vi.	vii.	viii.	ix.	x.
1.	Salaries	3,60,000	33,929	3,00,000	NA	3,33,929	26,071	5,32,800**	**The enhanced fellowship of JRF @ 31000/- + HRA for the entire duration of the project may be considered.
2.	Permanent Equipments	NIL	-	-	-	-	-	-	
3.	Supplies & Materials/consumables	2,00,000	1,00,476	NIL [#]	-	1,00,476	99,524	1,00,000	
4.	Travel of Indian Scientists Abroad	4,81,200	NIL	4,76,846	-	4,76,846	4,354	4,81,200	
5.	Hospitality of Foreign Scientists - Per diem @ Rs. _____ - Accommodation	NA	-	-	-	-	-	-	
6.	Contingencies	50,000	6,480	41,153	-	47,633	2,367	50,000	
7.	Overhead Expenses	56,000	NIL	52,195	-	52,195	3,805	46,000	
8.	Interest earned	8,688	-	-	-	-	5,380	-	
	Total	11,55,888	1,40,885	8,70,194	-	10,11,079	1,41,501	12,10,000	

Note : * Please indicate heads and allocation as per original / revised (if any) sanction order approving/ revising the project

[#] Purchase order of Rs. 99,200/- placed before lockdown and payment is pending.

Name & Signature: 
Principal Investigator: **Dr. Pankaj Banerji**
Date: **09/07/2020**


Signature of Competent financial authority
Date: **Finance Officer**
Tezpur University

GFR 12 – A
[(SEE RULE 238 (1))
FORM OF UTILIZATION CERTIFICATE FOR THE GRANTEE ORGANIZATION INCLUDING
AUTONOMOUS ORGANIZATIONS

UTILIZATION CERTIFICATE FOR THE YEAR..2020-2021.....

(period ending 31st March 2021)

In respect of recurring/non-recurring

GRANT-IN-AID/SALARIES/CREATION OF CAPITAL ASSETS

1. Name of the scheme Directed functionalization of oxide and carbon nanomaterials for the development of efficient catalysts for carbon dioxide conversion into value-added products (DST-RFBR)
2. Whether recurring or non-recurring grants Recurring
3. Grants position at the beginning of the financial year
- (i) Cash in Hand/Bank 1,36,121/-
- (ii) Unadjusted advances NIL
- (iii) Total 1,36,121/-

4. Details of grants received, expenditure incurred and closing balances: (Actuals)

Unspent Balances of Grants received year [figure as at SI No 3(iii)]	Interest earned thereon	Interest deposited back to the government	Grant received during the year			Total Available funds (1+2-3+4)	Expenditure incurred	Closing Balance (5-6)
			Sanction no. (i)	Date (ii)	Amount (iii)			
1	2	3	4			5	6	7
1,36,121/-	75/-	NIL	INT/RUS/RFBR/P-322	20/11/2020	4,19,879/-	5,56,075/-	5,52,995/-	3,080/-

5. Component wise utilization of grants:

Grants-in-aid-General	Grant-in-aid -Salary	Grants-in-aid-creation of capital	Total
2,86,924/-	2,66,071/-	NIL	5,52,995/-

6. Details of grants position at end of the year
- (i) Cash in Hand /Bank 3,080/-
- (ii) Unadjusted Advance NIL
- (iii) Total 3,080/-

7. Certified that I have satisfied myself that the conditions on which grants were sanctioned have been duly fulfilled /are being fulfilled and that I have exercised following checks to see that the money has been actually utilized for the purpose for which it was sanctioned:

- (i) The main accounts and other subsidiary accounts and registers (including assets register) are maintained as prescribed in the relevant Act/Rules/standing instructions (mention the Act/Rules) and have been duly audited by designated auditors. The figures depicted above tally with the audited figures mentioned in financial statements/accounts.
- (ii) There exist internal controls for safeguarding public funds/assets, watching outcomes and achievements of physical targets against the financial inputs, ensuring quality in asset creation etc. & the periodic evaluation of internal controls is exercised to ensure their effectiveness.
- (iii) To the best of our knowledge and belief, no transactions have been entered that are in violation of relevant Act/Rules/standing instructions and scheme guidelines.
- (iv) The responsibilities among the key functionaries for execution of the scheme have been assigned in clear terms and are not general in nature.
- (v) The benefits were extended to the intended beneficiaries and only such areas/districts were covered where the scheme was intended to operate.
- (vi) The expenditure on various components of the scheme was in the proportions authorized as per the scheme guidelines and terms and conditions of the grants-in-aid.
- (vii) It has been ensured that the physical and financial performance under.....(name of the scheme has been according to the requirements, as prescribed in the guidelines issued by Govt. of India and the performance/targets achieved statement for the year to which the utilization of the fund resulted in outcomes give at Annexure- I duly enclosed.
- (viii) The utilization of the fund resulted in outcomes given at Annexure – II duly enclosed (to be formulated by the Ministry /Department concerned as per their requirements/specifications.)
- (ix) Details of various schemes executed by the agency through grants-in-aid received from the same Ministry or from other Ministries is enclosed at Annexure—II (to be formulated by the Ministry/Department concerned as per their requirements/specifications).

Date:

Place: Tezpur

Signature

Name

Chief Finance Officer
(Head of the Finance)

*Finance Officer
Tezpur University*

Signature

Name

Head of the Organisation

*Registrar
Tezpur University*

(TO BE FILLED IN BY DST)

2. Certified that I have satisfied myself that the conditions on which the grants-in-aid was sanctioned have been fulfilled/are being fulfilled and that I have exercised the following checks to see that the money was actually utilised for the purpose for which it was sanctioned:

Kinds of checks exercised.

- 1.
- 2.
- 3.
- 4.
- 5.

Signature
Designation
Date

**REQUEST FOR ANNUAL INSTALLMENT WITH
UP-TO-DATE STATEMENT OF EXPENDITURE**

(Year Means Financial Year i.e.. 1 st April to 31 st March of Next Year)

- | | | | |
|--|--------------------|----|---|
| 1. Sanction Letter No. | INT/RUS/RFBR/P-322 | 6. | Grant Received in each year: |
| 2. Total Project Cost Rs. | 21,84,400/- | a. | I year Rs . 11,47,200/- |
| 3. Sanctioned/Revised project cost (if applicable) Rs. | None | b. | II year Rs. 4,19,879/- |
| 4. Date of commencement of Project | 12.02.2019 | c. | III year Rs. |
| 5. Statement of Expenditure | | d. | Interest, Rs. 3,308/- + 5,380/- + 75/- if any |
| | | e. | Total Rs. 15,75,842/- |

Month Year

Month & Year	Expenditure incurred/ committed
April 2020	25,000
May 2020	25,000
June 2020	25,000
July 2020	25,000
August 2020	25,000
September 2020	-
October 2020	-
November 2020	-
December 2020	1,00,000
January 2021	25,000 + 99120 = 1,24,120
February 2021	16,071
March 2021	1,00,000 + 44,286 +28,750 + 14,768 = 1,87,804
Total	5,52,995

*** Purchase order placed before lockdown and payment was pending.**

Note:

1. Expenditure under the sanctioned heads, at any point of time, should not exceed funds allocated under the head, without prior approval of DST i.e. Figures in Column (vii) should not exceed corresponding figures in Column (iii)
2. Utilisation Certificate for each financial year ending 31st March has to be enclosed, along with request for carry-forward permission to next year

Annexure IInd Continued

Sl. No.	Sanctioned Heads**	Funds Allocated (*)	Expenditure Incurred					Balance as on date (Col. iii - viii)	Required Funds till 31 March	Remarks (if any)
			I Yr.	II Yr.	III Yr.	IV Yr. (Extn)	Total (iv+v+vi+vii)			
i.	ii.	iii.	iv.	v.	vi.	vii.	viii.	ix.	x.	xi.
1.	Salaries	(3,60,000 +2,40,000) 6,00,000	33,929	3,00,000	2,66,071	-	6,00,000	-		
2.	Permanent Equipments	NIL	-	-	-	-	-	-		
3.	Supplies & Materials/consumables	(2,00,000+ 1,00,000) 3,00,000	1,00,476	NIL	1,99,120	-	2,99,596	404		
4.	Travel of Indian Scientists Abroad	4,81,200	NIL	4,76,846	-	-	4,76,846	4,354		
5.	Hospitality of Foreign Scientists - Per diem @ Rs. _____ - Accommodation	NA	-	-	-	-	-	-		
6.	Contingencies	(50,000+ 39,879) 89,879	6,480	41,153	44,286	-	91,919	-2,040		
7.	Overhead Expenses	(56,000+ 40,000) 96,000	NIL	52,195	43,518	-	95,713	287		
8.	Interest earned	(3308+ 5380+75) 8,763	-	-	-	-	-	75		8688 returned to Bharatkosh
	Total	15,75,842	1,40,885	8,70,194	5,52,995	-	15,64,074	3,080		

Note : * Please indicate heads and allocation as per original / revised (if any) sanction order approving/ revising the project

Name & Signature
Principal Investigator:
Date:

[Signature]
Dr. Ranvijay Bhanal
19/12/22

Signature of Competent financial authority
Date:

[Signature]
Finance Officer
Tezpur University

GFR 12 – A
[(SEE RULE 238 (1))
FORM OF UTILIZATION CERTIFICATE FOR THE GRANTEE ORGANIZATION INCLUDING
AUTONOMOUS ORGANIZATIONS

UTILIZATION CERTIFICATE FOR THE YEAR..2021-2022.....
 (period ending 1st July 2021, project completion date with no cost extension)
 In respect of recurring/non-recurring
 GRANT-IN-AID/SALARIES/CREATION OF CAPITAL ASSETS

1. Name of the scheme Directed functionalization of oxide and carbon nanomaterials for the development of efficient catalysts for carbon dioxide conversion into value-added products (DST-RFBR)
2. Whether recurring or non-recurring grants Recurring
3. Grants position at the beginning of the financial year
- (i) Cash in Hand/Bank 3080/-
- (ii) Unadjusted advances NIL
- (iii) Total 3080/-

4. Details of grants received, expenditure incurred and closing balances: (Actuals)

Unspent Balances of Grants received year [figure as at SI No 3(iii)]	Interest earned thereon	Interest deposited back to the government	Grant received during the year			Total Available funds (1+2-3+4)	Expenditure incurred	Closing Balance (5-6)
			Sanction no. (i)	Date (ii)	Amount (iii)			
1	2	3	4			5	6	7
3,080/-	77/-	NIL			NIL	3,157/-	NIL	3,157/-

5. Component wise utilization of grants:

Grants-in-aid-General	Grant-in-aid -Salary	Grants-in-aid-creation of capital	Total
NIL	NIL	NIL	NIL

6. Details of grants position at end of the year
- (i) Cash in Hand /Bank 3,157/-
- (ii) Unadjusted Advance NIL
- (iii) Total 3,157/-

7. Certified that I have satisfied myself that the conditions on which grants were sanctioned have been duly fulfilled /are being fulfilled and that I have exercised following checks to see that the money has been actually utilized for the purpose for which it was sanctioned:

- (i) The main accounts and other subsidiary accounts and registers (including assets register) are maintained as prescribed in the relevant Act/Rules/standing instructions (mention the Act/Rules) and have been duly audited by designated auditors. The figures depicted above tally with the audited figures mentioned in financial statements/accounts.
- (ii) There exist internal controls for safeguarding public funds/assets, watching outcomes and achievements of physical targets against the financial inputs, ensuring quality in asset creation etc. & the periodic evaluation of internal controls is exercised to ensure their effectiveness.
- (iii) To the best of our knowledge and belief, no transactions have been entered that are in violation of relevant Act/Rules/standing instructions and scheme guidelines.
- (iv) The responsibilities among the key functionaries for execution of the scheme have been assigned in clear terms and are not general in nature.
- (v) The benefits were extended to the intended beneficiaries and only such areas/districts were covered where the scheme was intended to operate.
- (vi) The expenditure on various components of the scheme was in the proportions authorized as per the scheme guidelines and terms and conditions of the grants-in-aid.
- (vii) It has been ensured that the physical and financial performance under.....(name of the scheme has been according to the requirements, as prescribed in the guidelines issued by Govt. of India and the performance/targets achieved statement for the year to which the utilization of the fund resulted in outcomes give at Annexure- I duly enclosed.
- (viii) The utilization of the fund resulted in outcomes given at Annexure – II duly enclosed (to be formulated by the Ministry /Department concerned as per their requirements/specifications.)
- (ix) Details of various schemes executed by the agency through grants-in-aid received from the same Ministry or from other Ministries is enclosed at Annexure—II (to be formulated by the Ministry/Department concerned as per their requirements/specifications).

Date:

Place: Tezpur

Signature

Name

Chief Finance Officer
(Head of the Finance)

*Finance Officer
Tezpur University*

Signature

Name

Head of the Organisation

*Registrar
Tezpur University*

(TO BE FILLED IN BY DST)

2. Certified that I have satisfied myself that the conditions on which the grants-in-aid was sanctioned have been fulfilled/are being fulfilled and that I have exercised the following checks to see that the money was actually utilised for the purpose for which it was sanctioned:

Kinds of checks exercised.

- 1.
- 2.
- 3.
- 4.
- 5.

Signature
Designation
Date

**REQUEST FOR ANNUAL INSTALLMENT WITH
UP-TO-DATE STATEMENT OF EXPENDITURE**

(Year Means Financial Year i.e.. 1 st April to 31 st March of Next Year)

- | | | | |
|--|---|----|---|
| 1. Sanction Letter No. | INT/RUS/RFBR/P-322 | 6. | Grant Received in each year: |
| 2. Total Project Cost Rs. | 21,84,400/- | a. | I year Rs . 11,47,200/- |
| 3. Sanctioned/Revised project cost (if applicable) Rs. | None | b. | II year Rs. 4,19,879/- |
| 4. Date of commencement of Project | 12.02.2019 (No cost extension up to 01.07.2021) | c. | III year Rs. NIL |
| 5. Statement of Expenditure | | d. | Interest, Rs. 3,308/- + 5,380/- + 75/- if any +77/- |
| | | e. | Total Rs. 15,75,919/- |

Month Year

Month & Year	Expenditure incurred/ committed
Total	NIL

Note:

- Expenditure under the sanctioned heads, at any point of time, should not exceed funds allocated under the head, without prior approval of DST i.e. Figures in Column (vii) should not exceed corresponding figures in Column (iii)
- Utilisation Certificate for each financial year ending 31st March has to be enclosed, along with request for carry-forward permission to next year

Annexure IInd Continued


Sl. No.	Sanctioned Heads**	Funds Allocated (*)	Expenditure Incurred					Balance as on date (Col. iii - viii)	Required Funds till 31 March	Remarks (if any)
			I Yr.	II Yr.	III Yr.	IV Yr. (No cost Extn)	Total (iv+v+vi+vii)			
i.	ii.	iii.	iv.	v.	vi.	vii.	viii.	ix.	x.	xi.
1.	Salaries	(3,60,000 +2,40,000) 6,00,000	33,929	3,00,000	2,66,071	-	6,00,000	-		
2.	Permanent Equipments	NIL	-	-	-	-	-	-		
3.	Supplies & Materials/consumables	(2,00,000+ 1,00,000) 3,00,000	1,00,476	NIL	1,99,120	-	2,99,596	404		
4.	Travel of Indian Scientists Abroad	4,81,200	NIL	4,76,846	-	-	4,76,846	4,354		
5.	Hospitality of Foreign Scientists - Per diem @ Rs. _____ - Accommodation	NA	-	-	-	-	-	-		
6.	Contingencies	(50,000+ 39,879) 89,879	6,480	41,153	44,286	-	91,919	-2,040		
7.	Overhead Expenses	(56,000+ 40,000) 96,000	NIL	52,195	43,518	-	95,713	287		
8.	Interest earned	(3308+ 5380+75+77) 8,763	-	-	-	-	-	152 (75+77)		8688 returned to Bharatkosh
	Total	15,75,919	1,40,885	8,70,194	5,52,995	-	15,64,074	3,157		

Note : * Please indicate heads and allocation as per original / revised (if any) sanction order approving/ revising the project

Name & Signature

Principal Investigator:

Date:


Dr. Ranbir Bhanal

19/12/22

Signature of Competent financial authority

Date:


Finance Officer
Jespur University